Mathematical Modelling of Magnesium Corrosion for Orthopaedic Implants

by

Safia K. Ahmed

Doctoral thesis submitted in partial fulfilment of the requirements for the award of Doctor of Philosophy

Loughborough University

Supervised by Dr. John Ward

Co-supervised by Dr. Yang Liu

Abstract

Magnesium (Mg) has grasped the attention of biomaterial researchers due to its desirable properties for orthopaedic implants. It is a biodegradable, lightweight structured metal with mechanical properties more comparable to the human bone than frequently used implant materials like titanium and stainless steel. However, the element corrodes rapidly in aqueous environments, which prevents its direct use as an implant material. In this thesis, novel mathematical models are presented to address the problem of Mg corrosion.

In aqueous environments, a Mg implant reacts to form magnesium hydroxide $(Mg(OH)_2)$, which can react further with bicarbonate ions to form magnesium carbonate $(MgCO_3)$; these reactions are considered in the corrosion models developed in this work, and this is the first study to consider $MgCO_3$. A simple mass action model was derived first, which predicted the amount of Mg and its corrosion products over time, where an exponential decay of Mg was perceived.

The backbone of this thesis is a PDE model for Mg corrosion, which considers distinct porous layers of $Mg(OH)_2$ and $MgCO_3$ surrounding a block of Mg with the advection and diffusion of H_2O and CO_2 through porous media; this porous media assumption is a novel feature in comparison to other metal corrosion models. The model was derived and analysed in one spatial dimension for Cartesian, radically symmetric spherical and cylindrical geometries. Singularities resulting from the model at small time were handled using asymptotic analysis. The effect of the model parameters on key timescales was investigated, whereby porosity of the layers and reaction rates of H_2O and Mg were shown to have a significant effect. Furthermore, the porous media assumption on the Mg compound layers led to the prediction of a slightly faster corrosion of the original Mg block compared to that with different rates of advection.

In addition to the above, corrosion from inside a single Mg pore was considered using the same modelling approach. The timescale for pore closure and the size of Mg corrosion at pore closure were of particular interest, and were affected by changes in the parameters. The pore closure time was found to be rapid in comparison to the degradation time of the implant.

The final model in this work is a physiologically based pharmacokinetic (PBPK) model, which is used to explore the effects of a corroding Mg implant on blood serum levels; a high amount of Mg in the blood can cause complications. Values for the implant release rate of Mg and urine excretion rates were refined in the model, where it was highlighted that an Mg implantation must be carefully considered for patients, particularly those with reduced renal function.

Acknowledgements

Firstly, I want to thank God for helping me with everything and giving me the strength to write this thesis. Many thanks go to my supervisor, Dr. John Ward, for his invaluable support, guidance and patience throughout the last four years. I would also like to thank my co-supervisor, Dr. Yang Liu, for her guidance and helpful insights on my PhD topic. Thank you to the Loughborough University Graduate School for the scholarship provided to help me complete my PhD. It has been a pleasure to be given the opportunity to take part in interdisciplinary research. Finally, a huge thank you to my parents and family for all their support and prayers.

"Seeking knowledge is an obligation upon every Muslim."

-Prophet Muhammad

"Indeed, with hardship will be ease."

-Qur'an 94:6

Publications

The work in Chapter 3 has been published in [1], and is titled "Numerical Modelling of Effects of Biphasic Layers of Corrosion Products to the Degradation of Magnesium Metal *in vitro*" by Safia K. Ahmed, John P. Ward and Yang Liu (2017) in *Materials*, 11(1).

The work presented in Chapter 4 and Chapter 5 are intended for submission.

Contents

List of Figures

List of Tables

Chapter 1

Introduction

Orthopaedic implant surgeries are required when the bone fails to heal and regenerate by itself after a severe bone defect or fracture. Implant materials are used to hold the bone together whilst it heals, and these can come in the form of screws, stents, pins and plates (see Figure 1.1 for a fracture fixation using screws). The requirement of orthopaedic surgical procedures are usually due to fractures resulting from osteoporosis or a traumatic accident, both of which are increasing due to people living longer, and the occurrence of more sport injuries and road accidents [9]. On top of this, additional surgeries are performed to remove the implants after the bone has healed because frequently used implant materials are non-biodegradable; these surgical procedures are also on the rise [10]. A biodegradable material like magnesium (Mg) would eliminate the need for implant removal surgery.

Magnesium is a lightweight structured metal that is becoming increasingly popular for bone implants due to its desirable assets. As an orthopaedic implant, magnesium degrades and replaces bone tissue whilst healing a fracture eventually leading to its full absorption into the bone. Ionic magnesium is the fourth most abundant cation in the human body. The element is detected in large amounts in the bone tissue, and is a significant component in stimulating bone growth [11, 12, 13]. Furthermore, mag-
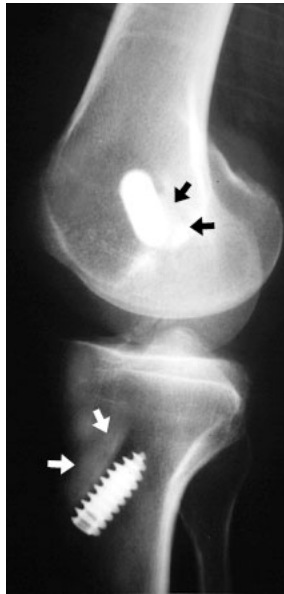
Figure 1.1: Screws used to fix a bone graft in place. Taken with permission from [2]

nesium holds physical and mechanical properties more comparable to human bone than frequently used implant materials like titanium and stainless steel, thus eliminating the problem of stress shielding. Stress shielding is caused by a conventional implant material through the removal of normal bone stress, which leads to a lower bone density [14].

While there are numerous benefits of magnesium implants, Mg has the undesirable property of rapid corrosion in an aqueous environment, which is consistently an obstacle for biomaterial researchers [15]. This corrosion is due to magnesium being reactive with water forming magnesium hydroxide, $Mg(OH)_2$, and releasing bubbles of hydrogen that can deposit near the implant to form gas pockets. Furthermore, the rapid corrosion causes the loss of mechanical support before the newly formed bone tissue can bear the load, thereby preventing the bone from healing correctly. A gradual degradation of Mg is thus preferable. The rapid corrosion effects can be mitigated by using alloys of magnesium, and research into this for their use in orthopaedic implant devices is vastly growing [6, 16]. Physiological consequences of Mg

implants have also been widely explored [12, 17]. However, the major challenge that continues to be faced by regulators and industry is how to predict the corrosion rate of magnesium metal-based biomaterials *in vitro* and correlate this to the timing of its absorption *in vivo*. In this thesis, the problem is approached using mathematical modelling aimed to provide a systematic means of quantitatively describing the physiochemical interaction during magnesium corrosion processes *in vitro*, further informing standardisation of *in vitro* investigation of magnesium alloy corrosion and implant design parameters for optimal bone growth.

The degradation of Mg in an aqueous environment involves the reaction between Mg and H_2O to form $Mg(OH)_2$, which then reacts with other physiological ions in the environment such as dissolved CO_2, to ultimately form magnesium carbonate, $MgCO_3$. The latter feature is currently absent in the few magnesium corrosion mathematical models that exist, and is believed to play an important part in the performance of an implant *in vivo* [18]; this is the first study to consider $MgCO_3$ in a magnesium corrosion mathematical model. To describe Mg degradation, two types of mathematical models are developed in this thesis; an ordinary differential equation (ODE) model (Chapter 2) and a partial differential equation (PDE) model (Chapters 3 and 4). The PDE model is the backbone of this thesis, for which an extension of the approach by [19] was adopted, but applied instead to magnesium, and the resulting layers of corrosive products $Mg(OH)_2$ and $MgCO_3$. A novelty of the PDE model is that it considers the corrosion layers as porous media, whereby there is a fluid phase flow within the pores of the developing crystal structures, so that the reactants, H_2O and CO_2, can advect, as well as diffuse, through them. Whether or not this porous media assumption leads to substantially different results is one of the aspects explored in this thesis.

Typically, a magnesium sample for research into orthopaedic applications is porous.

Depending on the size and number of pores, this is known to be beneficial during the absorption of an implant [6]. To include porosity in this work, the degradation inside a magnesium pore is analysed (Chapter 4). Such an approach on modelling the degradation of magnesium adds to the novelty of this thesis.

The absorption of a magnesium implant incorporates the release of magnesium ions into the blood resulting in an increase in magnesium levels. An excessive amount of magnesium in the blood can lead to a condition called hypermagnesemia, which can have a serious impact on the patients health if left uncontrolled. It is known that magnesium deficiency is a common trait in the western world and the human body is effective at excreting any excess magnesium via the kidneys [8], so a degrading magnesium implant may not lead to hypermagnesemia, but, in agreement with [20], such effects should still be monitored. A physiologically based pharmacokinetic (PBPK) model is thus developed in this thesis, which aims to ensure hypermagnesemia can be prevented during implantation (Chapter 5). It is the first mathematical model derived to explore this issue.

To sum up, four original mathematical models have been developed in this thesis, that aim to provide a framework for describing magnesium degradation *in vitro* and *in vivo*. The long-term goal is to guide relatively simple *in vitro* experimentation that can inform optimal choices for model parameters, which can then be used, with appropriate geometries and dimensions, to predict corrosion *in vivo*.

The remainder of this chapter reflects on different topics surrounding magnesium corrosion of orthopaedic implants starting with a history of magnesium implants. Next, the degradation of magnesium is explained in detail, after which Mg based implants are compared to other materials. Following this, *in vitro* and *in vivo* studies are reviewed, and then mathematical models on degradation and PBPK models are discussed. The chapter ends with a description of the thesis structure.

1.1 The History of Magnesium Implants

When discussing the history of magnesium implants, the work of Witte [21] is cited by many researchers [12, 22, 23, 24]; it includes a brief history which is summarized here. The element, magnesium, was discovered in 1808 by the British chemist Sir Humphry Davy. In medicine, magnesium implants have been applied in osteosythesis, neurorrhaphy and cardiology. A remarkable result of Mg implantation was in the treatment of proliferating hemangioma in a 3-month-old child located on the face, throat and shoulder, [21, 25]; hemangioma is the growth of blood vessels.

The first use of magnesium in orthopaedic surgery was by Lambotte in 1906, who used the implant on a 17 year old to treat a fractured bone of the lower limb. The implant was later removed due to the evolution of gas cavities and the pain experienced by the patient [12, 21]. Through further experiments the complete absorption of magnesium was witnessed by Lambotte [21]. Research on magnesium orthopaedic implants in the beginning of the twentieth century was quite focused as several researchers contributed towards different findings. However, because of the issue of its rapid corrosion rate, surgeons became attracted to stainless steel and titanium implants when they were invented and neglected the concentrated use of magnesium as an implant material, [25]. According to [25], stainless steel was developed in the 1930s, and [26] reports that titanium alloys were first employed in the 1960s; the use of both has gradually increased over time. Other implant materials were also invented, but stainless steel and titanium still remain popular choices today [22, 27]. Nevertheless, concerns over these implant materials regarding non-biodegradability and problematic corrosion products led the implant industry to reassess magnesium in the late 1990s [20, 25]. Since then an extensive amount of research has been conducted on magnesium as an orthopaedic implant material focusing on its enhancement in corrosion resistance [25]. A review by Kirkland in 2012 [23] pinpoints that inter-

national journals are publishing approximately 10 to 15 articles on Mg orthopaedic implants per week. Furthermore, a review written in 2014 describes the increasing rate of interest in Mg as "exponential" [20].

1.2 Degradation of Magnesium

Countless papers hail magnesium for its distinct physical and mechanical properties for bone implants, but while many desirable features of Mg can be emphasised, it does hold undesirable properties. These are all related to its rapid corrosion rate in an aqueous environment [23].

In the body, or in a clinically relevant environment, Mg implants undergo the following reaction

$$\text{Mg} + 2\,\text{H}_2\text{O} \longrightarrow \text{Mg(OH)}_2 + \text{H}_2, \qquad\qquad (1.1)$$
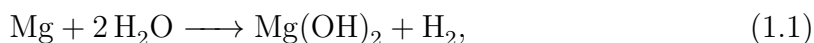
to produce magnesium hydroxide and hydrogen gas [16]. The reaction is rapid causing an excess release of hydrogen gas in a short time that can accumulate to form gas pockets near the implant and delay healing [16, 23, 28, 29]. A build-up of the gas can cause necrosis of tissues; which is the unregulated death of cells in the tissues. In the worst-case scenario severe hydrogen evolution can block the blood stream resulting in a fatality [23, 28]; although this has not yet been reported from implantation studies. The magnesium hydroxide produced in (1.1) acts as a protective layer on the magnesium surface, but is only stable at a high pH, which means that in physiological environments it is vulnerable to further corrosion [30]. The hydroxide can react with other physiological ions in the body or in clinical solutions, such as dissolved carbon dioxide, chloride ions and phosphate ions, forming further magnesium compounds [16, 31, 32]. All products produced during the degradation process are non-toxic [6], but if the reaction in (1.1) is rapid then it can lead to toxicity due to an increase in local pH [33]. Furthermore, the rapid corrosion causes the loss of mechanical support

before the newly formed bone tissue can bear the load.

Impurities within Mg metal also contribute to the rapid corrosion rate in (1.1) [28, 29]. The contaminants emerge unintentionally during its manufacturing process and are found in small amounts; they include iron (Fe), nickel (Ni) and copper (Cu). To determine tolerable amounts of the impurities in Mg, the notion of "tolerance limits" has been introduced [29, 34]. When the amounts of Fe, Ni and Cu are beyond the "tolerance limit" Mg degradation is accelerated.

To mitigate all the harmful effects of Mg corrosion mentioned above, implants are being alloyed with small amounts of other elements or coated with a protective layer [6, 23]. However, the corrosion of the alloying elements within the implant can lead to toxicity [23, 27], which means that alloying components need to be carefully selected. For this reason, the branch of Mg based alloys within orthopaedic implants is broad. This topic is discussed further in Section 1.4. Moreover, a high purity Mg, which is not usually achievable, is said to be more corrosion resistant than Mg alloys; but compared to commercial purity Mg, alloying elements in their pure form are "nobler" [16, 28]. In agreement with [28], understanding the degradation of a commercial purity Mg is the groundwork to apprehend Mg alloys, coating and purification impacts. This thesis observes the corrosion of a commercially pure Mg, which is referred to as "pure magnesium".

Returning to (1.1) magnesium hydroxide undergoes further corrosion with physiological ions in the body or in clinical environments. The most mentioned reaction in the literature is with chloride ions that are present in salt solutions *in vitro* (reflecting that in physiological environments) to produce magnesium chloride $MgCl_2$ [6, 16]. Studies have observed the long-term degradation of Mg *in vitro* of which the final products are found to be crystals of magnesium carbonate, $MgCO_3$, and a precipitate of calcium phosphate, $Ca_3(PO_4)_2$ [18, 31, 35, 36]. The formation of

magnesium carbonate is of interest in this thesis. The reaction of hydrogen carbonate ions, HCO_3^-, with magnesium hydroxide leads to the formation of magnesium hydrogen carbonate, $Mg(HCO_3)_2$, which then decomposes to form a stable layer of magnesium carbonate. The intermediate magnesium hydrogen carbonate is thermodynamically unstable at atmospheric levels of CO_2 [37]; it is thus assumed that the hydrogen carbonate form is short-lived and therefore neglected in the forthcoming work, except in Chapter 2. A representation of the overall reaction is

$$CO_2 + H_2O \longleftrightarrow HCO_3^- + H^+, \tag{1.2}$$

$$Mg(OH)_2 + HCO_3^- \longrightarrow MgCO_3 + H_2O + OH^-, \tag{1.3}$$
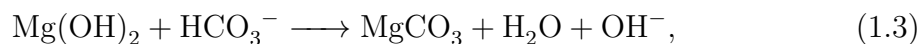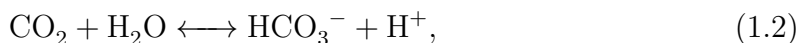
which is demonstrated in [18], where the authors tested the degradation of Mg *in vitro* using cell culture medium with the presence of a hydrogen carbonate buffering system using concentrations reflecting that in the blood (27 mmol/L [38]). This led to the corrosion of magnesium hydroxide via the reaction in equation (1.3). Both the concentration of CO_2 or HCO_3^- can be viewed for the reaction [39], because the stoichiometry for water is the same. In this thesis the conversion of magnesium hydroxide to magnesium carbonate is summarized by [37, 40],

$$Mg(OH)_2 + CO_2 \longrightarrow MgCO_3 + H_2O. \tag{1.4}$$
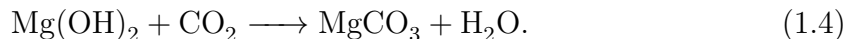
The stable layer of $MgCO_3$ eventually dissolves as it is absorbed into the bone, but due to the time span of studies, accurate information regarding this is unavailable. Consequently, in this work, the carbonate is regarded as the final layer. Equations (1.1) and (1.4) are used as the basis for the model formulation in Chapters 2, 3 and 4.

1.3 Magnesium vs. Other Implant Materials

Titanium (Ti), stainless steel and cobalt-chromium (Co-Cr) and their alloys are the most popular orthopaedic implant materials currently used for fracture fixation, and these are compared to Mg in numerous papers to highlight and discuss why researchers are inclined towards Mg based implants [6, 13, 28]. First and foremost, unlike the current popular materials, Mg is biodegradable. The ability to fully degrade in the human body means that it will save on the expenses and risks incurred when undergoing a second surgery to remove a permanent implant. Such hardware removal can be the cause of an infection, pain, rejection or metal allergy, all of which are usually caused by traditional materials [27, 41], or it could just be the patient's individual choice. Implant removal surgeries are rising. The authors in [10] describe them to be one of the "most frequent" surgical procedures in the western world. In their study they found that implant removal surgery led to a high level of patient satisfaction amongst German patients, and concluded that such surgeries should be carried out as standard while also considering the patient's safety. Hence, it can be reasoned that the traditional use of a biodegradable material is more appropriate for the orthopaedic implant industry.

Traditional implant materials experience some corrosion in body fluids; though this is not as rapid as the corrosion of pure Mg. Nonetheless, the corrosion effects of these implants are not safe because, unlike Mg, they are not tailored to safely degrade in the body [23]. As a result of unsafe degradation, the implants are sometimes removed. Ti alloys are the most popular as they are the most resistant to corrosion [26].

The gradual degradation of a Mg implant in the human body is non-toxic [23], and leads to its complete absorption in the bone while releasing Mg ions into the blood [20]. This biodegradability carries some benefits for the body since Mg is an

essential mineral in the human body, which holds around 21–30g of Mg. It is required for providing normal neurological and muscular function [11, 12]. Mg is found in large amounts in the bone tissue, where more than half of the content in the bone consists of Mg [5]. Furthermore, it is a significant component in encouraging and reinforcing bone growth, while an Mg deficiency in the human body promotes brittle and fragile bones, which leads to osteoporosis [13, 23, 28, 42]. The popular implant materials, Ti, stainless steel, Co-Cr and their alloys, are dormant; in other words their implantation does not provide any benefit to the body like Mg does [23]. Nevertheless, overly large amounts of Mg ions into the blood can potentially cause problems particularly for vulnerable patients. Consequently, Mg in the blood should be observed during orthopaedic implantation [20]. The problem is addressed in this thesis in Chapter 5.

The primary issue with the popular implant materials is the mismatch between their mechanical properties and that of human bone [22]. In contrast, Mg has desirable mechanical properties that are much more comparable to human bone. Mg is a light metal with a specific density of 1.74 g/cm^3, which is close to that of natural bone, (1.8-2.1 g/cm^3 [6, 13]), while traditional implant materials are much less dense. Furthermore, it is well known that Mg is a very structured metal, thereby making it easier to machine and design for implantation [23]. The elastic modulus, compressive yield strength and fracture toughness of Mg are closer to human bone than the traditionally used implant materials (see Table 1.1 for a comparison between Mg, natural bone and Ti [6]). These physical and mechanical qualities eliminate the problem of stress shielding, which is normally ascribed to the application of traditional metallic implants.

Biodegradable implant materials that are currently used in the orthopaedic industry include polymers and ceramics. However, these do not provide the mechanical properties of a metal implant, and for this reason their applications are limited

Properties	Magnesium	Natural bone	Titanium alloy
Density g/cm^3	1.74-2	1.8-2.1	4.4-4.5
Elastic modulus (Gpa)	41-45	3-30	110-117
Compressive yield strength (Mpa)	65-100	130-180	758-1117
Fracture toughness ($MPam^{1/2}$)	15-40	3-6	55-115

Table 1.1: Physical and mechanical properties of magnesium, natural bone and titanium [6].

[28, 43, 44]. Like Mg, Fe is another biodegradable metallic implant that has been investigated [26]. However, the corrosion behaviour of Fe is rapid, and its physical and mechanical properties cannot compete with Mg; therefore, Mg stands out much more to biomaterial researchers [13, 45]. To summarize, literature studies reflect that, aside from its rapid degradation, Mg is a much more advantageous implant material compared to those that are currently used [23].

1.4 Review of *in vitro* and *in vivo* Studies

The degradation of pure Mg implants have been tested against different Mg alloys in many studies, and the various affects of these implants on the human body have also been explored extensively *in vitro* and *in vivo* [18, 30, 32, 36, 46, 47]. *In vitro* trials involve Mg and its alloys being immersed into clinical solutions. Results of these studies are used to guide *in vivo* studies. Some past and recent discoveries are mentioned in this section.

Many research studies stress on the importance of thorough considerations for the choice of alloying components for Mg implants [16, 29, 48]. Typical components are Calcium (Ca), Zinc (Zn) and Aluminium (Al) [16, 23]. Ca and Zn are the most biocompatible elements used to enhance corrosion resistance, and Al enhances the mechanical properties of the implant without increasing the corrosion rate. The most widely studied Mg alloys are combined with Al and Zn [6, 16, 48]. The studies thus far point to Zn as a promising component, whilst Al is more contentious as there is
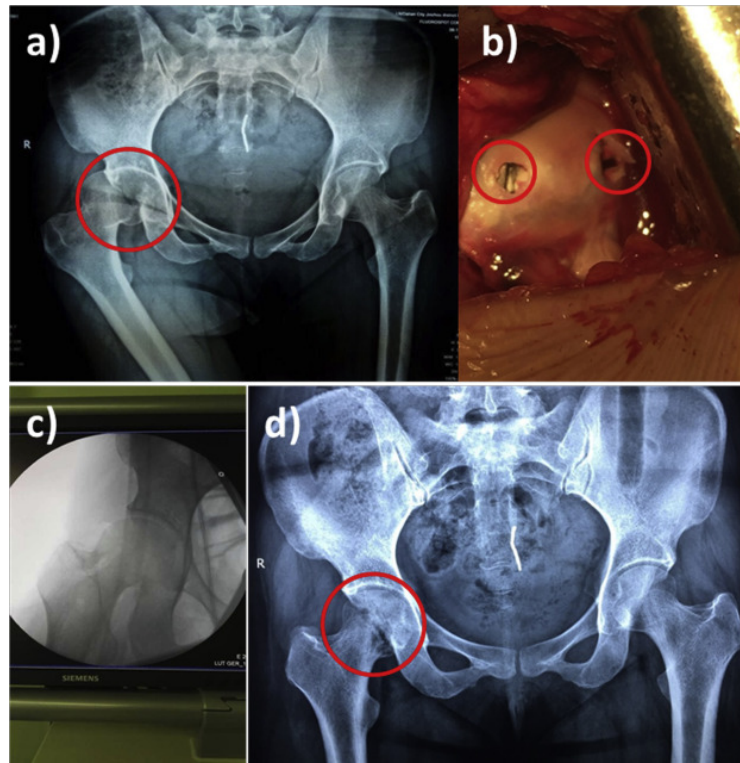
Figure 1.2: Two high purity Mg screws used to treat a femoral head fracture; a) The femoral head was crushed into two parts (red circle); b) the broken femoral head was connected by two Mg screws (red circle); c) X-ray imaging on the day of surgery, which shows that the femoral head was repaired; and d) the femoral head was well restored at 3 months post-surgery. Taken with permission from [3].

potential for side effects, for example researchers have recognised that a growth in Al ion concentration in the brain is related to Alzheimer's disease [16, 23, 48]. The authors in [16] argue that Al containing alloys are not suitable for human implantation, but should instead only be used in experimental studies. Like Zn, Manganese (Mn) is another suitable alloying component, when used in small amounts, due to its tolerance in the human body and its ability to lessen the corrosion caused by impurities within a Mg metal [28]. Furthermore, rare earths (RE) are also popular components for Mg based alloys due to their good mechanical properties and corrosion resistance, but their biocompatibility has raised some concerns [23]. Out of all the RE that have been studied, Mg alloyed with neodymium (Nd) is said to have excellent mechanical

properties with a more slower corrosion rate [48, 49].

Several factors are known to affect the bone response of a Mg implant, such as the pH, surface roughness and surface charge; and further to this, the corrosion effects of Mg can have an impact on various components in the human body. These attributes are examined in many studies [17, 30, 36, 38, 50]. The study in [36] explored the corrosion effects of an Mg-Mn-Zn alloy on the blood composition and organs, as well as on the bone response after 6 months implantation in rats. The authors observed a faster degradation in the bone marrow than in cortical bone. They report that no hydrogen bubbles were perceived around the surrounding tissue after 5 weeks of implantation, which they point out was probably due to the low degradation rate of the alloy [36]; and after a histological analysis, a good compatibility between bone tissue and the alloy was noted. Moreover, a blood examination indicated that the alloy had only a little change in the blood composition and no disorder effect on the organs (liver and kidneys). A fairly recent study investigated how collagen molecules interact with a pure Mg and an Mg-Al-Zn alloy *in vitro* [17]. The pH in the solution, assembly time, electrolytes and material surface roughness were found to have an effect on the collagen monomer structures that were formed on the implant.

Recently, due to the elevated developments in corrosion resistance, Mg and its alloys have been successfully implanted into humans over long-term studies in Germany, China and Korea, where their full degradation was observed [3]. In Germany, Mg-Y-Re-Zr alloy screws were used in the treatment of a hallux valgus (deformity of the big toe), where the surgery showed a positive outcome [51]. Hence, the alloy received recognition in 2013 and became the first Mg implant available to the medical market worldwide for human implantation [52]. Following this the device was employed to treat patients in Ireland and Iran [3]. In 2013, high purity Mg screws were used in China to treat bone flaps in the femoral head of patients, and within

a 1 year follow-up period, the implant proved to be successful [53]. Following this success, the remarkable device was rewarded as an "innovative medical device", which then inspired Chinese researchers to further the use of the implant, where it was applied to a femoral head fracture. The study observed good recovery in the patient 3 months after the surgery, see Figure 1.2. Another human study was conducted in Korea where the implantation of Mg-Ca-Zn screws for radius fractures returned positive results [54]. Consequently, the alloy received recognition in 2015 and became the second alloy available to the medical market worldwide [3].

Despite the growing amount of research into Mg implants for orthopaedic applications, there is a lack of robust tools allowing insights onto the progress of corrosion in a spatial and temporal dependent manner. Further investigations are vital for Mg to become a traditional implant material, particularly using an interdisciplinary approach like that in this thesis. Papers such as [23, 55] also agree that further contributions from different disciplines is a means for studying Mg implants.

1.5 Degradation Models

Mathematical modelling has been applied widely to metal corrosion problems, where studies have investigated a range of metals for the corrosion damage caused by environmental factors such as atmospheric metal corrosion and internal corrosion of pipes [19, 56, 57, 58, 59, 60, 61, 62, 63]. A selection of analytical degradation models for atmospheric corrosion have been reviewed in [59], which aim to predict the thickness loss of a metal whilst taking into account several factors that affect such corrosion like temperature and salinity. A more advanced approach for metal corrosion involves a reaction-diffusion moving boundary model, which is seen in a plethora of studies, some of which are named above, to describe corrosion in, for example, zirconium [62] and steel [61].

Moving boundary problems have a wide range of physical applications that compromise diffusion, for example heat transfer and porous media problems [64]. The most elementary moving boundary problem is the classical Stefan problem for the solidification of a spherical ball of liquid or the melting of a spherical ball of ice [65]. The modelling of the Stefan problem involves the heat equation for the fluid phase, with a boundary condition on the fluid-solid interface setting temperature to that of the melting point and a heat flux condition that accounts for the latent heat in conserving energy that drives the moving boundary (Stefan condition). Much of moving boundary problems in models of this area, including Chapter 3 and 4 in this thesis, use moving boundary conditions similar to the Stefan problem [66].

In this thesis, for Chapter 3 and 4, the modelling approach employs a porous media extension of a moving boundary model that is used to describe the corrosion of a block of copper (Cu) [19, 67]. The corrosion is caused by sulphur dioxide pollution, and the model is built upon the chemical reactions incurred as the copper sample corrodes. The authors first examine the oxidation of copper, which forms a layer of cuprite (Cu_2O), and in an area with small pollution levels, the cuprite acts as a protective layer. However, in areas with moderate or high pollution levels the cuprite is a non-protective layer on the boundary, which reacts with sulphur dioxide, water and oxygen to form a final layer, brochantite $Cu_4(OH)_6SO_4$. The degradation of copper in [19] is modelled with two moving boundaries considering an advection-diffusion flux. Neglecting the advective contribution to the corrosion dynamics results in a Stefan-like model.

The application of mathematical modelling is a "relatively new" concept for medical implants; this explains why magnesium corrosion has been the subject of only a small number of modelling studies, which include [68, 69, 70]. In [68], a simple two phase bulk model of magnesium corrosion was proposed and parameters fitted

to experimental data; however, the model is not explicit in the products of corrosion. A spatially explicit model of a galvanised magnesium implant was proposed in [69]; here, the magnesium block was a fixed domain and they showed that the thickness of the galvanised layer effected corrosion. The authors of [70] used a level-set approach to describe moving interfaces separating a pure magnesium block and a partially corroded phase consisting of dissolved Mg ions, a protective layer of magnesium hydroxide and chloride ions.

1.6 PBPK Models

Physiologically based pharmacokinetic (PBPK) models are used to observe the effects of a synthetic drug or a natural chemical substance in a target organ or the whole body. Its application plays an integral part in drug development to help understand dosing in animals and humans [71, 72]. The models compromise of multiple tissue compartments in the human body which are all connected to the blood [72]. Concentrations of drug in each of the compartments and blood are represented by the state variables that change in time according to, typically, coupled systems of ODEs. Here, each compartment may consist of more evolutionary equations, and are linked to other compartments via the blood state variable. The models are often highly complex due to factors such as the requirement of a large number of state-parameters and the evolution of different time scales. In most applications, analysis is limited to computational only, however, some of these complexities can be overcome by model reduction, which aids their clinical use.

The authors in [73] explain two model reduction techniques, proper lumping and balanced truncation. The proper lumping technique, described in detail in [74], is the most popular [73, 75, 76], and aims to provide a lower dimensional set of the system

via a lumping matrix L that is applied to the original state-variables $\mathbf{x}(t)$, such that

$$\bar{\mathbf{x}}(t) = L\mathbf{x}(t),$$

where $\bar{\mathbf{x}}(t)$ denotes a reduced set of variables [73]. Meanwhile the balanced trunca-tion technique aims to eliminate aspects of the dynamics, in the model, that have a minimal contribution towards the overall input-output relation [73]. A PBPK system is reduced in [77] using singular perturbation theory, where the authors explore a number of timescales to find the meaningful ones in terms of events in their model. In this work, in Chapter 5, singular pertubation is used to reduce the model.

Simple semi-empirical pharmacological models for magnesium containing drugs have been previously studied, such as, for the cardiovascular effects in sheep [78] and for plasma concentrations and blood pressure in pre-eclamptic women [79]; pre-eclamptic women are pregnant women with hypertension and protein in the urine. However, these models are not as physiologically relevant as PBPK models. The PBPK model derived in Chapter 5, is the first to consider magnesium metabolism to aid in understanding the impact of a degrading magnesium implant on blood plasma.

1.7   Thesis Structure

The thesis consists of six chapters including the current one, which introduces the research topic on magnesium corrosion. Chapter 2 starts the modelling work of this thesis with the derivation of an ODE model explaining Mg corrosion. The model is analysed and a numerical solution is obtained. An advection-diffusion model is developed in Chapter 3, which is a substantial part of this work. Chapter 3 commences with a description of how the mathematical model is set-up for Mg corrosion and the assumptions required for the model are also mentioned. The model is derived with initial, boundary and interface conditions for two different cases; these cases

are emphasized in the chapter. The model is analysed and solved numerically, from which a range of results are discussed due to different effects in the model. Chapter 4 adapts the PDE model in Chapter 3 to describe corrosion from inside a Mg pore. The model is analysed and solved in a similar way to that in Chapter 3. The results are then explored for pore corrosion.

In Chapter 5, a PBPK model is derived for Mg transport in the blood. The model is analysed and solved numerically for two scenarios. Chapter 6, the final chapter, concludes the work in this thesis and compromises of a reflection to guide any future work. Additionally, there is an appendix in the thesis, which explains certain aspects of Chapter 3 in detail.

Chapter 2

An ODE Model of Magnesium Corrosion

To begin modelling the corrosion of a magnesium (Mg) block, a simple ODE model is derived in this chapter using the law of mass action to describe the chemical processes of Mg decay. The model considers the physiological interactions during Mg corrosion; these are explained in Section 1.2. After derivation of the model, a steady state analysis is conducted and numerical results are presented.

2.1 Modelling the Problem

In aqueous environments, Mg undergoes a rapid reaction with water to form magnesium hydroxide, $Mg(OH)_2$, and bubbles of hydrogen that evolve in the environment [16]. The $Mg(OH)_2$ undergoes further corrosion due to the physiological environments, where it reacts with bicarbonate ions or CO_2 to form magnesium hydrogen carbonate, $Mg(HCO_3)_2$. The hydrogen carbonate form is short-lived, and decomposes to form a more stable compound magnesium carbonate, $MgCO_3$, H_2O and CO_2

Variable (X)	A	B	C	D	E	F	G
Concentration	Mg	H_2O	$Mg(OH)_2$	H_2	CO_2	$Mg(HCO_3)_2$	$MgCO_3$

Table 2.1: Notation for the concentrations of the corresponding chemicals used in the ODE model.

[18, 37]. The full chemical reactions can be summarized as [18],

$$Mg + 2\,H_2O \xrightarrow{k_1} Mg(OH)_2 + H_2, \tag{2.1}$$

$$Mg(OH)_2 + 2\,CO_2 \xrightarrow{k_2} Mg(HCO_3)_2 \xrightarrow{k_3} MgCO_3 + CO_2 + H_2O, \tag{2.2}$$
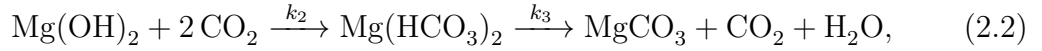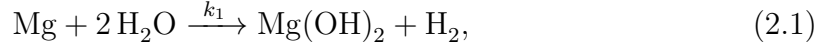
where k_1, k_2 and k_3 are the reaction rate constants. Table 2.1 displays the variables for the concentrations of the chemicals in equations (2.1) and (2.2).

2.2 Mathematical Model

The law of mass action states that the rate of reaction is proportional to the product of concentrations of the reactants [80]. Applying this to (2.1) and (2.2) leads to the following mass balance equations

$$\begin{aligned}
\frac{dA}{dt} &= -k_1 AB^2, \\
\frac{dB}{dt} &= -2k_1 AB^2 + k_3 F, \\
\frac{dC}{dt} &= k_1 AB^2 - k_2 CE^2, \\
\frac{dD}{dt} &= k_1 AB^2, \\
\frac{dE}{dt} &= -2k_2 CE^2 + k_3 F, \\
\frac{dF}{dt} &= k_2 CE^2 - k_3 F, \\
\frac{dG}{dt} &= k_3 F,
\end{aligned} \tag{2.3}$$

Parameter	Description	Dimension
X_0	Initial condition of chemical X	M/L^3
k_1	Reaction rate constant between Mg and H_2O	$(M/L^3)^{-2} t^{-1}$
k_2	Reaction rate constant between $Mg(OH)_2$ and CO_2	$(M/L^3)^{-2} t^{-1}$
k_3	Reaction rate constant for the decomposition of $Mg(HCO_3)_2$	t^{-1}

Table 2.2: Explanation of the parameters, where $X = A, B, ..., G$ are the concentrations, M and L are units for mass and length, respectively.

where t is time. Initial conditions are $X(0) = X_0$, where $X = A, B, ..., G$. See Table 2.2 for an explanation of the model parameters, which are all positive.

In this analysis, the concentration of water is assumed to be constant throughout the duration of Mg corrosion, so $B(t)$ is absorbed into the reaction rate constant k_1 to give k_{10} and $\dot{B} = 0$. For the rest of equations (2.3), the following conservation relations are found

$$\frac{d(A+D)}{dt} = 0 \qquad\qquad \Rightarrow D = A_0 + D_0 - A,$$
$$\frac{d(E - 2A - 2C - G)}{dt} = 0 \qquad \Rightarrow E = E_0 - 2A_0 - 2C_0 - G_0 + 2C + 2A + G,$$
$$\frac{d(A + C + F + G)}{dt} = 0 \qquad \Rightarrow F = A_0 + C_0 + F_0 + G_0 - A - C - G.$$

Further to this, the analysis here assumes to start at the beginning with Mg, H_2O and CO_2 only, and no Mg compounds i.e. $A_0, B_0, E_0 > 0$ and $C_0 = F_0 = G_0 = 0$. This simplifies the conservation expressions, which on substitution into (2.3) gives the following reduced system

$$\frac{dA}{dt} = -k_{10}A,$$
$$\frac{dC}{dt} = k_{10}A - k_2C(E_0 - 2A_0 + 2A + 2C + G)^2, \qquad (2.4)$$
$$\frac{dG}{dt} = k_3(A_0 - A - C - G),$$

where $k_{10} = k_1 B_0^2$; and the initial conditions are

$$A = A_0, \qquad C = C_0, \qquad G = G_0. \tag{2.5}$$

2.2.1   Non-dimensionalisation

The system in (2.4)-(2.5) is rescaled using the following variables

$$\tau = k_3 t, \qquad u_1 = \frac{A}{A_0}, \qquad u_2 = \frac{C}{A_0}, \qquad u_3 = \frac{G}{A_0}, \tag{2.6}$$

and the following dimensionless parameters are introduced

$$\mu_1 = \frac{k_{10}}{k_3}, \qquad \mu_2 = \frac{k_2 A_0^2}{k_3}, \qquad \rho_1 = \frac{E_0}{A_0},$$

leading to the dimensionless system

$$\frac{du_1}{d\tau} = -\mu_1 u_1, \tag{2.7}$$

$$\frac{du_2}{d\tau} = \mu_1 u_1 - \mu_2 u_2 (\rho_1 - 2 + 2u_1 + 2u_2 + u_3)^2, \tag{2.8}$$

$$\frac{du_3}{d\tau} = 1 - u_1 - u_2 - u_3, \tag{2.9}$$

noting that $u_{23} = 1 - u_1 - u_2 - u_3$ is the dimensionless $Mg(HCO_3)_2$ concentration. The initial conditions are

$$u_1(0) = 1, \qquad u_2(0) = 0 \qquad u_3(0) = 0. \tag{2.10}$$

The dimensionless variables u_1, u_2 and u_3 represent concentrations of Mg, $Mg(OH)_2$ and $MgCO_3$, respectively in dimensionless form.

Equation (2.7) is solved using the initial condition in (2.10) to give $u_1 = e^{-\mu_1 \tau}$,

which suggests that the Mg decreases exponentially until it fully corrodes.

2.3 Steady State Analysis

A qualitative analysis of the model is conducted here. Two steady states are found using equations (2.7)-(2.9), these are for the full corroded case

$$(0, 0, 1), \tag{2.11}$$

and the partially corroded case (due to CO_2 exhaustion)

$$(0, 1 - \rho_1, \rho_1). \tag{2.12}$$

The Jacobian matrix is

$$\begin{pmatrix} -\mu_1 & 0 & 0 \\ \mu_1 & -\mu_2(\rho_1 + 2u_2)(\rho_1 + 6u_2) & 0 \\ -1 & -1 & -1 \end{pmatrix}. \tag{2.13}$$

The eigenvalues of (2.13) are found for each steady state using Maple. For (2.11), the eigenvalues are $-1, -\mu_1\rho_1^2, -\mu_1$, which indicate that the steady state is stable. For (2.12), the eigenvalues are $0, -1, -\mu_1$, which indicate partial stability; this is to be expected as this steady state is dependent on the initial CO_2 concentration. When $\rho_1 < 1$, then we expect (A, C, G) to tend to (2.12) as $t \to \infty$ otherwise (A, C, G) tends to (2.11).

2.4 Numerical Simulation

The model in (2.7) - (2.10) is solved numerically in MATLAB using the ODE solver *ode15s*. The reaction rate constants are represented by dimensionless parameters μ_1
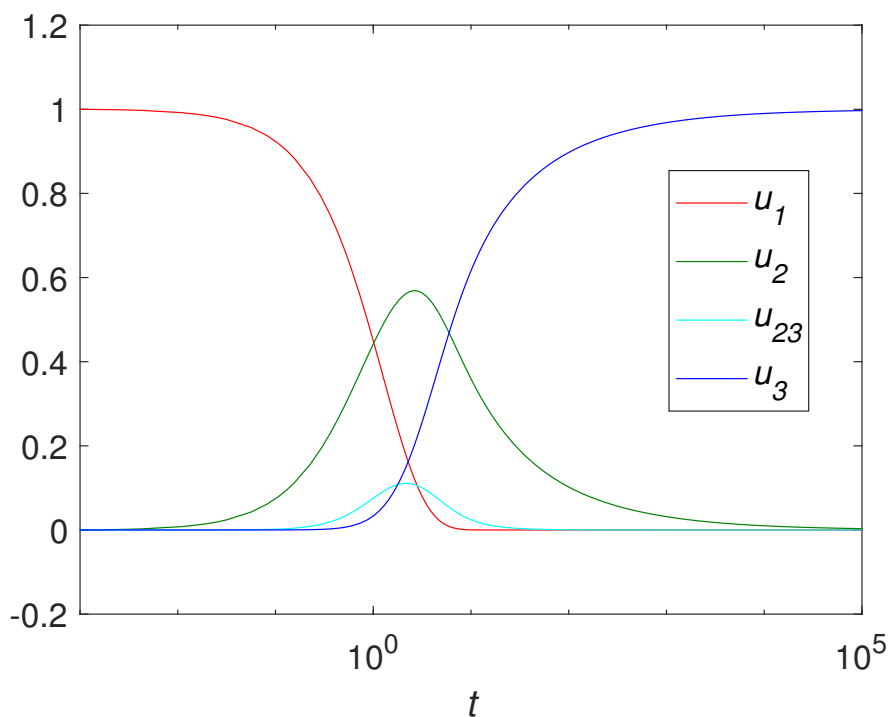
Figure 2.1: Plot of Mg and its compounds over time, u_1, u_2, u_{23}, u_3, when $\mu_1 = 0.80$, $\mu_2 = 0.50$ and $\rho_1 = 1.00$.

and μ_2, which are unknown from the literature. These are experimented with in the simulations. Since the reaction between Mg and H_2O is rapid compared to that between $Mg(OH)_2$ and CO_2, it must be that $\mu_1 > \mu_2$; and since $Mg(HCO_3)_2$ is known to decompose very quickly, μ_1 and μ_2 must be less than 1. The ratio between the initial concentrations of CO_2 and Mg is represented by ρ_1 in the dimensionless model, and this is also experimented with in the simulations to display CO_2 exhaustion.

The result in Figure 2.1 is produced when $\mu_1 = 0.80$, $\mu_2 = 0.50$ and $\rho_1 = 1.00$ (i.e. there is the same amount of Mg and CO_2), and displays u_1, u_2, u_{23} and u_3, over time. It is seen that Mg, u_1, decreases as it is being used up in the reaction, and eventually decays out of the system. Meanwhile, $Mg(OH)_2$, u_2, increases as it is being produced and then begins to decrease as it is consumed more that it is produced, eventually decaying out of the system. The $Mg(HCO_3)_2$, u_{23}, is close to zero throughout; this
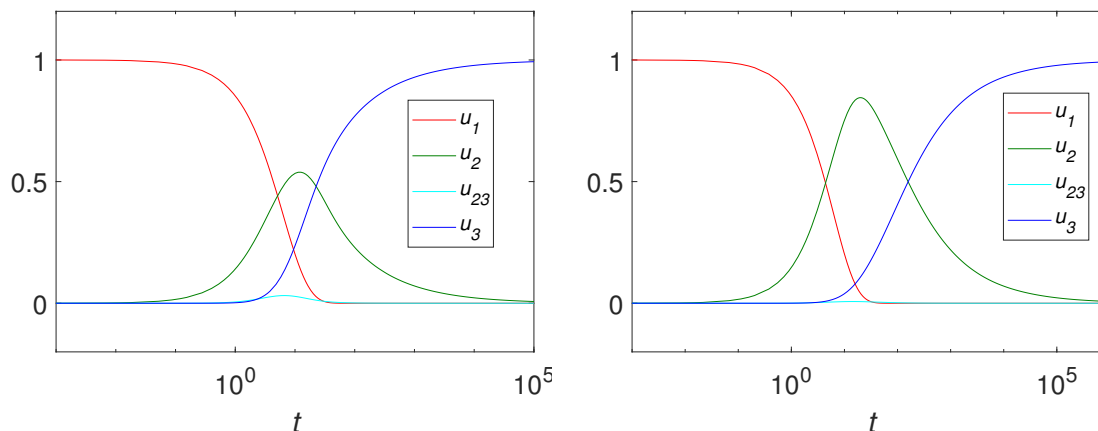
Figure 2.2: Plot of Mg and its compounds, u_1, u_2, u_{23}, u_3, over time when $\mu_1 = 0.16$ and $\rho_1 = 1.00$ with $\mu_2 = 0.10$ (left) $\mu_2 = 0.01$ (right).

reflects the fast decomposition of the compound. The final product $MgCO_3$, u_3, begins to increase slowly at the start, but increases quite rapidly when Mg is low and then eventually slows down to a steady state when the other compounds leave the system.

As μ_1 and μ_2 are decreased then u_{23} is expected to be closer to zero. Figure 2.2 displays results when $\mu_1 = 0.16$ and $\rho_1 = 1.00$ with $\mu_2 = 0.10$ (left) and $\mu_2 = 0.01$ (right); it can be seen that u_{23} is close to zero in these plots than Figure 2.1. In Figure 2.2, when $\mu_2 = 0.01$ u_2 reaches a higher peak, and u_2 and u_3 take longer to reach a steady state as opposed to when $\mu_2 = 0.10$; this is expected since $Mg(OH)_2$ is consumed at a slower rate when μ_2 is decreased.

The steady state analysis in Section 2.3 suggests that CO_2 exhaustion is expected when $\rho_1 < 1$. Figure 2.3 displays the simulation when $\mu_1 = 0.80$, $\mu_2 = 0.50$ and $\rho_1 = 0.80$. It is seen that CO_2 exhaustion leads to u_2 not reaching zero, thereby reducing $MgCO_3$ production.
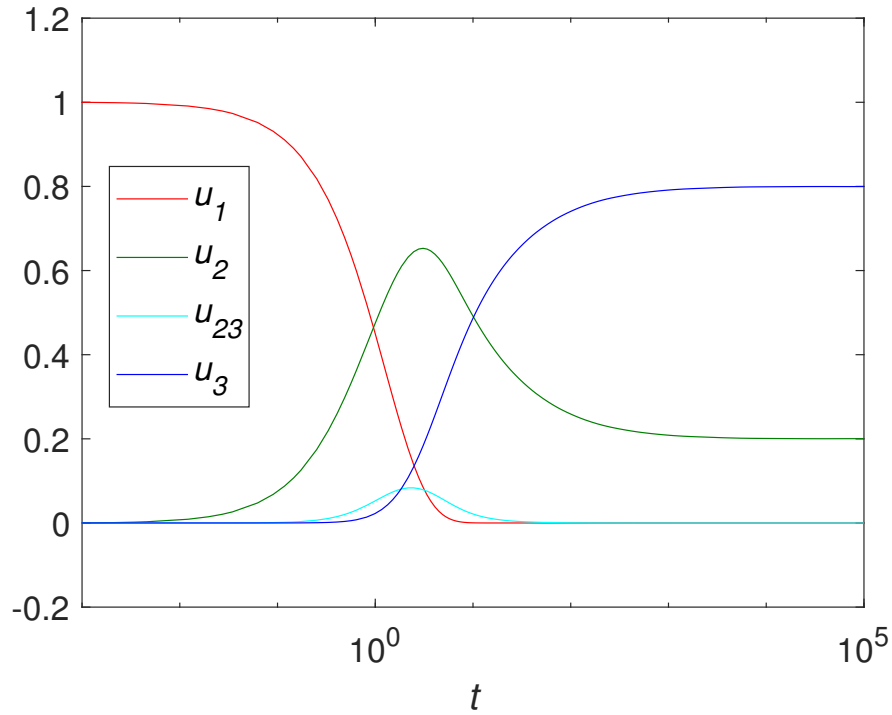
Figure 2.3: Plot of Mg and its compounds, u_1, u_2, u_{23}, u_3, over time when $\mu_1 = 0.80$, $\mu_2 = 0.50$ and $\rho_1 = 0.80$.

2.5 Conclusion

The corrosion of Mg was explained in this chapter through the derivation of a simple ODE model based on chemical interactions between Mg and the physiological environment in (2.1) and (2.2). The model was derived using the law of mass action, and described the rate of change for Mg and its compounds. The corrosion of Mg was described by an exponential decay. Two steady states were identified in the model, these were partially stable and stable. The former referred to CO_2 exhaustion where $Mg(OH)_2$ was not fully consumed, while the latter referred to the final state where only $MgCO_3$ remained in the system.

Numerical simulations were produced for the model, which displayed a logical relationship between Mg and its compounds over time. Adjusting the parameter values,

μ_1, μ_2 and ρ_1, for the model simulations lead to expected results. Exhaustion of CO_2 was perceived when $\rho_1 < 1$, which is in agreement with the steady state analysis. The model provides a good overview for Mg degradation based on the chemical equations. For subsequent chapters, due to the elevated rate of decomposition from $Mg(HCO_3)_2$ to $MgCO_3$, we only assume the corrosion sequence of $Mg \longrightarrow Mg(OH)_2 \longrightarrow MgCO_3$.

Experimental studies, performed by collaborators at the Centre for Biological Engineering at Loughborough University, involved the immersion of small spherical grains of a Mg-Ca alloy into simulated body fluid (SBF) with a 5% CO_2 medium, where the grains were clumped together as close as possible to minimize any gaps. Bearing in mind the set-up of these studies, a spatial model would be more applicable compared to the simple model in this chapter. Thus leading to the development of a PDE model, which is seen in the next chapter.

Chapter 3

A PDE Model of Magnesium Corrosion

As discussed in the introduction, Magnesium (Mg) corrodes rapidly in aqueous environments, which challenges its use as a supporting structure for medical implants. The problem can be addressed by using Mg alloys, protective coatings and purification techniques, but challenges remain at optimising the properties of the material and predicting its adequate mechanical performance. In this chapter, a PDE model is presented to provide a systematic means of quantitatively describing the physio-chemical interactions during Mg corrosion to predict the corrosion rate of Mg with an aim to inform standardisation of *in vitro* investigations of Mg alloy corrosion and implant design parameters for optimal tissue growth and implant absorption. The work in this chapter has also been published in [1].

The modelling approach employs a porous media extension of the model in [19], which was used to describe atmospheric corrosion of a block of copper. In our model, the corrosion of Mg to produce magnesium hydroxide ($Mg(OH)_2$) and magnesium carbonate ($MgCO_3$) are viewed as distinct layers around the Mg sample. This is the first study to consider the latter corrosion product in a magnesium corrosion model.

Another novelty of the model is that it regards the hydroxide and carbonate layers as porous media. The resulting advection-diffusion model with moving boundaries is simplified and non-dimensionalised before being solved numerically using asymptotic expansions to deal with singular cases. The results are displayed and discussed in Section (3.4), and the chapter is concluded in the final section.

3.1 Modelling the Problem

In aqueous environments, the magnesium component of a proposed implant will initially corrode through the following reaction with water

$$Mg + 2\,H_2O \longrightarrow Mg(OH)_2 + H_2, \tag{3.1}$$
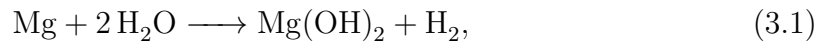
which leads to the production of hydrogen and a protective layer of $Mg(OH)_2$. The hydrogen gas evolves from the solution leaving the hydroxide film on the magnesium surface, which, in physiological environments, is susceptible to further corrosion [30]. In the body fluid or in the presence of a bicarbonate buffering system in cell culture medium, HCO_3^- can react with the hydroxide to firstly form $Mg(HCO_3)_2$, which is short-lived and decomposes to become $MgCO_3$. The intermediate hydrogen carbonate form is neglected in this chapter due to its elevated rate of decomposition. So the transformation of $Mg(OH)_2$ to $MgCO_3$ is summarised as follows [37]

$$Mg(OH)_2 + CO_2 \longrightarrow MgCO_3 + H_2O. \tag{3.2}$$
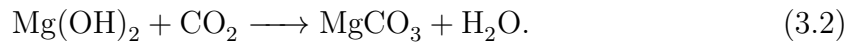
As explained in Section 1.2, either the concentration of CO_2 or HCO_3^- can be viewed since the stoichiometry for water is the same; this work focuses on CO_2. The resulting layer of $MgCO_3$ is more stable and is regarded as the final layer in the model. It is assumed in the model that, throughout the corrosion process of Mg, the environment

is stable (e.g., pH is unchanged, as would be expected in a buffered medium *in vitro*) and that supplies of water and CO_2 are inexhaustible.

The modelling is aimed at explaining the corrosion process of an Mg pellet from the start, through the formation of the hydroxide and carbonate layers, until the Mg and $Mg(OH)_2$ are exhausted and only the $MgCO_3$ remains. The Mg pellet is assumed to be a solid with no pores and corrodes whilst maintaining a smooth surface, i.e. surface pitting and cracking is assumed negligible. Therefore it is envisioned that during the degradation process, the Mg is surrounded by a layer of $Mg(OH)_2$, which in turn is surrounded by a layer of $MgCO_3$, see Figure 3.1. To enable the Mg to corrode further, water must be able to diffuse though the carbonate and hydroxide layers to react the Mg interface, and CO_2 must be able to diffuse through the carbonate layer to reach the hydroxide compound interface. These assumptions lead to a model that describes both the transport and reaction processes of water and carbon dioxide as well as the location of the interfaces between Mg and its constituents, which accumulate on the surface of the Mg as corrosion products. The hydroxide and carbonate layers are treated as porous media, thereby the movement speed of the "solid" components, i.e. the $Mg(OH)_2$ and $MgCO_3$, is different to that of the fluid and dissolved gas components, i.e. H_2O and CO_2; this is a new feature in metal corrosion models.

Radial symmetry is assumed for the modelling process where the model is formulated for a general 1-D geometry, namely Cartesian (describing a magnesium slab), cylindrical (a magnesium rod) and spherical geometry (a magnesium ball). Figure 3.1 shows a cross-section of the cylindrical/spheroid scenarios for the model; the Cartesian case simply has 3 layers bounded by parallel, linear interfaces. Applying the above ideal geometries means that the resulting model will only consider changes in one-spatial dimension.
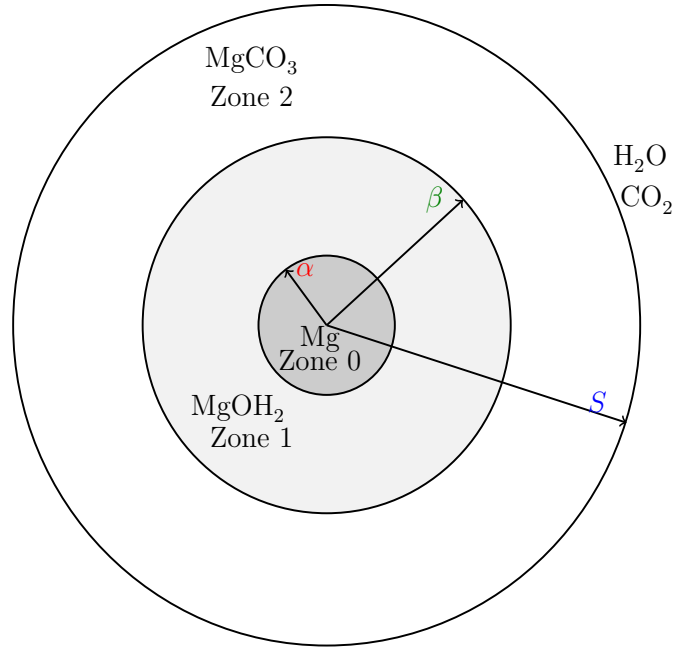
Figure 3.1: A physiochemical schematic of the magnesium corrosion system used in the model for cylindrical and spherical geometries. The pure magnesium exists in the core (Zone 0, $0 \leq r < \alpha(t)$), the magnesium hydroxide forms a middle layer (Zone 1, $\alpha(t) < r < \beta(t)$) and the outer layer consists of magnesium carbonate (Zone 2, $\beta(t) < r < S(t)$).

3.1.1   Model Variables

Writing r as the spatial coordinate and t as the time variable, the moving interfaces are denoted as follows

- $r = \alpha(t)$: the location of the magnesium to magnesium hydroxide interface.

- $r = \beta(t)$: the location of the magnesium hydroxide to magnesium carbonate interface.

- $r = S(t)$: the location of outer edge exposed to concentrations of water and carbon dioxide in the environment.

The spaces between the interfaces are labelled as

- Zone 0: the Mg layer $r < \alpha(t)$.

- Zone 1: the $Mg(OH)_2$ layer $\alpha(t) < r < \beta(t)$.

- Zone 2: the $MgCO_3$ layer $\beta(t) < r < S(t)$.

Also, the mass concentrations of water and carbon dioxide in the pores of the Mg compounds are denoted by

- $W_1(r,t)$: the concentration of water in the $Mg(OH)_2$ layer.

- $W_2(r,t)$: the concentration of water in the $MgCO_3$ layer.

- $C_2(r,t)$: the concentration of carbon dioxide in the $MgCO_3$ layer.

When the hydroxide deposits on the magnesium surface and when the carbonate deposits on the hydroxide surface, the "solid" compounds move with velocities v_{s_i}; and the flow of water and carbon dioxide in the fluid phases are denoted by velocities v_{f_i}, where $i = 1, 2$ corresponds to the zone.

The solid structure of each zone is assumed to be homogeneous, i.e. they consist of a fixed volume fraction of the Mg compound and non-traversable space (ε_i) and traversable space ($1 - \varepsilon_i$); traversable space is defined to be continuous channels of space and excludes completely enclosed gaps in the solid structure. The Mg layer is assumed to be entirely non-traversable, hence $\varepsilon_0 = 1$.

It is assumed that the chemical reactions occur only at the interfaces $\alpha(t)$ and $\beta(t)$, whereby the rate at which these interfaces move depends on the local rate of reaction. Considering the availability of inexhaustible CO_2 *in vitro* or in the physiological environment, it is noted that in the physiochemical representative corrosion system, the Mg and $Mg(OH)_2$ regions will eventually vanish, i.e. $\alpha = 0$ and $\beta = 0$ respectively. This means that there are distinct time phases in the corrosion process that need to be separately handled by the model, and these are defined by $t = T_\alpha$ as the point in time when $\alpha(t) = 0$ (i.e. $\alpha(t) > 0$ for $t < T_\alpha$), and likewise $t = T_\beta$ for

when $\beta(t) = 0$. Once $\beta = 0$, i.e. for $t > T_\beta$, there are no further developments in the system and all that remains is a block of $MgCO_3$.

3.2 Mathematical Model

The diffusion of the fluid and gas components, H_2O and CO_2, throughout the Mg compounds are governed by Fick's law of diffusion, and the transport of the fluid/gas components through the porous medium follows Darcy's law.

With $v_{s_1}(r,t)$ and $v_{s_2}(r,t)$ being the radial velocities of the "solid" phases, the conservation of mass implies

$$\frac{1}{r^d}\frac{\partial}{\partial r}\left(r^d \varepsilon_1\, v_{s_1}\right) = 0 \qquad r \in (\alpha, \beta), \tag{3.3}$$

$$\frac{1}{r^d}\frac{\partial}{\partial r}\left(r^d \varepsilon_2\, v_{s_2}\right) = 0 \qquad r \in (\beta, S), \tag{3.4}$$

where $d = 0, 1, 2$ representing Cartesian, cylindrical and spherical geometry respectively, ε_1 and ε_2 are the solid phase volume fractions for Zone 1 and Zone 2, respectively. These are assumed to be constant in their respective zones so can be divided out. However, the fraction term will be retained in the model derivation for completeness. For simplicity, it is assumed that the fluid phase consists of all non-solid materials and that it is non-compressible. Conservation of total material volume implies that

$$\frac{1}{r^d}\frac{\partial}{\partial r}\left(r^d\left(\varepsilon_i\, v_{s_i} + (1 - \varepsilon_i)\, v_{f_i}\right)\right) = 0,$$

for $i = 1, 2$, hence applying (3.3) and (3.4) gives

$$\frac{1}{r^d}\frac{\partial}{\partial r}\left(r^d(1 - \varepsilon_1)\, v_{f_1}\right) = 0 \qquad r \in (\alpha, \beta), \tag{3.5}$$

$$\frac{1}{r^d}\frac{\partial}{\partial r}\left(r^d(1 - \varepsilon_2)\, v_{f_2}\right) = 0 \qquad r \in (\beta, S). \tag{3.6}$$

where the fluid fractions, $(1 - \varepsilon_1)$ and $(1 - \varepsilon_2)$, for Zone 1 and Zone 2, respectively are constants; so these can be cancelled out in each of the equations. It is noted that the flow here does not encompass that of the fluid/gas trapped in non-traversable pores in the solid structure. The following advection-diffusion fluxes are derived for water and carbon dioxide,

$$
\begin{aligned}
J_{W_1} &= v_{f_1} W_1 - D_W \nabla W_1 & r \in (\alpha, \beta), \\
\left. \begin{aligned} J_{W_2} &= v_{f_2} W_2 - D_W \nabla W_2 \\ J_{C_2} &= v_{f_2} C_2 - D_C \nabla C_2 \end{aligned} \right\} & & r \in (\beta, S),
\end{aligned}
\tag{3.7}
$$

where D_W is the diffusion coefficient of water and D_C is the diffusion coefficient of carbon dioxide. From the fluxes, the following transport equations are attained

$$
\frac{\partial((1 - \varepsilon_1)W_1)}{\partial t} = -\frac{1}{r^d}\frac{\partial}{\partial r}\left(r^d(1 - \varepsilon_1)J_{W_1}\right) \qquad r \in (\alpha, \beta), \tag{3.8}
$$

$$
\left. \begin{aligned}
\frac{\partial((1 - \varepsilon_2)W_2)}{\partial t} &= -\frac{1}{r^d}\frac{\partial}{\partial r}\left(r^d(1 - \varepsilon_1)J_{W_2}\right) \\
\frac{\partial((1 - \varepsilon_2)C_2)}{\partial t} &= -\frac{1}{r^d}\frac{\partial}{\partial r}\left(r^d(1 - \varepsilon_1)J_{C_2}\right)
\end{aligned} \right\} \qquad r \in (\beta, S), \tag{3.9}
$$

where again the fluid fractions, $(1 - \varepsilon_1)$ and $(1 - \varepsilon_2)$ can be divided out.

3.2.1 Initial, Boundary and Interface Conditions

It is assumed that the initial state consists only of a magnesium, and we impose

$$
t = 0: \qquad S(0) = \beta(0) = \alpha(0) = S_0, \tag{3.10}
$$

where the initial thickness or radius $S_0 > 0$. Water and carbon dioxide is sourced at the outer surface $r = S$, which move at speed equal to the local velocity, hence

$$
r = S(t): \qquad W_2 = W_0^*, \quad C_2 = C_0^*, \quad \dot{S} = v_{s2}, \tag{3.11}
$$

where $\dot{S} = dS/dt$, and W_0^* and C_0^* are constant concentrations of water and carbon dioxide on the outer surface. The conditions on the interfaces are more complex and change at critical points of the corrosion process. It is assumed that the reactions occur only at the boundaries. On $r = \alpha(t)$, water reacts with the surface of the magnesium block; the rate of this reaction, R_α, is of utmost importance in this problem. Assuming that the magnesium surface is uniform, then R_α will be dependent on the water concentration and flux there. As two water molecules are consumed, it is assumed by the law of mass action applied to (3.1) that $R_\alpha = kW_1^2$, where k is a rate constant. There are two cases that will be considered in this model

- *Case 1* considers the limit $k \to \infty$, where the reaction is so rapid that water is immediately exhausted on the $r = \alpha(t)$ interface, hence $W_1 = 0$ here. This assumption is most consistent with that when carbon dioxide is exhausted on $r = \beta(t)$. The upcoming boundary conditions (3.12) and (3.14) are relevant for this case.

- *Case 2* considers $k < \infty$, whereby $W_1 > 0$ on $r = \alpha(t)$. In small time, when $1 - \beta(t)/S(t) \ll 1$, the small distance for the carbon dioxide to diffuse means that $Mg(OH)_2$ immediately becomes exhausted on production and Mg converts to $MgCO_3$, in effect, immediately; consequently $\alpha(t) = \beta(t)$ during this transient. See Figure 3.2 for a visualisation of this. In time, the thickness of Zone 2, $S(t) - \beta(t)$, becomes sufficiently large for the reaction to exhaust the carbon dioxide on $r = \beta(t)$, allowing the $Mg(OH)_2$ layer to grow. Let $t = T_{\alpha=\beta}$ be the smallest time at which $C_2(\beta(t), t) = 0$, then for $t < T_{\alpha=\beta}$ the upcoming conditions (3.16) hold, whilst for $t > T_{\alpha=\beta}$ equations in (3.13) and (3.14) are imposed.

Table 3.1 displays the notation used in the model. Let A be the area of a surface element on a magnesium surface. The volume change rate upon this element of the Mg
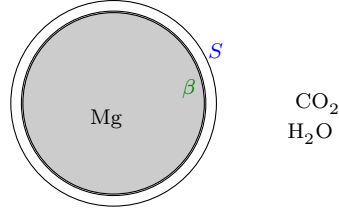
Figure 3.2: Mg decomposition at the start of the problem when $k < \infty$ and $S(t) - \beta(t)$ is very small, where the CO_2 can penetrate the tiny layer of $MgCO_3$ and instantly react the $Mg(OH)_2$ without exhausting the CO_2, hence the hydroxide layer is absent i.e. $\alpha(t) = \beta(t)$.

block is $A\dot\alpha$, translating to a molar change rate of $\mu_0\dot\alpha A$, where $\mu_0 = \dfrac{\rho_0}{M_0}$ with ρ_0 and M_0 being the mass density and mass/mol of Mg, respectively. The water flux through $r = \alpha(t)$ is $(1 - \varepsilon_1)(-W_1\dot\alpha + J_{W_1})$, with its derivation shown in Appendix A.1. So the water molar flux as the boundary moves is $(1 - \varepsilon_1)(-W_1\dot\alpha + J_{W_1})A/M_W = 2\mu_0\dot\alpha A$, since 2 molecules of water are consumed in the reaction at $r = \alpha(t)$. Note that the constant M_W is equal to the mass/mol of water. For the $k \to \infty$ case, this provides the equation for the moving boundary $\alpha(t)$, whilst for $k < \infty$ there is in addition the mass flux through A satisfying $(1 - \varepsilon_1)(-W_1\dot\alpha + J_{W_1}) = -2R_\alpha = -2kW_1^2$. Volume elements are inclusive of the void fraction. The volume fraction difference through converting Mg to $Mg(OH)_2$ is $\omega_\alpha - 1$, where $\omega_\alpha = \mu_0/\mu_1$ because at the interface 1 mole of Mg transforms into 1 mole of $Mg(OH)_2$. Consequently, volume gain rate from the reaction yields $v_{s_1}A = -(\omega_\alpha - 1)\dot\alpha A$, noting that $\omega_\alpha > 1$ implies a gain in volume so that v_{s_1} must have the opposite sign to $\dot\alpha$. The final condition results from a no slip condition to the fluid phase on $\alpha(t)$, i.e. $v_{f_1} = \dot\alpha$. In summary, for $k \to \infty$ the conditions are on

$$
\begin{aligned}
r = \alpha(t) : \quad & W_1 = 0, \\
& v_{s_1} = -(\omega_\alpha - 1)\dot\alpha, \ v_{f_1} = \dot\alpha, \\
& (1 - \varepsilon_1)(-\dot\alpha W_1 + J_{W_1}) = 2\frac{M_W}{M_0}\rho_0\dot\alpha,
\end{aligned}
\tag{3.12}
$$
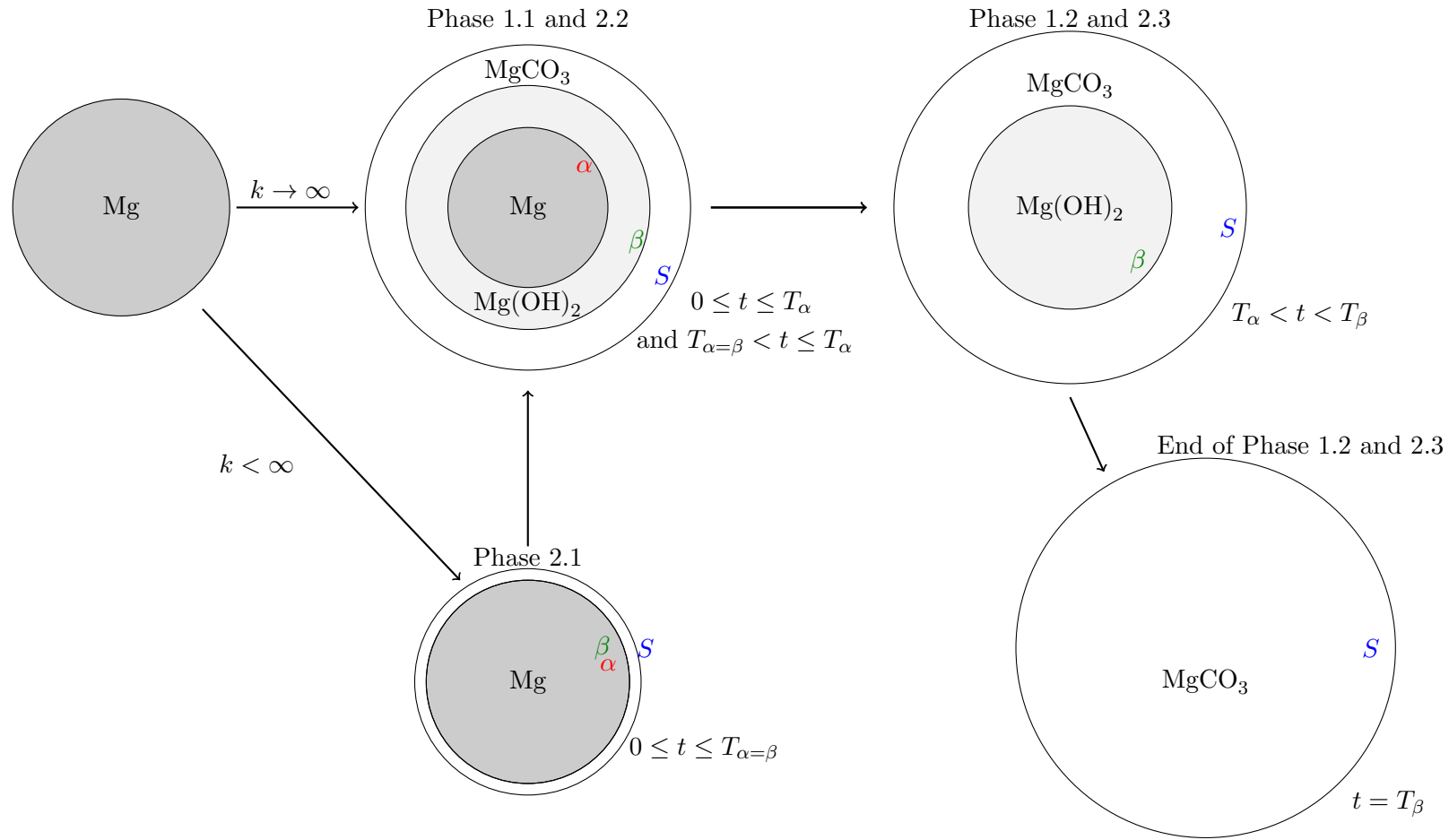
Figure 3.3: Corrosion of Mg from the start of the system for the two cases on k; when $k \to \infty$ Mg decomposes to form layers of $Mg(OH)_2$ and $MgCO_3$ (Phase 1.1), when $k < \infty$ then at small time the hydroxide layer is absent i.e. $\alpha(t) = \beta(t)$ (Phase 2.1) until eventually $Mg(OH)_2$ is present and hence the full system corrodes (Phase 2.2). The process in Phase 1.1 and 2.2 evolves until Mg fully degrades at $t = T_\alpha$, after which only the Mg compounds are present (Phase 1.2 and 2.3); this eventually leads to the full consumption of $Mg(OH)_2$ where only $MgCO_3$ remains thereby ending the system at $t = T_\beta$.

Zone (i)	Domain	Solid fraction	Solid constituent	Mass density	Molecular mass	Mol/Vol	Solid velocity
0	$r < \alpha$	$\varepsilon_0 = 1$	Mg	ρ_0	M_0	μ_0	0
1	$\alpha < r < \beta$	ε_1	$Mg(OH)_2$	ρ_1	M_1	μ_1	v_{s_1}
2	$\beta < r < S$	ε_2	$MgCO_3$	ρ_2	M_2	μ_2	v_{s_2}

Table 3.1: Notation used in the model where $\rho_i = M_i \mu_i$, $\omega_\alpha = \mu_0/\mu_1$ and $\omega_\beta = \mu_1/\mu_2$.

and for $k < \infty$ the conditions are on

$$r = \alpha(t): \quad W_1 > 0,$$

$$v_{s_1} = -(\omega_\alpha - 1)\dot{\alpha}, \ v_{f_1} = \dot{\alpha}, \tag{3.13}$$
$$\frac{M_W}{M_0}\rho_0\dot{\alpha} = -kW_1^2;$$

these conditions hold for $\alpha(t) > 0$. For the cases on k described before, $k \to \infty$ and when $t > T_{\alpha=\beta}$ for $k < \infty$, then on $r = \beta(t)$ the carbon dioxide is assumed to be completely consumed by its reaction with $Mg(OH)_2$, i.e. $C_2(\beta(t), t) = 0$. A water molecule is produced during this reaction, from which it is assumed that the concentration is continuous across the interface, i.e. $W_2(\beta(t), t) = W_1(\beta(t), t)$.

Letting A be again the area of a surface element on $r = \beta(t)$, then the rate of volume loss of $Mg(OH)_2$ is $(v_{s_1} - \dot{\beta})A$ and the molar loss rate is therefore $R_\beta = \mu_1(v_{s_1} - \dot{\beta})A$, where R_β is the reaction rate and $\mu_1 = \rho_1/M_1$ with ρ_1 and M_1 being the mass density and mass/mol of $Mg(OH)_2$, respectively. The water flux through $r = \beta(t)$ is $-(1 - \varepsilon_2)(\dot{\beta}W_2 - J_{W_2}) + (1 - \varepsilon_1)(\dot{\beta}W_1 - J_{W_1})$; the derivation of this is shown in the Appendix A.1. Therefore, the molar flux of the water as the boundary moves is $(1 - \varepsilon_2)(-\dot{\beta}W_2 + J_{W_2})A - (1 - \varepsilon_1)(-\dot{\beta}W_1 + J_{W_1})A/M_W = R_\beta$. Similarly, the carbon dioxide flux on the surface is $(1 - \varepsilon_2)(-\dot{\beta}C_2 + J_{C_2})$, so the molar flux of carbon dioxide as the boundary moves is $(1 - \varepsilon_2)(-\dot{\beta}C_2 + J_{C_2})A/M_C = -R_\beta$, where M_C is the mass/mol of carbon dioxide. The volume fraction difference from the reaction at $r = \beta(t)$ is $\omega_\beta - 1$, by definition, and thus the volume gain rate $A(v_{s_2} - v_{s_1})$ is equal

to $(\omega_\beta - 1)(v_{s_1} - \dot{\beta})A$, where $\omega_\beta = \mu_1/\mu_2 > 1$. The constant $\mu_2 = \rho_2/M_2$ where ρ_2 and M_2 are the mass density and mass/mol of $MgCO_3$, respectively. Conservation of fluid flux across the interface leads to $(1 - \varepsilon_1)(\dot{\beta} - v_{f_1}) = (1 - \varepsilon_2)(\dot{\beta} - v_{f_2})$, which represents the relationship between the net velocities in both magnesium compound regions. The conditions are on

$$
\begin{aligned}
r = \beta(t): \quad & C_2 = 0, \quad W_2 = W_1, \quad v_{s_2} = v_{s_1} - (\omega_\beta - 1)(\dot{\beta} - v_{s_1}), \\
& (1 - \varepsilon_1)(v_{f_1} - \dot{\beta}) = (1 - \varepsilon_2)(v_{f_2} - \dot{\beta}), \\
& (1 - \varepsilon_2)(-\dot{\beta}W_2 + J_{W_2}) - (1 - \varepsilon_1)(-\dot{\beta}W_1 + J_{W_1}) = -\frac{M_W}{M_1}\rho_1(\dot{\beta} - v_{s_1}), \\
& (1 - \varepsilon_2)(-\dot{\beta}C_2 + J_{C_2}) = \frac{M_C}{M_1}\rho_1(\dot{\beta} - v_{s_1}).
\end{aligned}
\tag{3.14}
$$

for $\beta(t) > 0$.

On exhaustion of the pure Mg block and $\alpha(t) \equiv 0$, the boundary conditions for both *Case 1* and *Case 2* are

$$
r = 0: \quad v_{s_1} = 0, \quad v_{f_1} = 0, \quad J_{W_1} = 0.
\tag{3.15}
$$

When $k < \infty$ and $t \le T_{\alpha=\beta}$, Zone 1 is absent. Hence, the boundary conditions are

$$
\begin{aligned}
r = \alpha(t) = \beta(t): \quad & v_{s_2} = -(\omega_\alpha \omega_\beta - 1)\dot{\beta}, \quad v_{f_2} = \dot{\beta}, \\
& (1 - \varepsilon_2)(-\dot{\beta}W_2 + J_{W_2}) = \frac{M_W}{M_1}\rho_1\dot{\beta}, \\
& \frac{M_W}{M_0}\rho_0\dot{\beta} = -kW_1^2, \quad (1 - \varepsilon_2)J_{C_2} = \frac{M_C}{M_1}\rho_1\dot{\beta}.
\end{aligned}
\tag{3.16}
$$

Here, the conversion of Mg to $MgCO_3$ generates a volume fraction difference of $(\omega_\beta \omega_\alpha - 1)$ and the stated condition on v_{s_1} is equivalent to that in (3.12) and likewise for v_{f_1}. The flux condition on water results from the net loss of one molecule from the overall reaction and likewise for CO_2. The current model assumes that $MgCO_3$ will

Phase		time	b.c	v_{s_i} and v_{f_i}
1.1	$k \to \infty$	$0 \leq t \leq T_\alpha$	(3.12), (3.14)	(3.17)
1.2		$T_\alpha < t \leq T_\beta$	(3.15), (3.14)	(3.18)
2.1	$k < \infty$	$0 \leq t \leq T_{\alpha=\beta}$	(3.16)	(3.19)
2.2		$T_{\alpha=\beta} < t \leq T_\alpha$	(3.12), (3.14)	(3.17)
2.3		$T_\alpha < t \leq T_\beta$	(3.15), (3.14)	(3.18)

Table 3.2: Relevant boundary conditions for each of the Mg corrosion phases for the two cases $k \to \infty$ and $k < \infty$, where timescales $T_{\alpha=\beta}$, T_α and T_β represent the smallest points in time when Phase 2.1 ends, $\alpha = 0$ and $\beta = 0$, respectively.

have no exit from the system, so the final state corresponds to when $\beta = 0$, whereby all of the Mg and $Mg(OH)_2$ has been exhausted. The diagram in Figure 3.3 displays the different stages during the corrosion of Mg in the model, where each phase is labelled for the two cases on k. When $k \to \infty$ then we have Phase 1.1 (for $0 \leq t \leq T_\alpha$) and Phase 1.2 (for $T_\alpha < t \leq T_\beta$); and when $k < \infty$ then we have Phase 2.1 (for $0 \leq t \leq T_{\alpha=\beta}$), Phase 2.2 (for $T_{\alpha=\beta} < t \leq T_\alpha$) and Phase 2.3 (for $T_\alpha < t \leq T_\beta$).

Table 3.2 shows the boundary conditions used for the phases in *Case 1* and *Case 2*. Note, in the case $k < \infty$ and $T_\alpha = T_{\alpha=\beta}$, then Phases 2.1 and 2.3 are relevant. Conditions (3.10) and (3.11) are relevant for both of the cases on k.

3.2.2 Exact Solutions

Equations (3.3)-(3.6) are straightforward to integrate, though their solution depends on the various scenarios stated above. For *Case 1*, applying equations (3.12) and (3.14) yields

$$
\begin{aligned}
&v_{s_1} = -\frac{(\omega_\alpha - 1)\, \dot{\alpha}\, \alpha^d}{r^d}, \qquad && v_{s_2} = -\frac{\omega_\beta\, (\omega_\alpha - 1)\, \dot{\alpha}\, \alpha^d + (\omega_\beta - 1)\, \dot{\beta}\, \beta^d}{r^d}, \\
&v_{f_1} = \frac{\dot{\alpha}\, \alpha^d}{r^d}, && v_{f_2} = \frac{(1 - \varepsilon_1)\, \dot{\alpha}\, \alpha^d - (\varepsilon_2 - \varepsilon_1)\, \dot{\beta}\, \beta^d}{(1 - \varepsilon_2) r^d},
\end{aligned}
\tag{3.17}
$$

for $t \leq T_\alpha$; and applying equations (3.15) and (3.14) yields

$$v_{s_1} = 0, \qquad v_{s_2} = -\frac{(\omega_\beta - 1)\,\dot\beta\,\beta^d}{r^d},$$
$$v_{f_1} = 0, \qquad v_{f_2} = \frac{-(\varepsilon_2 - \varepsilon_1)\,\dot\beta\,\beta^d}{(1 - \varepsilon_2)r^d}, \tag{3.18}$$

for $t > T_\alpha$. For *Case 2*, applying (3.16) and (3.14) gives

$$v_{s_1} = -\frac{(\omega_\alpha - 1)\,\dot\beta\,\beta^d}{r^d}, \qquad v_{s_2} = -\frac{(\omega_\alpha\,\omega_\beta - 1)\dot\beta\beta^d}{r^d},$$
$$v_{f_1} = \frac{\dot\beta\,\beta^d}{r^d}, \qquad v_{f_2} = \frac{\dot\beta\,\beta^d}{r^d}, \tag{3.19}$$

for $t \leq T_{\alpha=\beta}$, and the velocities for $T_{\alpha=\beta} < t \leq T_\alpha$ and $t > T_\alpha$ are then the same as that in equations (3.17) and (3.18), respectively. Using the formulation in (3.17) for v_{s_2} and the initial conditions in (3.10), the following is obtained from the boundary condition $\dot S = v_{s_2}(S, t)$,

$$S = S_0\left[-(\omega_\beta - 1)\,(\beta/S_0)^{d+1} - \omega_\beta(\omega_\alpha - 1)\,(\alpha/S_0)^{d+1} + \omega_\alpha\,\omega_\beta\right]^{1/d+1}. \tag{3.20}$$

This formula is correct for $t \leq T_{\alpha=\beta}$ in *Case 2* on insertion of $\alpha = \beta$, and in the final phase for both cases on substitution of $\alpha = 0$. From this the final size, S_∞, of the magnesium carbonate block can be deduced on substitution of $\alpha = \beta = 0$ into (3.20) to give

$$S_\infty = S_0\,(\omega_\alpha\omega_\beta)^{1/(d+1)}; \tag{3.21}$$

this can be calculated *a priori* from the total volume fraction change from converting Mg to $MgCO_3$ being $(S_\infty/S_0)^{1+d} = \omega_\alpha\omega_\beta$.

There are no further exact solutions to be obtained from the full system of equations and variables α, β, W_1, W_2 and C_2 need to be resolved numerically from (3.8),

Parameter	Value	Units	Description	Source
D_W	2.85	cm^2/day	Diffusion coefficient of H_2O	[81]
D_C	1.66	cm^2/day	Diffusion coefficient of CO_2	[82]
M_0	24.3	g/mol	Molecular mass of Mg	P
M_1	58.3	g/mol	Molecular mass of $Mg(OH)_2$	P
M_2	84.3	g/mol	Molecular mass of $MgCO_3$	P
M_W	18	g/mol	Molecular mass of H_2O	P
M_C	44	g/mol	Molecular mass of CO_2	P
ρ_0	1.74	g/cm^3	Mass density of Mg	[83]
ρ_1	2.34	g/cm^3	Mass density of $Mg(OH)_2$	S
ρ_2	2.96	g/cm^3	Mass density of $MgCO_3$	S
W_0^*	1	g/cm^3	Concentration of H_2O in human body	S
C_0^*	0.0011	g/cm^3	Concentration of CO_2 in human body	[84]
w_α	1.79	-	Molar density ratio of Mg and $Mg(OH)_2$	D
w_β	1.14	-	Molar density ratio of $Mg(OH)_2$ and $MgCO_3$	D
ε_1	†	-	Fraction of $Mg(OH)_2$	-
ε_2	†	-	Fraction of $MgCO_3$	-
k	†	$cm^4/g\,day$	Rate of reaction between Mg and H_2O	-

Table 3.3: List of model variables, their interpretation and, where possible, estimated values from the literature. † unknown parameters in the model. "P" derived from the periodic table, "S" indicates standard textbook references and "D" derived from formula in Table 3.1.

(3.9) and (3.10)-(3.16).

Table 3.3 shows the data for each of the parameters in the model. There are three parameters $\varepsilon_1, \varepsilon_2$ and k for which information appears to be limited; these will be investigated further on their effects to the degradation behaviour of magnesium metal and the dynamics of the biphasic corrosion layer.

3.2.3 Non-Dimensionalisation

Of the various candidates for a suitable scaling in time, none stand out as providing any particular advantage here, such that an approximate timescale is chosen for which carbon dioxide diffuses across a reference distance S_0^* (choosing $S_0^* = 1\,cm$). The water and carbon dioxide variables are rescaled with ambient mass concentrations W_0^* and

C_0^* and hence are written as

$$t = \frac{S_0^{*2}}{D_c}\hat{t}, \quad r = S_0^*\hat{r}, \quad W_1 = W_0^*\hat{W}_1, \quad W_2 = W_0^*\hat{W}_2, \quad C_2 = C_0^*\hat{C}_2, \quad \alpha = S_0^*\hat{\alpha},$$

$$\beta = S_0^*\hat{\beta}, \quad S = S_0^*\hat{S},$$

and $v_* = D_C\hat{v}_*/S_0^*$, where the quantities with hats are dimensionless. Using the data in Table 5.3 the scaling implies that $\hat{t} = 1$ represents about 14.5 hours. Let

$$\hat{S}_0 = \frac{S_0}{S_0^*}, \quad \hat{D}_W = \frac{D_W}{D_C}, \quad \gamma_0 = \frac{M_W\rho_0}{M_0W_0^*}, \quad \gamma_1 = \frac{M_W\rho_1}{M_1W_0^*}, \quad \gamma_2 = \frac{M_C\rho_1}{M_1C_0^*}, \quad \kappa = \frac{S_0^*W_0^*}{D_C}k,$$

$$(3.22)$$

noting that ω_α and ω_β are already dimensionless, then, on dropping the hats for clarity, the following system is obtained

$$\frac{\partial W_1}{\partial t} + v_{f_1}\frac{\partial W_1}{\partial r} - \frac{D_W}{r^d}\frac{\partial}{\partial r}\left(r^d\frac{\partial W_1}{\partial r}\right) = 0, \quad (3.23)$$

$$\frac{\partial W_2}{\partial t} + v_{f_2}\frac{\partial W_2}{\partial r} - \frac{D_W}{r^d}\frac{\partial}{\partial r}\left(r^d\frac{\partial W_2}{\partial r}\right) = 0, \quad (3.24)$$

$$\frac{\partial C_2}{\partial t} + v_{f_2}\frac{\partial C_2}{\partial r} - \frac{1}{r^d}\frac{\partial}{\partial r}\left(r^d\frac{\partial C_2}{\partial r}\right) = 0, \quad (3.25)$$

where the velocities for each phase are also non-dimensionalised and appear to be the same as that shown in equations (3.17)-(3.19). Initial conditions are

$$\alpha(0) = \beta(0) = S(0) = S_0. \quad (3.26)$$

For *Case 1*, $\kappa \to \infty$, the boundary conditions are as follows,

$$W_1(\alpha, t) = 0, \quad W_1(\beta, t) = W_2(\beta, t), \quad W_2(S, t) = 1, \quad C_2(\beta, t) = 0, \quad C_2(S, t) = 1,$$

$$(3.27)$$

with the following interface conditions for $t \leq T_\alpha$

$$r = \alpha(t): \quad -(1 - \varepsilon_1)\, D_W\, \partial_r W_1 = 2\,\gamma_0\, \dot{\alpha},$$

$$r = \beta(t): \quad D_W\left((1 - \varepsilon_1)\, \partial_r W_1 - (1 - \varepsilon_2)\, \partial_r W_2\right) = -\gamma_1 \left(\dot{\beta} + \frac{(\omega_\alpha - 1)\, \alpha^d \dot{\alpha}}{\beta^d}\right),$$

$$-(1 - \varepsilon_2)\partial_r C_2 = \gamma_2 \left(\dot{\beta} + \frac{(\omega_\alpha - 1)\, \alpha^d \dot{\alpha}}{\beta^d}\right),$$

$$(3.28)$$

and analytical solution for S

$$S = S_0 \left(\omega_\alpha \omega_\beta - (\omega_\beta - 1)(\beta/S_0)^{d+1} - \omega_\beta(\omega_\alpha - 1)(\alpha/S_0)^{d+1}\right)^{1/(d+1)}; \qquad (3.29)$$

and for $t > T_\alpha$,

$$r = 0: \quad \partial_r W_1 = 0,$$

$$r = \beta(t): \quad D_W\left((1 - \varepsilon_1)\, \partial_r W_1 - (1 - \varepsilon_2)\, \partial_r W_2\right) = -\gamma_1 \dot{\beta}, \qquad (3.30)$$

$$-(1 - \varepsilon_2)\partial_r C_2 = \gamma_2\, \dot{\beta},$$

with analytical solution

$$S = S_0 \left(\omega_\alpha \omega_\beta - (\omega_\beta - 1)(\beta/S_0)^{d+1}\right)^{1/(d+1)}. \qquad (3.31)$$

For *Case 2*, $\kappa < \infty$, the boundary conditions for $t \leq T_{\alpha=\beta}$ are as follows

$$W_2(S, t) = 1, \quad C_2(S, t) = 1, \qquad (3.32)$$

with interface conditions

$$r = \alpha(t) = \beta(t): \quad \gamma_0 \dot{\beta} = -\kappa W_2^2, \quad -D_W\,(1 - \varepsilon_2)\, \partial_r W_2 = \gamma_1\, \omega_\alpha\, \dot{\beta},$$

$$-(1 - \varepsilon_2)\partial_r C_2 = \gamma_2\, \omega_\alpha\, \dot{\beta},$$

$$(3.33)$$

Parameter	Value
D_W	1.5625
γ_0	1.2889
γ_1	0.7225
γ_2	1605.5
w_α	1.79
w_β	1.14
ε_1	†
ε_2	†
κ	†

Table 3.4: List of dimensionless parameter values calculated from the values listed in Table 5.3 and (3.22); † being the free parameters

and analytical solution

$$S = S_0 \left[(\beta/S_0)^{d+1} + \omega_\alpha \omega_\beta (1 - (\beta/S_0)^{d+1}) \right]^{1/(d+1)} ; \tag{3.34}$$

and when $t > T_{\alpha=\beta}$, in addition to equations (3.32) the boundary conditions are

$$\gamma_0 \dot{\alpha} = -\kappa W_1^2, \quad W_1(\beta, t) = W_2(\beta, t), \quad C_2(\beta, t) = 0, \tag{3.35}$$

whereby for $T_{\alpha=\beta} < t \leq T_\alpha$ equations (3.28) and (3.29) are valid, and for $t > T_\alpha$ equations (3.30) and (3.31) are imposed.

Table 3.4 displays the values for the dimensionless parameters used in the model simulations in the next section.

3.3   Numerical Method and Asymptotics

To solve the model numerically, the spatial domains of the system of PDEs (3.23)-(3.25) are mapped to the unit interval $\rho \in [1, 2]$ using the rescaling outlined in Section 3.3.1; this allows an easier numerical scheme because one moving boundary is perceived numerically instead of two, so $r \to \rho$. The difficulties from the singularities

resulting from $\alpha = \beta = S$ at $t = 0$ at the start of Phases 1.1 and 2.1 and $\alpha = \beta$ at $t = T_{\alpha=\beta}$ at the start of Phase 2.2 are discussed in Section 3.3.2.

The system of PDEs in (3.36)-(3.38) and the appropriate boundary conditions for each of the phases was solved using the Method of Lines (MoL) implemented in MATLAB. MoL is a general technique for solving time-dependent PDEs of parabolic type [85]. It converts the PDE system into an ODE system by discretising the spatial derivatives and allowing the time derivative to stay continuous. The domains for Zones 1 and 2 are divided into a uniform mesh, not necessarily using the same number of points, and the spatial derivatives are discretised using central differences; upwind scheme for the advection terms were also implemented but the code usually ran slightly slower. The stiff ODE solver, *ode15s*, was used for the time stepping process. More on the numerical scheme can be found in Appendix A.2.

3.3.1   Change of Variables

For numerical convenience the two zones, the hydroxide layer, $r \in (\alpha, \beta)$ (Zone 1), and the carbonate layer, $r \in (\beta, S)$ (Zone 2), are each mapped to an interval of unit size using the transformation $(r, t) \rightarrow (\rho, \tau)$, namely

$$r = \alpha + (\beta - \alpha)(\rho - 1), \qquad\qquad r \in (\alpha, \beta) \longrightarrow \rho \in (1, 2),$$

$$r = \beta + (S - \beta)(\rho - 1), \qquad\qquad r \in (\beta, S) \longrightarrow \rho \in (1, 2),$$

$$t = \tau.$$

Substitution into equations (3.23)-(3.25) yields

$$\frac{\partial W_1}{\partial \tau} + \frac{1}{\beta - \alpha}\Big(G_1(\rho, \tau) + v_{f_1}\Big)\frac{\partial W_1}{\partial \rho} - \frac{D_W}{(\beta - \alpha)^2}\Big[d_\alpha(\rho, \tau)\frac{\partial W_1}{\partial \rho} + \frac{\partial^2 W_1}{\partial \rho^2}\Big] = 0$$

(3.36)

$$\frac{\partial W_2}{\partial \tau} + \frac{1}{S - \beta}\Big(G_2(\rho, \tau) + v_{f_2}\Big)\frac{\partial W_2}{\partial \rho} - \frac{D_W}{(S - \beta)^2}\Big[d_\beta(\rho, \tau)\frac{\partial W_2}{\partial \rho} + \frac{\partial^2 W_2}{\partial \rho^2}\Big] = 0$$

(3.37)

$$\frac{\partial C_2}{\partial \tau} + \frac{1}{S - \beta}\Big(G_2(\rho, \tau) + v_{f_2}\Big)\frac{\partial C_2}{\partial \rho} - \frac{1}{(S - \beta)^2}\Big[d_\beta(\rho, \tau)\frac{\partial C_2}{\partial \rho} + \frac{\partial^2 C_2}{\partial \rho^2}\Big] = 0 \quad (3.38)$$

where

$$G_1(\rho, \tau) = (\dot{\alpha} - \dot{\beta})(\rho - 1) - \dot{\alpha}, \qquad G_2(\rho, \tau) = (\dot{\beta} - \dot{S})(\rho - 1) - \dot{\beta},$$

$$d_\alpha(\rho, \tau) = \frac{d(\beta - \alpha)}{\alpha + (\beta - \alpha)(\rho - 1)}, \qquad d_\beta(\rho, \tau) = \frac{d(S - \beta)}{\beta + (S - \beta)(\rho - 1)},$$

using the "dot notation" to denote the derivative with respect to τ. For Phases 1.1 and 2.2, the fluid phase velocities are

$$v_{f_1} = \frac{\dot{\alpha}\,\alpha^d}{\big[\alpha + (\beta - \alpha)(\rho - 1)\big]^d}, \qquad v_{f_2} = \frac{(1 - \varepsilon_1)\,\dot{\alpha}\,\alpha^d - (\varepsilon_2 - \varepsilon_1)\,\dot{\beta}\,\beta^d}{(1 - \varepsilon_2)\big[\beta + (S - \beta)(\rho - 1)\big]^d},$$

for Phase 2.1 these are

$$v_{f_1} = \frac{\dot{\beta}\,\beta^d}{\big[\alpha + (\beta - \alpha)(\rho - 1)\big]^d}, \qquad v_{f_2} = \frac{\dot{\beta}\,\beta^d}{\big[\beta + (S - \beta)(\rho - 1)\big]^d},$$

and for Phases 1.2 and 2.3

$$v_{f_1} = 0, \qquad v_{f_2} = \frac{(\varepsilon_1 - \varepsilon_2)\,\dot{\beta}\,\beta^d}{(1 - \varepsilon_2)\big[\beta + (S - \beta)(\rho - 1)\big]^d}.$$

The initial conditions are

$$\tau = 0: \quad \alpha = \beta = S = S_0.$$

For all phases, the following holds

$$W_2(2,\tau) = 1, \quad C_2(2,\tau) = 1. \tag{3.39}$$

For *Case 1*, $\kappa \to \infty$, the conditions for $0 \le \tau \le T_\alpha$ are

$$W_1(1,\tau) = 0, \tag{3.40}$$

$$W_1(2,\tau) = W_2(1,\tau), \tag{3.41}$$

$$C_2(1,\tau) = 0, \tag{3.42}$$

and

$$
\begin{aligned}
&-(1-\varepsilon_1)\frac{D_W}{\beta-\alpha}\,\partial_\rho W_1(1,\tau) = 2\,\gamma_0\,\dot\alpha, \\
&D_W\left(\frac{1-\varepsilon_2}{S-\beta}\,\partial_\rho W_2(1,\tau) - \frac{1-\varepsilon_1}{\beta-\alpha}\,\partial_\rho W_1(2,\tau)\right) = \gamma_1\left(\dot\beta + \frac{(\omega_\alpha-1)\,\alpha^d\dot\alpha}{\beta^d}\right), \\
&-\frac{(1-\varepsilon_2)}{S-\beta}\partial_\rho C_2(1,\tau) = \gamma_2\left(\dot\beta + \frac{(\omega_\alpha-1)\,\alpha^d\dot\alpha}{\beta^d}\right), \\
&S = S_0\left(\omega_\alpha\omega_\beta - (\omega_\beta-1)(\beta/S_0)^{d+1} - \omega_\beta(\omega_\alpha-1)(\alpha/S_0)^{d+1}\right)^{1/(d+1)};
\end{aligned}
\tag{3.43}
$$

and for $\tau > T_\alpha$, equations (3.41), (3.42) and

$$
\begin{aligned}
&\partial_\rho W_1(1,\tau) = 0, \quad D_W\left(\frac{(1-\varepsilon_2)}{S-\beta}\,\partial_\rho W_2(1,\tau) - \frac{(1-\varepsilon_1)}{\beta-\alpha}\,\partial_\rho W_1(2,\tau)\right) = \gamma_1\dot\beta, \\
&\qquad\qquad -\frac{(1-\varepsilon_2)}{S-\beta}\partial_\rho C_2(1,\tau) = \gamma_2\,\dot\beta, \\
&\qquad S = S_0\left(\omega_\alpha\omega_\beta - (\omega_\beta-1)(\beta/S_0)^{d+1}\right)^{1/(d+1)},
\end{aligned}
\tag{3.44}
$$

are imposed. For *Case 2*, $\kappa < \infty$, the conditions for $0 \leq \tau \leq T_{\alpha=\beta}$ are

$$
\gamma_0 \, \dot{\beta} = -\kappa \, W_2(1,\tau)^2, \quad -D_W \frac{(1-\varepsilon_2)}{S-\beta} \partial_\rho W_2(1,\tau) = \gamma_1 \, \omega_\alpha \, \dot{\beta},
$$
$$
-\frac{(1-\varepsilon_2)}{S-\beta} \partial_\rho C_2(1,\tau) = \gamma_2 \, \omega_\alpha \, \dot{\beta}, \tag{3.45}
$$
$$
S = S_0 \left[(\beta/S_0)^{d+1} + \omega_\alpha \omega_\beta (1 - (\beta/S_0)^{d+1}) \right]^{1/(d+1)},
$$

noting $\alpha = \beta$ here; for $T_{\alpha=\beta} < \tau \leq T_\alpha$ the conditions in equations (3.41) - (3.43) are imposed along with

$$
\dot{\alpha} = -\frac{\kappa \, W_1^2(1,\tau)}{\gamma_0}, \tag{3.46}
$$

and for $\tau > T_\alpha$ equations (3.41)-(3.42) and (3.44) are imposed.

The spatial mapping is valid for $0 \leq \alpha < \beta < S$ and gives rise to a singularity at $\tau = 0$ (where $\alpha = \beta = S$) and for *Case 2* at $\tau = T_{\alpha=\beta}$ (where $\alpha = \beta$). This problem is evaded using the small time asymptotic expansions presented in Section 3.3.2.

3.3.2   Small Time Asymptotics

To handle the singularities at $\tau = 0$ and $\tau = T_{\alpha=\beta}$ (for *Case 2*) in the numerical simulation, small time asymptotic solutions of the variables are obtained, which are used to provide approximate initial conditions at a small time increment after the singular time points. For *Case 1*, it is assumed that at the beginning of the system, at $t = \tau_0 \ll 1$, a tiny amount of $Mg(OH)_2$ and consequently $MgCO_3$ is present with a small amount of Mg being used up, hence $\alpha(\tau_0) < S_0$ for $\tau_0 \ll 1$. Furthermore, as $\omega_\alpha, \omega_\beta > 1$, then there will be a small creation of volume, hence $S(\tau_0) > S_0$. Likewise for *Case 2*, $S(\tau_0) > S_0 > \beta(\tau_0) = \alpha(\tau_0)$ at $t = \tau_0 \ll 1$. The relevant phases for this analysis are Phase 1.1, 2.1 and 2.2; these are discussed separately.

Phase 1.1

Phase 1.1 considers *Case 1* when $\tau \leq T_\alpha$. Rearranging the first equation in (3.43) gives

$$\dot{\alpha} = -(1 - \varepsilon_1)\frac{D_W}{2\gamma_0(\beta - \alpha)}\frac{\partial W_1}{\partial \rho}, \tag{3.47}$$

where $\beta - \alpha \ll 1$ for $\tau \ll 1$, and then

$$\dot{\alpha} = O\Big(\frac{1}{\beta - \alpha}\Big),$$

assuming $\dfrac{\partial W_1}{\partial \rho} = O(1)$. We start by seeking expansions of the form

$$\alpha \sim S_0 + a_1\tau^\sigma, \quad \beta \sim S_0 + b_1\tau^\sigma,$$

where $a_1, b_1 = O(1)$ and σ is to be determined. We have $\beta - \alpha = \tau^\sigma(b_1 - a_1)$ and $\dot{\alpha} = \sigma\tau^{\sigma-1}a_1$, so from (3.47) it follows

$$\tau^{2\sigma-1} = 1 \Rightarrow \sigma = \frac{1}{2},$$

consequently, the following small time approximations are applied

$$\alpha(\tau) \sim S_0 + a_1\,\tau^{1/2}, \quad \beta(\tau) \sim S_0 + b_1\,\tau^{1/2}, \quad S(\tau) \sim S_0 + s_1\,\tau^{1/2} \tag{3.48}$$

as $\tau \longrightarrow 0$; $a_1 < 0$ is expected as some Mg will be used up and $s_1 > 0$ as volume is gained from Mg. Substituting these into the model equations (3.36)-(3.38), the

following is obtained at leading order

$$\frac{1}{2\,(b_1 - a_1)}\left(g_1(\rho,\tau) + a_1\,S_0^d\right)\frac{\partial\,W_1}{\partial\,\rho} - \frac{D_W}{(b_1 - a_1)^2}\frac{\partial^2\,W_1}{\partial\,\rho^2} \sim 0, \tag{3.49}$$

$$\frac{1}{2\,(s_1 - b_1)}\left(g_2(\rho,\tau) + \frac{(1-\varepsilon_1)a_1\,S_0^d - (\varepsilon_2 - \varepsilon_1)b_1\,S_0^d}{(1-\varepsilon_2)}\right)\frac{\partial\,W_2}{\partial\,\rho} - \frac{D_W}{(s_1 - b_1)^2}\frac{\partial^2\,W_2}{\partial\,\rho^2} \sim 0, \tag{3.50}$$

$$\frac{1}{2\,(s_1 - b_1)}\left(g_2(\rho,\tau) + \frac{(1-\varepsilon_1)a_1\,S_0^d - (\varepsilon_2 - \varepsilon_1)b_1\,S_0^d}{(1-\varepsilon_2)}\right)\frac{\partial\,C_2}{\partial\,\rho} - \frac{1}{(s_1 - b_1)^2}\frac{\partial^2\,C_2}{\partial\,\rho^2} \sim 0, \tag{3.51}$$

as $\tau \longrightarrow 0$, with

$$g_1(\rho,\tau) = (a_1 - b_1)(\rho - 1) - a_1, \qquad g_2(\rho,\tau) = (b_1 - s_1)(\rho - 1) - b_1.$$

The interface conditions are

$$a_1\gamma_0(b_1 - a_1) + (1-\varepsilon_1)D_W\,\partial_\rho W_1(1,\tau) \sim 0,$$

$$2D_W\left(\frac{1-\varepsilon_1}{b_1 - a_1}\,\partial_\rho W_1(2,\tau) - \frac{1-\varepsilon_2}{s_1 - b_1}\,\partial_\rho W_2(1,\tau)\right) + \gamma_1\left(b_1 + a_1(\omega_\alpha - 1)\right) \sim 0,$$

$$b_1 + \frac{2\,(1-\varepsilon_2)}{\gamma_2\,(s_1 - b_1)}\partial_\rho C_2(1,\tau) + a_1(\omega_\alpha - 1) \sim 0,$$

$$\tag{3.52}$$

and the analytical solution for S is

$$s_1 \sim -[(\omega_\beta - 1)b_1 + \omega_\beta(\omega_\alpha - 1)a_1], \tag{3.53}$$

as $\tau \to 0$. By applying the boundary conditions in (3.40)-(3.42), equations (3.49)-(3.51) are integrated using Maple to give the analytical solution

$$
\begin{aligned}
W_1(\rho, t) &= \frac{W(\lambda_1 - \lambda_2)}{\lambda_1 - \lambda_3}, \\
W_2(\rho, t) &= \frac{(\lambda_4 - \lambda_5)W + \lambda_5 - \lambda_6}{-\lambda_6 + \lambda_4}, \\
C_2(\rho, t) &= \frac{\lambda_7 - \lambda_8}{-\lambda_9 + \lambda_7},
\end{aligned}
\tag{3.54}
$$

where $W = W_1(2) = W_2(1)$ and

$$
\lambda_1 = \mathrm{erf}\left(\frac{a_1(S_0^d - 1)}{\lambda_0}\right), \quad \lambda_2 = \mathrm{erf}\left(\frac{S_0^d a_1 + (\rho - 2)a_1 - b_1(\rho - 1)}{\lambda_0}\right),
$$

$$
\lambda_3 = \mathrm{erf}\left(\frac{S_0^d a_1 - b_1}{\lambda_0}\right), \quad \lambda_4 = \mathrm{erf}\left(\frac{(\lambda_{01} - s_1(-1 + \varepsilon_2))(b_1 - s_1)}{\lambda_{00}}\right),
$$

$$
\lambda_5 = \mathrm{erf}\left(\frac{(b_1 - s_1)(\lambda_{02} + (-1 + \varepsilon_2)((\rho - 2)b_1 - s_1(\rho - 1)))}{\lambda_{00}}\right),
$$

$$
\lambda_6 = \mathrm{erf}\left(\frac{(((\varepsilon_2 - \varepsilon_1)b_1 + a_1(-1 + \varepsilon_1))S_0^d - b_1(-1 + \varepsilon_2)(b_1 - s_1)}{\lambda_{00}}\right),
$$

$$
\lambda_7 = \mathrm{erf}\left(\frac{\lambda_{01} - b_1(-1 + \varepsilon_2)}{2(-1 + \varepsilon_2)}\right),
$$

$$
\lambda_8 = \mathrm{erf}\left(\frac{\lambda_{01} + (-1 + \varepsilon_2)((\rho - 2)b_1 - s_1(\rho - 1))}{2(-1 + \varepsilon_2)}\right),
$$

$$
\lambda_9 = \mathrm{erf}\left(\frac{\lambda_{01} - s_1(-1 + \varepsilon_2)}{2(-1 + \varepsilon_2)}\right),
$$

$$
\lambda_0 = 2\sqrt{\frac{1}{D_W}}\,D_W, \quad \lambda_{00} = 2\sqrt{\frac{(b_1 - s_1)^2}{D_W}}\,D_W(-1 + \varepsilon_2),
$$

$$
\lambda_{01} = (b_1\varepsilon_2 + (-b_1 + a_1)\varepsilon_1 - a_1)S_0^d, \quad \lambda_{02} = ((\varepsilon_2 - \varepsilon_1)b_1 + a_1(-1 + \varepsilon_1))S_0^d.
$$

The equations in (3.52) form a non-linear system of algebraic equations for the unknowns W, a_1 and b_1, which can routinely be solved numerically. Using these solutions along with equations (3.53) and (3.54) the required initial conditions, $\alpha, \beta, S, W_1, W_2$ and C_2, are formulated for small time at Phase 1.1.

Phase 2.1

With $\alpha = \beta$ and $S - \beta \ll 1$ for small time, we have from equation (3.37) and (3.38) $\partial_{\rho\rho}W_2 \sim 0$ and $\partial_{\rho\rho}C_2 \sim 0$ at leading order. Furthermore, as $W_2(2, \tau) = 1$ we anticipate $\dot{\beta} = O(1)$ from the first equation in (3.45). The second and third terms of equation (3.45) imply $\partial_\rho W_2(1, \tau) \sim 0$ and $\partial_\rho C_2(1, \tau) \sim 0$, hence $W_2(\rho, \tau) \sim 1$ and $C_2(\rho, \tau) \sim 1$ at leading order. We write

$$
\begin{aligned}
\beta &\sim S_0 + b_1^{[1]}\tau + b_2^{[1]}\tau^2, \\
S &\sim S_0 + s_1^{[1]}\tau + s_2^{[1]}\tau^2, \\
W_2 &\sim 1 + W_{2_1}^{[1]}(\rho)\tau + W_{2_2}^{[1]}(\rho)\tau^2, \\
C_2 &\sim 1 + C_{2_1}^{[1]}(\rho)\tau + C_{2_2}^{[1]}(\rho)\tau^2.
\end{aligned}
\tag{3.55}
$$

On substitution into (3.45) the following is obtained

$$
\begin{aligned}
b_1^{[1]} &= -\frac{\kappa}{\gamma_0}, \quad b_2^{[1]} = -\frac{\kappa}{\gamma_0}W_{2_1}^{[1]}, \quad s_1^{[1]} = (1 - w_\alpha w_\beta)\,b_1, \\
s_2^{[1]} &= \frac{1}{S_0}(1 - w_\alpha w_\beta)\left(\frac{b_1^{[1]^2}w_\alpha w_\beta\,d}{2} + S_0 b_2^{[1]}\right).
\end{aligned}
\tag{3.56}
$$

Asymptotically expanding equations (3.37) and (3.38) gives $\partial_{\rho\rho}W_{2_1} = 0$ and $\partial_{\rho\rho}C_{2_1} = 0$ at leading order; and using equation (3.45) we obtain $W_{2_1}^{[1]}$ and $C_{2_1}^{[1]}$, and then applying the boundary conditions in equation (3.39) to integrate yields

$$
\begin{aligned}
W_2 &= 1 + \frac{\gamma_1 w_\alpha b_1^{[1]}(s_1^{[1]} - b_1^{[1]})(2 - \rho)}{D_W(1 - \varepsilon_2)}\tau, \\
C_2 &= 1 + \frac{\gamma_2 w_\alpha b_1^{[1]}(s_1^{[1]} - b_1^{[1]})(2 - \rho)}{(1 - \varepsilon_2)}\tau,
\end{aligned}
\tag{3.57}
$$

as $\tau \to 0$. Taking the next order, for (3.37) and (3.38) gives

$$
\begin{aligned}
\partial_{\rho\rho}W_{2_2} &= \frac{2\partial_{\rho\rho}W_{2_1}(s_2^{[1]} - b_2^{[1]})}{(s_1^{[1]} - b_1^{[1]})} + \frac{(s_1^{[1]} - b_1^{[1]})}{D_W}\left[g_2^{[1]} + \frac{(1 - \varepsilon_2)b_1^{[1]}}{(1 - \varepsilon_2)} - \frac{dD_W}{S_0}\right]\partial_\rho W_{2_1}, \\
&= \frac{2\partial_{\rho\rho}W_{2_1}(s_2^{[1]} - b_2^{[1]})}{(s_1^{[1]} - b_1^{[1]})} + \frac{(s_1^{[1]} - b_1^{[1]})}{D_W}\left[(b_1^{[1]} - s_1^{[1]})(\rho - 1) - \frac{dD_W}{S_0}\right]\partial_\rho W_{2_1}, \\
\partial_{\rho\rho}C_{2_2} &= \frac{2\partial_{\rho\rho}C_{2_1}(s_2^{[1]} - b_2^{[1]})}{(s_1^{[1]} - b_1^{[1]})} + (s_1^{[1]} - b_1^{[1]})\left[g_2^{[1]} + \frac{(1 - \varepsilon_2)b_1^{[1]}}{(1 - \varepsilon_2)} - \frac{d}{S_0}\right]\partial_\rho C_{2_1}, \\
&= \frac{2\partial_{\rho\rho}C_{2_1}(s_2^{[1]} - b_2^{[1]})}{(s_1^{[1]} - b_1^{[1]})} + (s_1^{[1]} - b_1^{[1]})\left[(b_1^{[1]} - s_1^{[1]})(\rho - 1) - \frac{d}{S_0}\right]\partial_\rho C_{2_1}
\end{aligned}
$$

where

$$
g_2^{[1]} = (b_1^{[1]} - s_1^{[1]})(\rho - 1) - b_1^{[1]};
$$

hence the advection terms come into play in the τ^2 terms. Taking (3.56), for β, S, and (3.57) for W_2 and C_2, we have the initial conditions for Phase 2.1.

Phase 2.2

This phase occurs after Phase 2.1 when α and β begin to separate at $T_{\alpha=\beta}$. The values of $\alpha = \beta, S, W_2$ and C_2 at $\tau = T_{\alpha=\beta}$ are known from the numerical solution of Phase 2.1. For $0 < \tau - T_{\alpha=\beta} \ll 1$, or $0 < \beta - \alpha \ll 1$, we write

$$
W_1 \sim W_2(1, \tau) + (\beta - \alpha)A(2 - \rho),
$$

where A is an unknown function of W_2, and $\alpha = \alpha_0(\tau) + O(\tau - T_{\alpha=\beta})$, then the first in (3.45) implies that

$$
\dot{\alpha}_0 = -\frac{\kappa W_2^2(1, \tau)}{\gamma_0}, \tag{3.58}
$$

at leading order, implying from the first in (3.43) that

$$-(1-\varepsilon_1)\frac{D_W}{\beta-\alpha}\partial_\rho W_1(1,\tau) \sim 2\kappa W_2^2(1,\tau),$$

resulting with $A = 2\kappa W_2^2(1,\tau)/D_W(1-\varepsilon_1)$ and hence

$$W_1 \sim W_2(1,\tau) + (\beta-\alpha)\frac{2\kappa W_2^2(1,\tau)}{D_W(1-\varepsilon_1)}(2-\rho). \tag{3.59}$$

For the initial part of Phase 2.2, equations (3.37) and (3.38) are solved numerically until $\beta - \alpha$ reaches a given small tolerance, typically $\beta - \alpha = 10^{-3}$, at $t = T_{\alpha=\beta} + \tau_1$ say. Following this the system for Phase 2.2 is solved in the usual fashion starting from time $T_{\alpha=\beta} + \tau_1$ using the updated solutions for W_2, C_2, α, β and S, and by using (3.59) for W_1.

3.4 Results

The results from the numerical solution are displayed and discussed in this section. From the data values listed in Table 3.3, there is current uncertainty on appropriate values for $\varepsilon_1, \varepsilon_2$ and κ (though, to keep the values close to the mid-range, $\varepsilon_1 = 0.6$ and $\varepsilon_2 = 0.4$ were chosen for most simulations). Sections 3.4.2-3.4.5 investigate, for the three principle geometries, the effect of these parameters on the model solutions, in particular on the degradation times of the original Mg block, T_α, and the Mg(OH)_2 layer, T_β. Explored in Section 3.4.3 is the effect of the initial size of the block, which is, of course, an experimentally controllable parameter; for the rest of the simulations the Mg radius is fixed at 1 cm. In Section 3.4.6, the significance of the porous media assumption in the current model is examined.
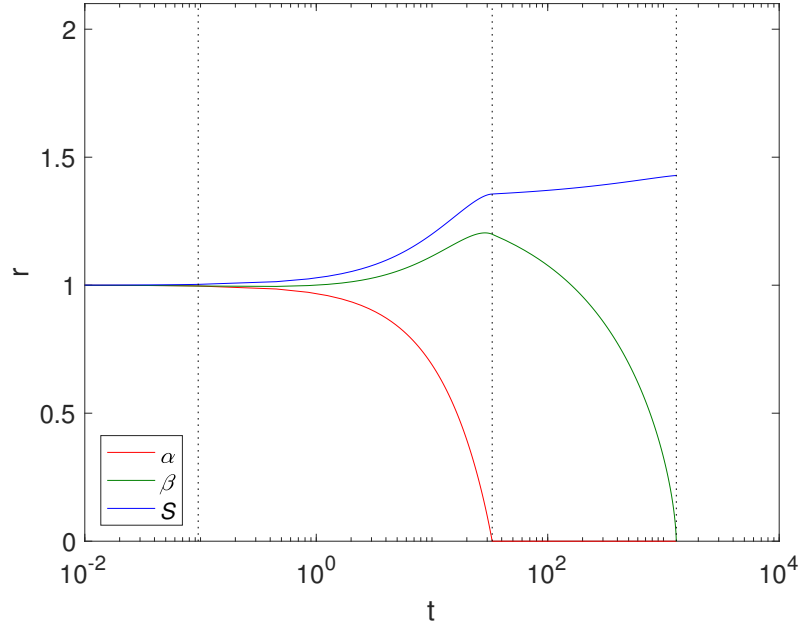
Figure 3.4: Plots of α, β and S against t in cylindrical geometry using $\varepsilon_1 = 0.6$, $\varepsilon_2 = 0.4$, $\kappa = 0.04$, the parameters in Table 3.4 and $S_0 = 1$. The dashed lines show $t = T_{\alpha=\beta}$ (left), $t = T_\alpha$ (middle) and T_β (right).

3.4.1 Magnesium Degradation

An example simulation using a finite reaction rate κ (*Case 2*) is shown in Figure 3.4 using cylindrical geometry, where $\kappa \approx 0.04$, (corresponding to $k = 0.07\,\mathrm{cm}^4/\mathrm{g \cdot s}$ in Table 3.3), $\varepsilon_1 = 0.6$ and $\varepsilon_2 = 0.4$. The size of Mg and its compounds over time are displayed in Figure 3.4 with the dashed lines showing $T_{\alpha=\beta}, T_\alpha$ and T_β. We note that the Mg block degrades relatively quickly at $t = O(10)$, whilst the $Mg(OH)_2$ takes $t = O(10^3)$. This is largely due to a relatively low concentration of CO_2 compared to H_2O in the fluid phase.

Figure 3.5 displays water and CO_2 concentration distribution at the start of Phases 2.1, end of Phase 2.1 ($t = T_{\alpha=\beta}$), Phase 2.2 at the point the full system is solved numerically (see Section 3.3.2), the start of Phase 2.3 ($t = T_\alpha$) and the end of Phase 2.3 ($t = T_\beta$); the times t are detailed in the caption where $\kappa \approx 0.04, \varepsilon_1 = 0.6$ and
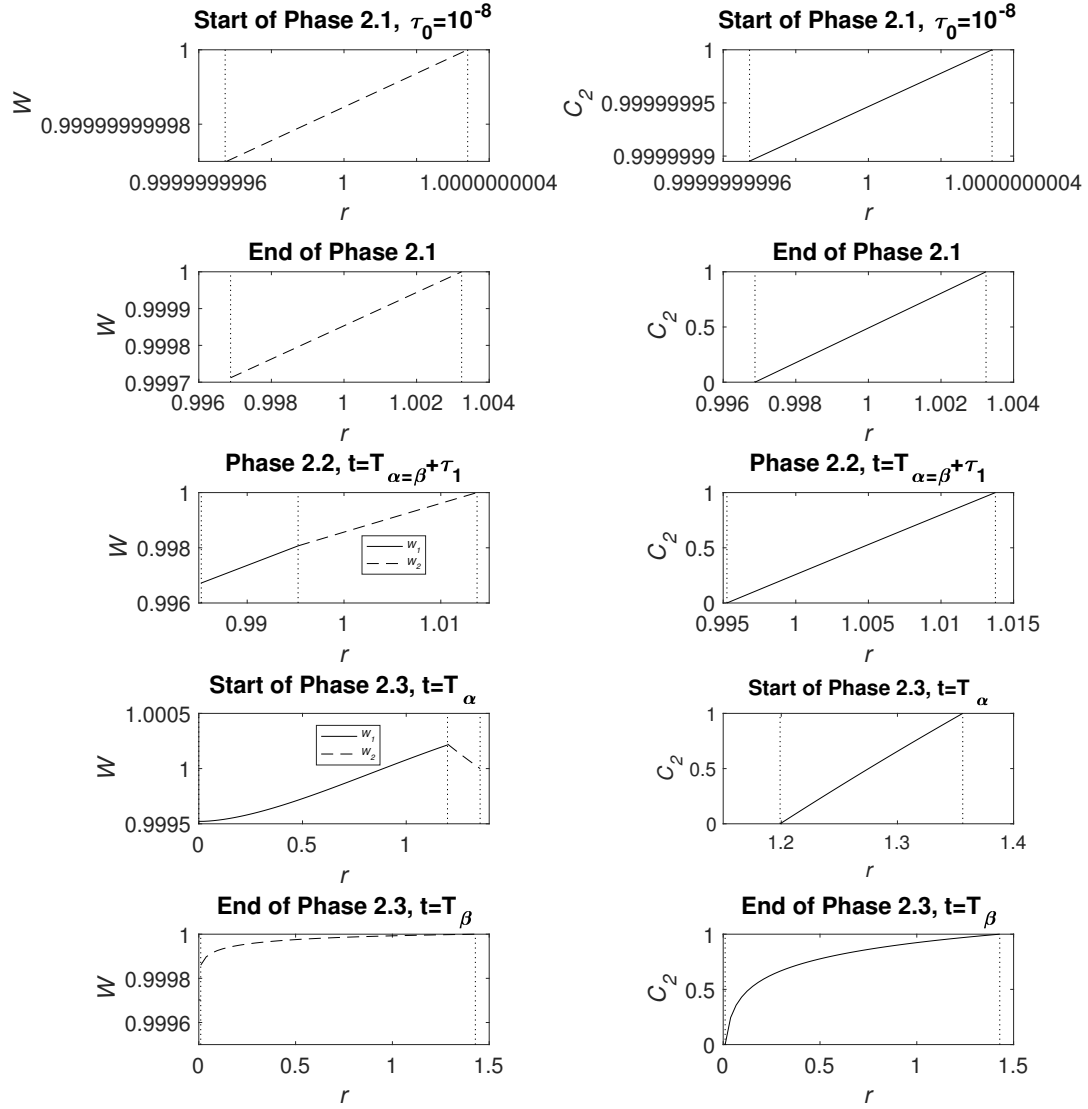
Figure 3.5: Plots of the concentrations W_1, W_2 (left) and C_2 (right) at, from top to bottom, the start of Phases 2.1 ($t = \tau_0 = 10^{-8}$), end of Phase 2.1 ($t = T_{\alpha=\beta} \approx 0.095$), Phase 2.2 ($t = T_{\alpha=\beta} + \tau_1$, with $\tau_1 = 0.356$, see Section 3.3.2), start of Phases 2.3 ($t = T_{\alpha} \approx 33.1$) and the end of 2.3 ($t = T_{\beta} \approx 1291$) in cylindrical geometry. In the left-hand panel, the solid lines are W_1 and the dashed lines W_2. The vertical dotted lines indicate from right to left, $r = S$, $r = \beta$ (right-hand panel, top 2 plots and bottom plot on left-hand panel) and $r = S$, $r = \beta$, $r = \alpha$ (remaining plots on left-hand panel). The parameters are $\varepsilon_1 = 0.6$, $\varepsilon_2 = 0.4$, $\kappa \approx 0.04$, $S_0 = 1$ and the rest listed in Table 3.4.

$\varepsilon_2 = 0.4$. In small time, there is only a very narrow $MgCO_3$ layer present and, as expected, the water and CO_2 are very nearly uniform $r \in (\beta, S)$. Furthermore, CO_2 is not initially exhausted by the conversion reaction of $Mg(OH)_2$ to $MgCO_3$ at $r = \beta$, but in time it descends, reaching zero as Phase 2.2 begins. As time advances clear gradients in concentrations emerge and whilst $\beta - \alpha$ and $S - \beta$ remain small the concentrations of water and CO_2 appear linear. The upward kink in the water distribution is due to production at $r = \beta$ in the above conversion reaction, even exceeding the exterior concentration as, locally, water replaces CO_2 molecules. During Phase 2.3, when there is no more Mg remaining, the water distribution W_1 tends to a uniform distribution via diffusion and the zero flux condition at $r = 0$. By the end of Phase 2.3, the profiles of W_2 and C_2 are no longer linear and CO_2 concentration forms a boundary layer in the vicinity of $r = \beta$.

The solid and fluid phase velocities in the regions are shown in Figure 3.6 at Phase 2.1 (near the start of this phase), end of Phase 2.1 ($t = T_{\alpha=\beta}$), Phase 2.2 (near the start of this phase), start of Phase 2.3 ($t = T_\alpha$) and the end of Phase 2.3 ($t = T_\beta$); the times t and the parameters are detailed in the caption. As expected, due to the direction of movement, the fluid velocities, v_{f_i}, are negative and the solid velocities, v_{s_i}, are positive. When the $Mg(OH)_2$ layer is absent at small time, the velocities are almost uniform $r \in (\beta, S)$. As CO_2 reaches exhaustion at Phase 2.2, the velocities in the hydroxide layer emerge. Near the start of Phase 2.2 whilst $\beta - \alpha$ and $S - \beta$ are small the velocities v_{f_i} and v_{s_i} appear linear. At the start of Phase 2.3, when Mg has fully corroded, the profiles for v_{f_1} and v_{s_1} tend to zero as $r \to \beta$, and by the end of Phase 2.3, v_{f_2} and v_{s_2} tend to a uniform distribution.
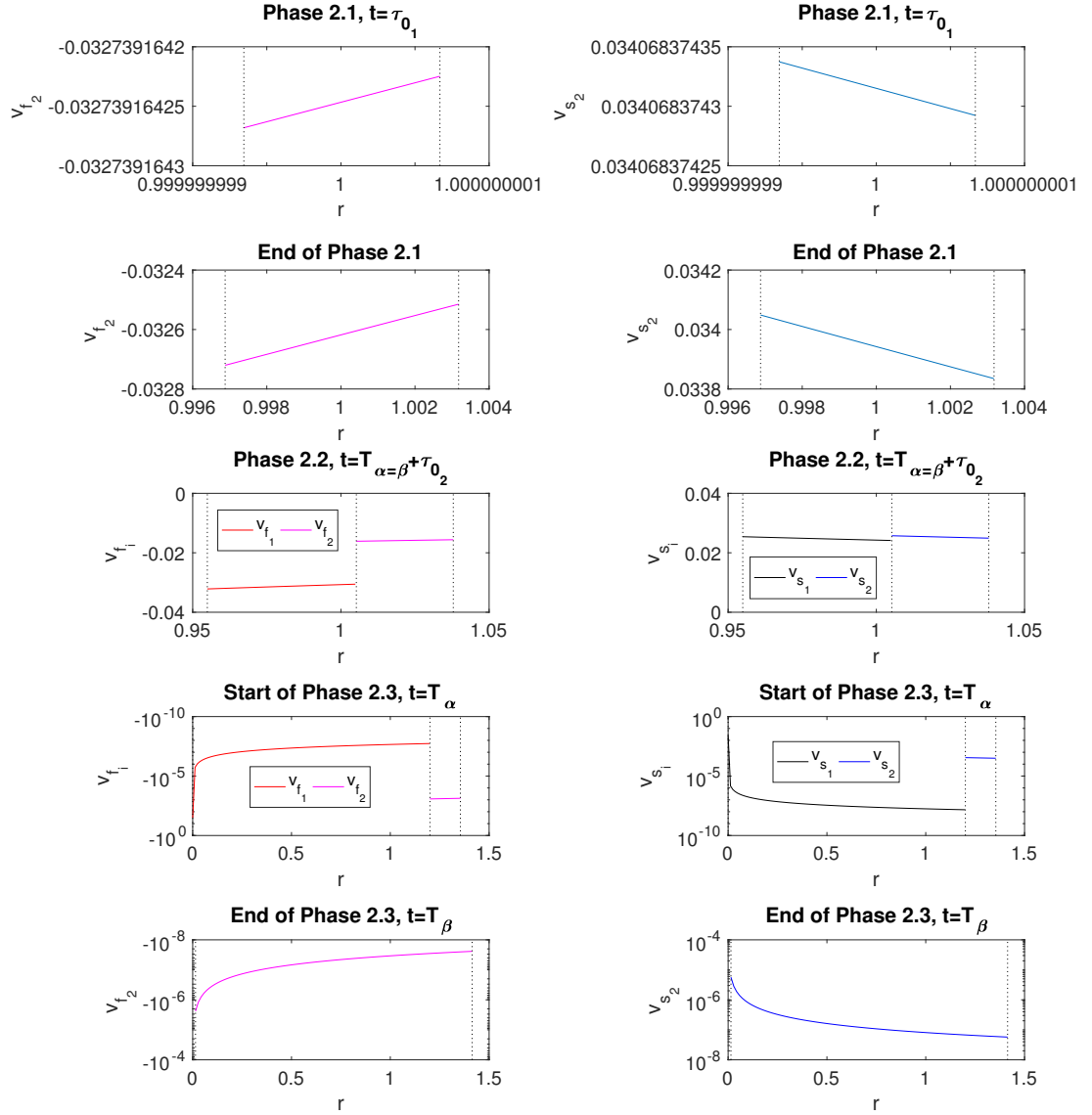
Figure 3.6: Plots of the velocities v_{f_i} (left) and v_{s_i} (right) at, from top to bottom, Phases 2.1 ($t = \tau_{0_1} = 2 \times 10^{-8}$), end of Phase 2.1 ($t = T_{\alpha=\beta} \approx 0.095$), Phase 2.2 ($t = T_{\alpha=\beta} + \tau_{0_2}$, with $\tau_{0_2} = 1.291$), start of Phases 2.3 ($t = T_\alpha \approx 33.1$) and the end of Phase 2.3 ($t = T_\beta \approx 1291$) in cylindrical geometry. In the left-hand panel, the red lines are v_{f_1} and the magenta lines are v_{f_2}; and in the right-hand panel, the black lines are v_{s_1} and the blue lines are v_{s_2}. The vertical dotted lines indicate from right to left, $r = S$, $r = \beta$ (top 2 and bottom row of plots) and $r = S$, $r = \beta$, $r = \alpha$ (remaining plots). The parameters are $\varepsilon_1 = 0.6$, $\varepsilon_2 = 0.4$, $\kappa \approx 0.04$, $S_0 = 1$ and the rest listed in Table 3.4.
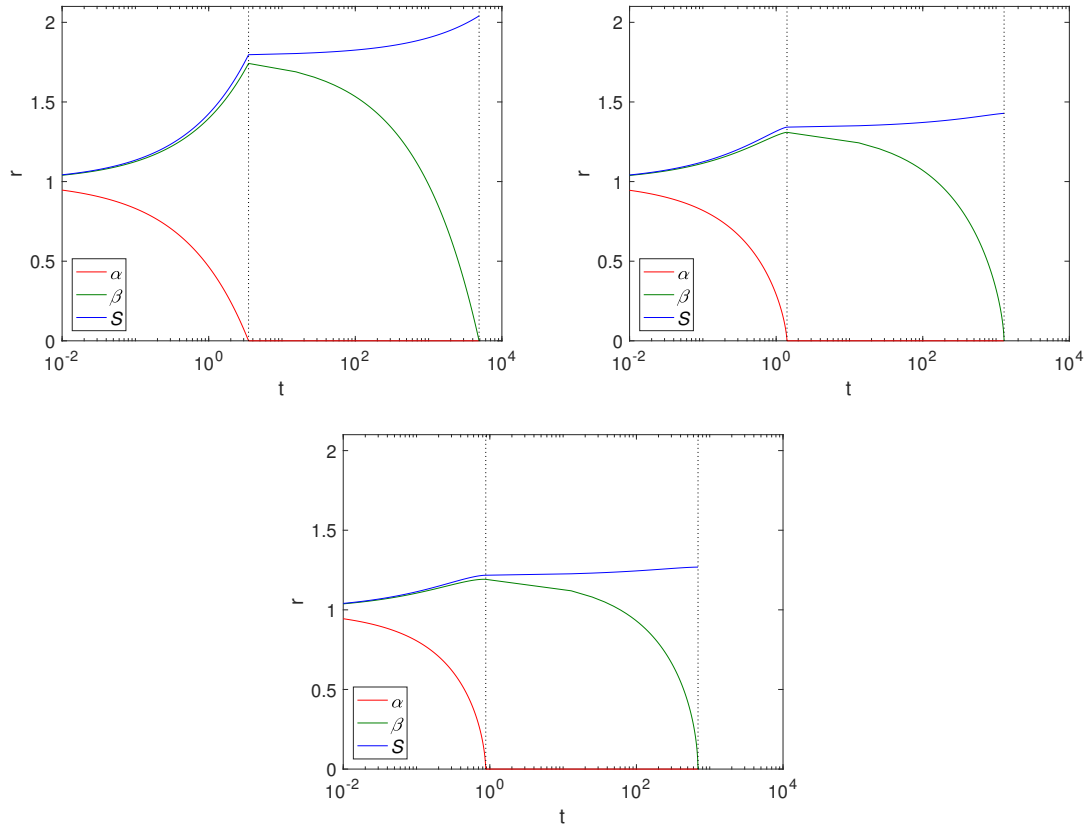
Figure 3.7: Plots of α, β and S against t, from left to right, Cartesian, cylindrical and spherical geometry using $\varepsilon_1 = 0.6$, $\varepsilon_2 = 0.4$, $\kappa \to \infty$, the parameters in Table 3.4 and $S_0 = 1$. The dashed lines show $t = T_\alpha$ (left) and T_β (right).

3.4.2 Effects of Geometry

Figure 3.7 shows α, β and S over time for a *Case 1* ($\kappa \to \infty$) example, using fixed solid fractions, $\varepsilon_1 = 0.6$ and $\varepsilon_2 = 0.4$ and an initial radius of $S_0 = 1$. The results are displayed left to right for Cartesian, cylindrical and spherical geometries. The dashed lines separate the two phases, Phase 1.1 and Phase 1.2. Here, the geometry is such that the size of the Mg block is greater in the Cartesian case, thus there is more of it to convert to $Mg(OH)_2$ and ultimately degrade into $MgCO_3$; as can be seen from the final sizes where $S_\infty^{[d]}$, ($d = 0, 1, 2$ for Cartesian, cylindrical and spherical geometry, respectively), $S_\infty^{[2]} < S_\infty^{[1]} < S_\infty^{[0]}$. Comparing the cylindrical case with that of Figure
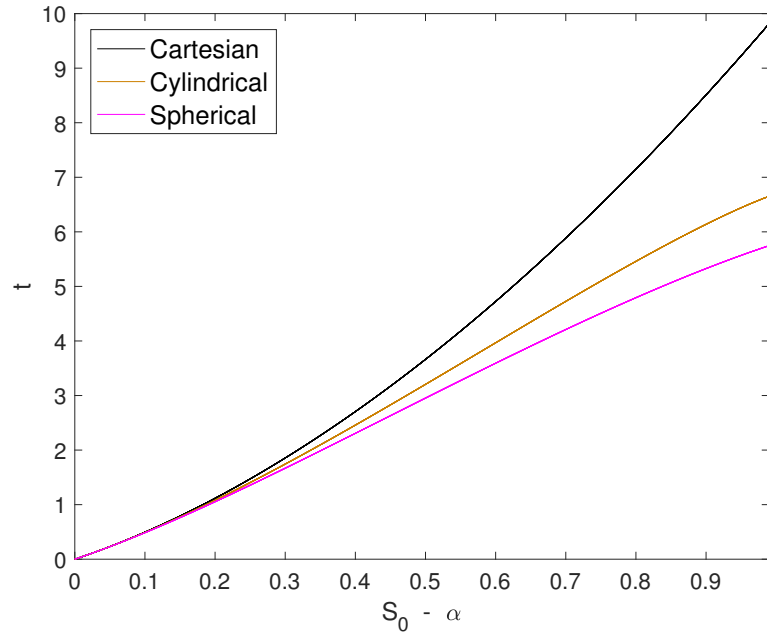
Figure 3.8: Plot of t against the corroded thickness of Mg, $S_0 - \alpha(t)$, in Cartesian, cylindrical and spherical geometry using $\varepsilon_1 = 0.6$, $\varepsilon_2 = 0.4$, $\kappa = 0.3$, the parameters in Table 3.4 and $S_0 = 1$.

3.4, it is observed that, as expected, the magnesium layer disappears much faster in the $\kappa \to \infty$ case ($T_\alpha \approx 1$) than for $\kappa \approx 0.04$ ($T_\alpha \approx 33$); but we note that it does not significantly affect the overall degradation time of $Mg(OH)_2$. In reality, the limit $\kappa \to \infty$ is unlikely to be realistic for pure or mostly pure magnesium, and represents a metal of low purity. However, as degradation of $Mg(OH)_2$ is independent of κ, there is very little difference between the $t = T_\beta$ values.

For *Case 2*, the corroded thickness, $S_0 - \alpha(t)$, of Mg with time is displayed in Figure 3.8 for each geometry, where $\kappa = 0.3$ (corresponding to $k = 0.5\,\text{cm}^4/\text{g}\cdot\text{s}$), $\varepsilon_1 = 0.6$, $\varepsilon_2 = 0.4$ and $S_0 = 1$. Evidently, the corroded thickness of Mg increases as time progresses. As expected, the Mg corrodes quicker in spherical geometry than cylindrical, and both degrade quicker than Cartesian.
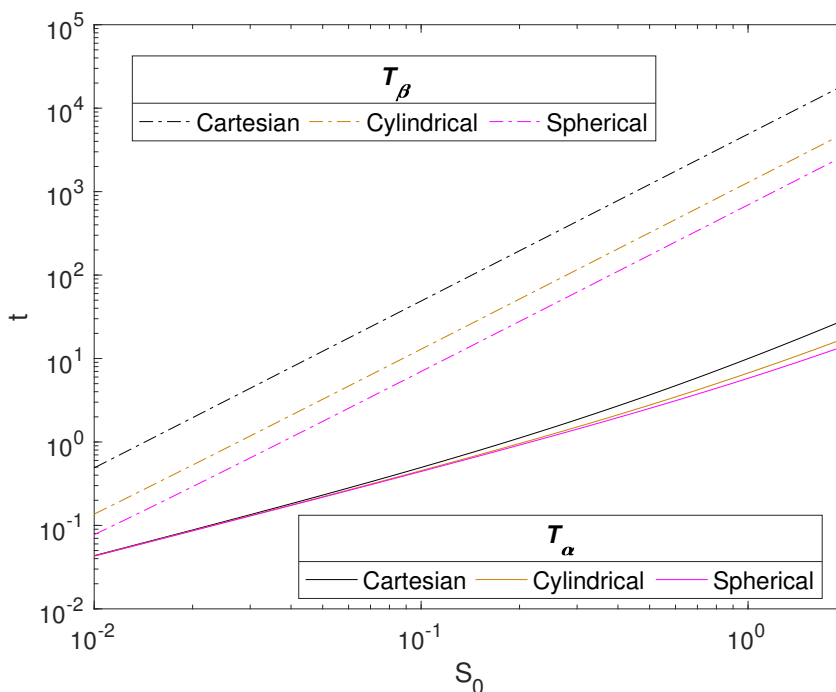
Figure 3.9: Plot of T_α and T_β against the initial magnesium block size, S_0, for each of the principle geometries. The parameters used are $\varepsilon_1 = 0.6$, $\varepsilon_2 = 0.4$, $\kappa \approx 0.3$ ($k = 0.5 \, \text{cm}^4/\text{g day}$) and parameters in Table 3.4.

3.4.3 Effect of Magnesium Block Size

The scaling presented in Section 3.2.3 are such that the initial magnesium block size of $S_0 = 1$, used in the simulations up to now, represents $1 \, \text{cm}$. Figure 3.9 plots the relationship between the initial Mg radius and the key degradation timescales, T_α and T_β, for each of the three principle geometries in a finite κ case. As expected, they show that these timescales increase with the initial radius of the Mg block, S_0. The plots suggests a power law relationship of $T_\beta \propto S_0^2$. This can be justified due to the concentration of CO_2 being relatively small compared to that of water, so that $1 \ll \gamma_2$, and hence the decay of the $Mg(OH)_2$ is slow. Full details are given in

Appendix A.3, where it can be deduced that

$$\frac{d\overline{\beta}}{d\overline{t}} \sim -\frac{(1-\varepsilon_2)}{S_0^2} f(\overline{\beta}, \overline{S}(\overline{\beta})), \tag{3.60}$$

where $f(\overline{\beta}, \overline{S}(\overline{\beta}))$ is independent of S_0; and on solution we obtain

$$T_\beta \sim S_0^2 \frac{B}{(1-\varepsilon_2)}, \tag{3.61}$$

where B is a geometry dependent constant.

3.4.4 Effect of Porosity of the $Mg(OH)_2$ and $MgCO_3$ Layers

In Figure 3.10, the effect of ε_1 (left) and ε_2 (right) on the time scales T_α and T_β is shown for $\kappa = 0.3, 6$ and $\kappa \to \infty$. The top plot of Figure 3.10 shows that T_α increases with the solid fraction, rising sharply as $\varepsilon_1 \to 1$. This is to be expected because as ε_1 increases there is less space for water to flow through the $Mg(OH)_2$ layer, hence decreasing the rate at which water reaches the Mg interface. However the solid fraction does not have an impact on the degradation time for $Mg(OH)_2$ as the transport of CO_2 in the $MgCO_3$ layer governs this process. The figure emphasises the importance of the hydroxide layer at slowing the degradation of the metal core, by impeding the passage of water. The decrease in porosity enhancing longevity is consistent with Sun *et al.* [60].

The bottom plot of Figure 3.10 shows the effects of changing ε_2 whilst keeping ε_1 fixed at 0.6. The solid fraction of $MgCO_3$ does not appear to have an affect on T_α, but does affect T_β. Here, for $t < T_\alpha$, the thickness of the $MgCO_3$ layer, $S - \beta$, is fairly small and appears not to be sufficient to impede significantly the passage of water across it, thus T_α remains approximately constant. Although, T_α varies between the κ values, it is small compared to T_β, and the conversion of $Mg(OH)_2$ to $MgCO_3$ being

independent of κ means the plots are superimposed. As ε_2 increases, it is CO_2 that is impeded by the smaller void fraction leading to the sharp rise in time T_β on $\varepsilon_2 \to 1$. Using the argument in Section 3.4.3 in formulating equation (3.61) for large γ_2, then we expect $T_\beta \propto 1/(1 - \varepsilon_2)$; this relationship matches the numerics very well and suggesting that $T_\beta \to \infty$ as $\varepsilon_2 \to 1^-$.

3.4.5 Effect of Rate of Reaction at Magnesium Interface

Figure 3.11 displays contours of $\log(T_\alpha)$ for a range of values for κ and ε_1 whilst keeping ε_2 constant at 0.4 (top plot), and a range of values for κ and ε_2 whilst keeping ε_1 constant at 0.6 (bottom plot). The variation in the parameter κ reflects different degradation rates across various magnesium alloys. As can be observed from the top plot of Figure 3.11, the longevity of Mg increases as κ and the void fraction $1 - \varepsilon_1$ decreases. In the plot, when $\kappa = O(10^{-3})$ and $1 - \varepsilon_1 = O(10^{-4})$, the longest time that Mg takes to fully degrade is at $T_\alpha = 10^{2.8}$, which is approximately 380 days. This prediction suggests that the model is on the right track, because an implant is preferred to be present for a minimum of 72 days [6]. The lower plot in Figure 3.11 shows that changes in ε_2 do not have an impact on the degradation time of Mg, but a smaller κ lengthens the degradation time of Mg.

Figure 3.12 displays the effects on T_α as κ changes in all three geometries (when $\varepsilon_1 = 0.6$ and $\varepsilon_2 = 0.4$). As expected, the time for the total degradation of pure magnesium increases as the reaction rate diminishes, whilst the curves tend to the *Case 1* solutions as $\kappa \to \infty$. For the reasons outlined in Section 3.4.2, Mg takes the longest time to degrade in Cartesian, then cylindrical and then spherical geometry; though the differences are less noticeable on a logged axis as $\kappa \to 0$.
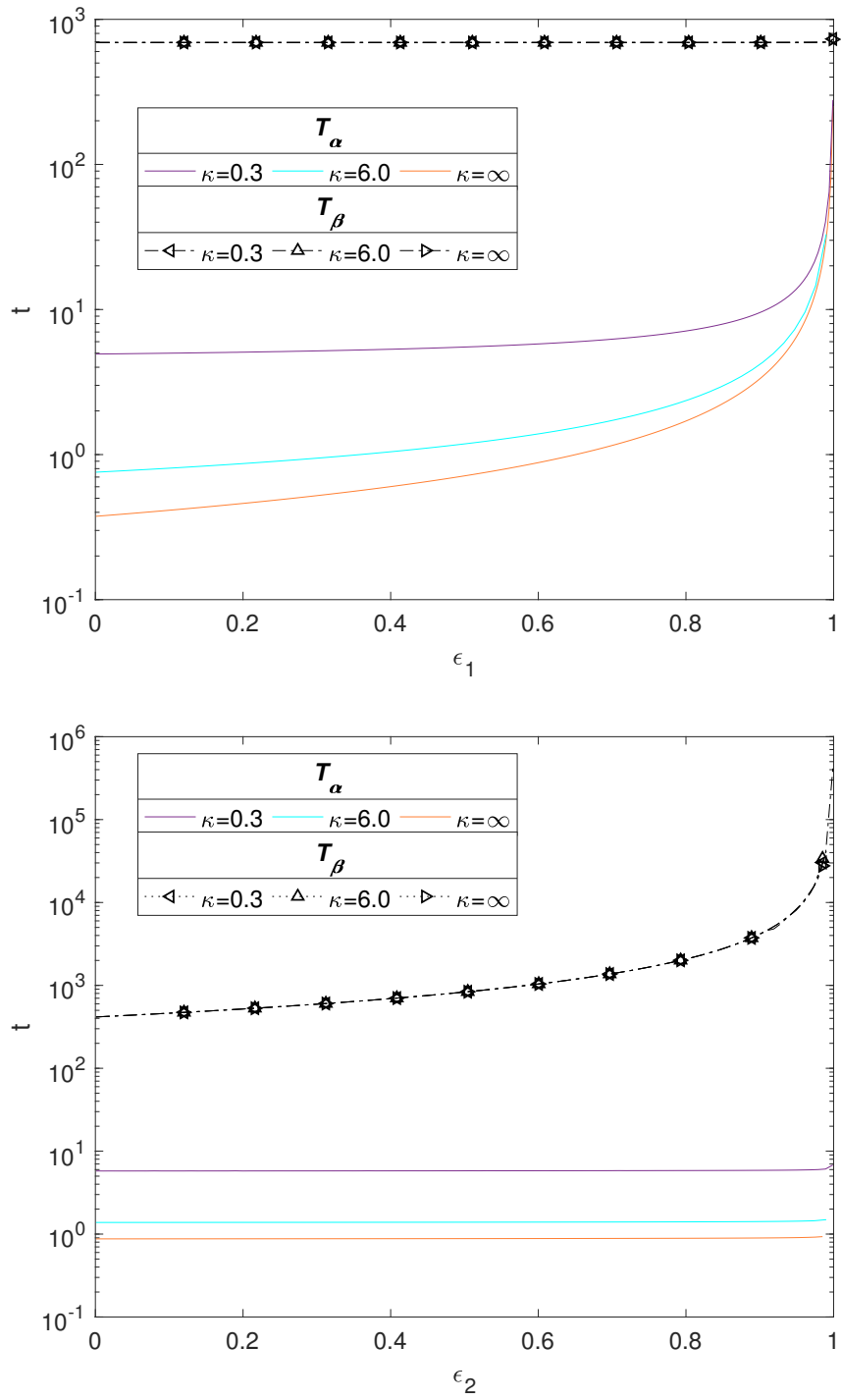
Figure 3.10: Plots of T_α and T_β against ε_1 (top) and ε_2 (bottom) in spherical geometry for $\kappa = 0.3, 6$ and $\kappa \to \infty$, $\varepsilon_1 = 0.6$ (bottom) and $\varepsilon_2 = 0.4$ (top) with the remaining parameters listed in Table 3.4 and $S_0 = 1$.
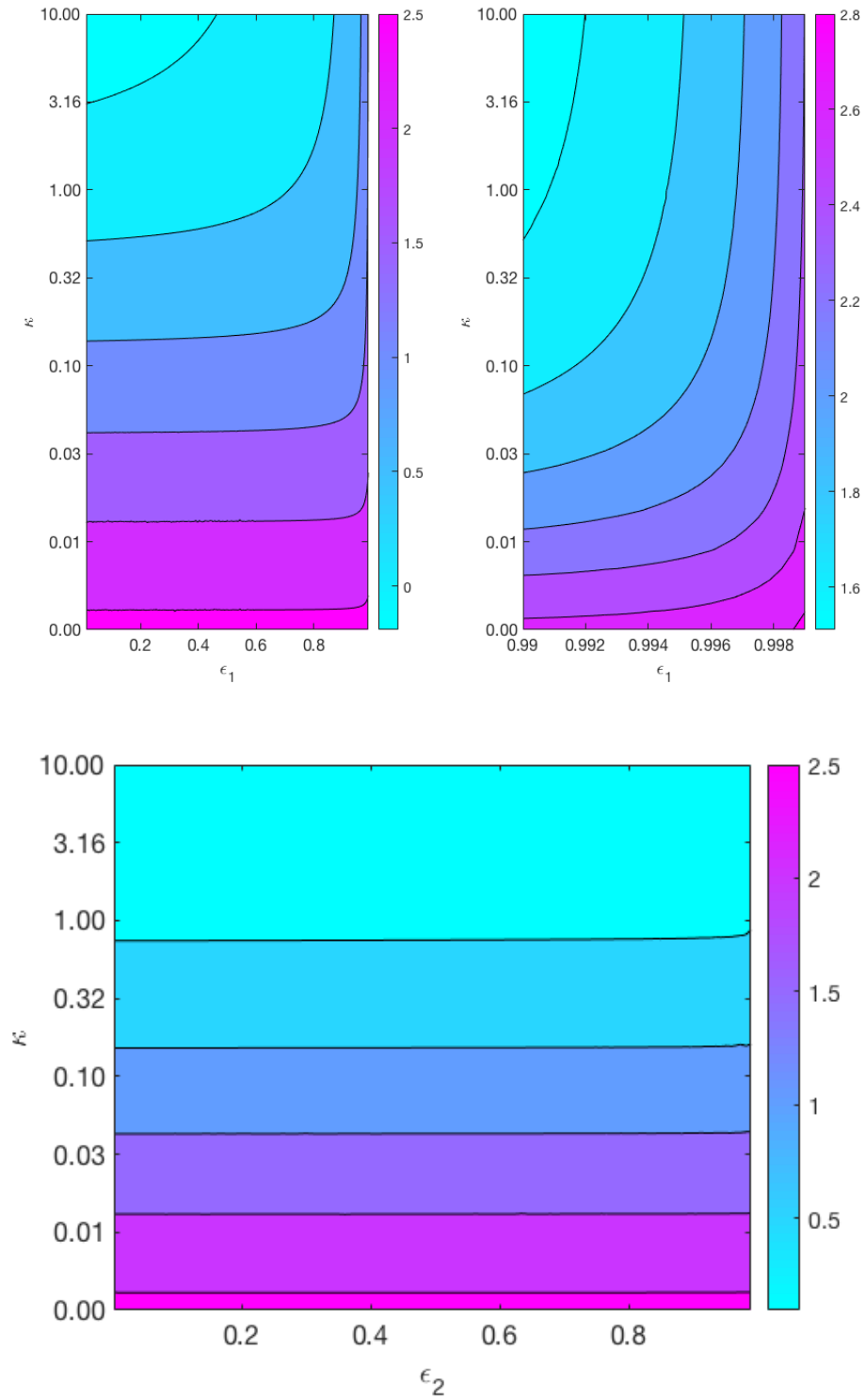
Figure 3.11: Contour plot of $\log(T_\alpha)$ for κ against ε_1 with $\varepsilon_2 = 0.4$ (top) and κ against ε_2 with $\varepsilon_1 = 0.6$ (bottom) in spherical geometry. The remaining parameters are listed in Table 3.4 and $S_0 = 1$.
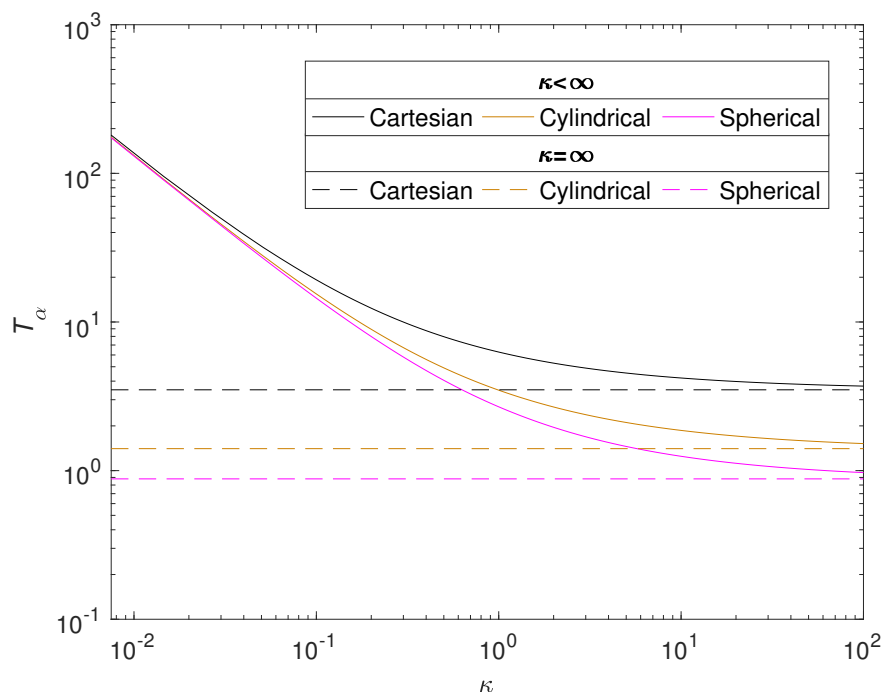
Figure 3.12: Plot of T_α against κ for the 3 principle geometries, with $\varepsilon_1 = 0.6$ $\varepsilon_2 = 0.4$, $S_0 = 1$ and the parameters listed in 3.4.

3.4.6 Role of Advection

The porous media assumption of the corrosion by-products is a novel feature of the current work in metal corrosion studies. The formation of $Mg(OH)_2$ and $MgCO_3$ crystal structures allows transport of water and carbon dioxide through its pores. The separate treatment of the resulting fluid and solid phase velocities is in contrast to [19], in which they assumed that the transport of the diffusive species is supplemented by that of the solid phase motion; this presumably reflects these molecules being somehow connected to and dragged along by the crystal structure. Figure 3.13 compares the evolution of α, β and S from three choices of advective flux velocities, V, of water and CO_2, namely

Case (i). The current model based on porous media assumption ($V = v_{f_i}$, solid lines).

Case (ii). Zero advective transport ($V = 0$, dotted lines), i.e. v_{f_i} set to zero in equation (3.23)-(3.25) and in the boundary conditions.

Case (iii). Advective transport equal to the solid phase velocity, as in [19] ($V = v_{s_i}$, dashed lines), i.e. v_{f_i} swapped with v_{s_i} in equation (3.23)-(3.25) and in the boundary conditions (as used in [19]).

The plots show that there is little difference qualitatively with the results between the cases, and the only visible difference being in the stages up to about $t = T_\alpha$. Mg is predicted to degrade slightly faster using the current model's assumptions ($V = v_{f_i}$) than the zero advection case ($V = 0$) and, in turn, is predicted to be faster than that using $V = v_{s_i}$ as the advection flux. This is due to the signs of the advective fluxes being $v_{f_i} < 0 < v_{s_i}$, as the reactions generate local solid volume increases, since $w_\alpha, w_\beta > 1$. Thus, negative advective flux in case (i) implies that there is a background inward drift of the reactants towards the reaction sites and hence the overall corrosion rates will be predicted to be faster than of case (ii), with zero drift, and case (iii), where the reactants are drawn away by the drift. For $t > T_\alpha$, the differences are maintained, but from the figure, the choice of advective flux appears to have little effect on β in larger time.
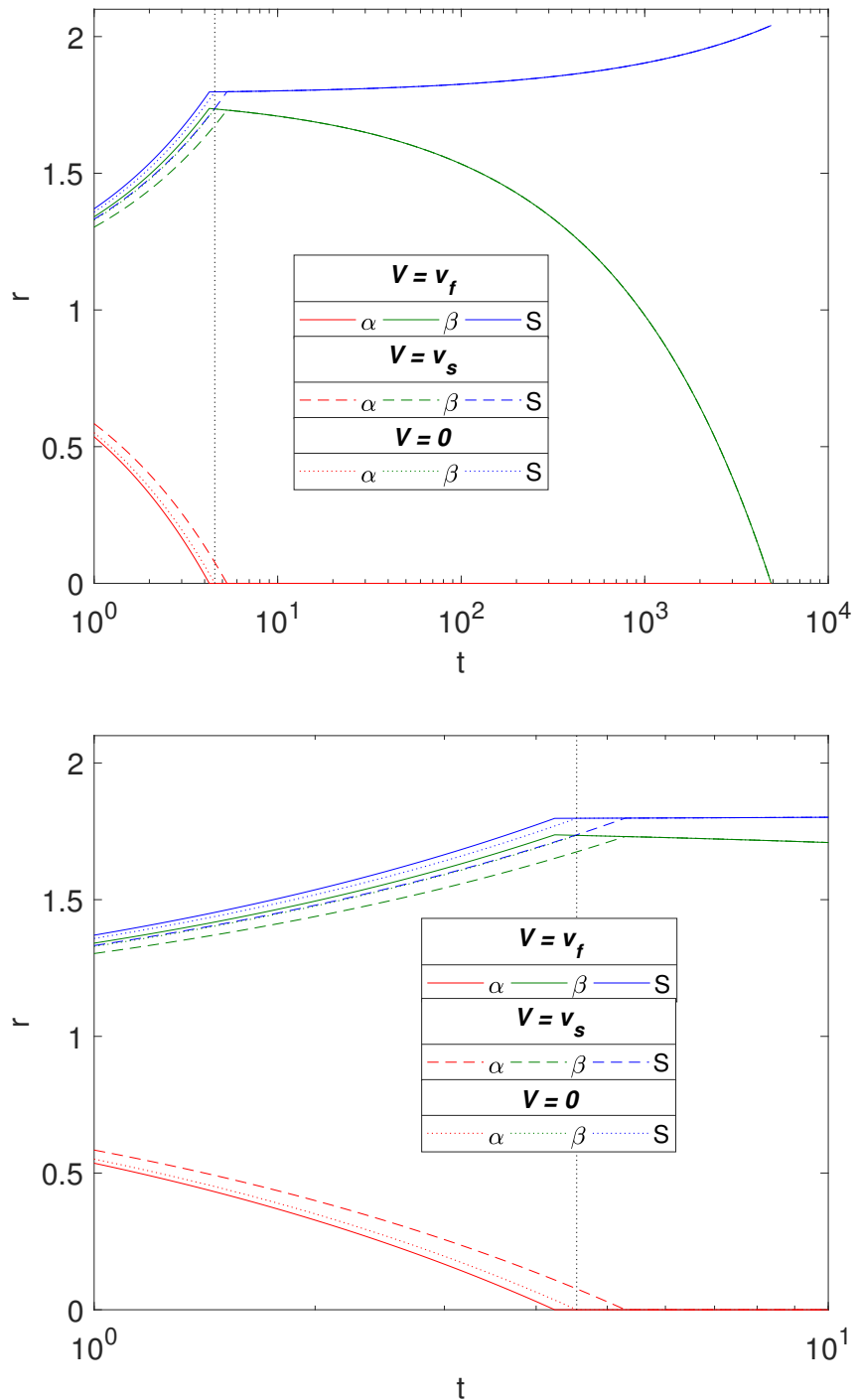
Figure 3.13: Plots of α, β and S resulting from using three choices of fluid and gas phase advection velocities, V, namely $V = v_{f_i}$ (as proposed in the current model, solid lines), $V = 0$ (dotted) and $V = v_{s_i}$ (dashed). The top plot shows the full evolution of the interfaces and bottom plot shows the results around $t = T_\alpha$. The results are in cylindrical geometry, with $\varepsilon_1 = 0.6$, $\varepsilon_2 = 0.4$ and parameters in Table 3.4 and $S_0 = 1$.

3.5 Conclusion

In this chapter, a partial differential equation system, with moving boundaries and interfaces, was used to describe the degradation of a piece of magnesium in aqueous media. This is a first step of modelling degradation of Mg or Mg alloy based orthopaedic implants in biologically relevant environments. The model considers the diffusion and advection of reactants through porous media in the crystal structures generated by reactions with Mg and its constituents. The corrosion products, $Mg(OH)_2$ and $MgCO_3$, are viewed as discrete regions surrounding a block of Mg. Novel features in terms of metal corrosion modelling is the consideration of porous media flow in the crystal structures and the explicit consideration of $MgCO_3$. The model was analysed numerically, but small time asymptotic solutions were needed to deal with singularities at initial and certain time points.

In 1-D, using the classical Cartesian, cylindrical or spherical geometries, a closed system of equations were derived using mass conservation alone. The result of Section 3.4.2 shows that geometry has a significant effect on timescales of Mg degradation and this can impact the shapes of materials used in an implant. For more accurate predictions of corrosion of complex shapes, the problem needs to be studied in two or three spatial dimensions, as has been considered using different modelling approaches in, for example, [60, 70]. The porous media assumption in the current model led to the explicit consideration of solid phase flow, through the manufacture of crystals at the reaction interfaces, and a fluid phase flow to avoid a vacuum. The flow velocities were analytically solvable, and the advective flow of the reactants in the fluid phase do not complicate the model significantly from one that assumes diffusion as the only means of reactant transport.

The investigation in Section 3.4.6 compared results using three different advection assumptions, whereby $V = v_{f_i}$ (current model), $V = 0$ and $V = v_{s_i}$ (used in [19])

representing extreme cases of physically relevant advective velocity V. The results showed that the choice of advection term can notably affect the predicted time of pure magnesium degradation, though in the long term there is only a little difference in the predicted results.

The model consists of three parameters k, ε_1 and ε_2 that are not readily available from the literature. However, there is scope for these parameters to be estimated based on appropriate *in vitro* data and this is discussed further in Section 6.1. The results of Section 3.4.4 and 3.4.5 show that these parameters can be tuned to predict a wide range of results in terms of timescales for the vanishing of pure magnesium, $t = T_\alpha$, and the $Mg(OH)_2$ layer, $t = T_\beta$. At T_β all that remains is a $MgCO_3$ block. The numerical results demonstrated that, over a various parameter values, k and ε_1 affect T_α, whilst having a little effect on T_β. The latter is affected most by ε_2. To substantially prolong Mg presence, Mg alloys must have the effect of reducing the reaction rate k. Another parameter that can be controlled in the model is S_0, which represents the radius of the Mg sample. This was tuned for various values in Section 3.4.3, where it was noted that complete corrosion is described well by the law $T_\beta \propto S_0^2$.

In summary, it was perceived from the numerical results that the model effectively determined the size of magnesium and its corrosion products over time depending on the geometry used along with several other parameters that can be tuned. There is plenty of scope in extending this model to describe corrosion in more physiologically relevant environments; this is discussed in Section 6.1. Nevertheless, the current model provides a promising initial step into a theoretical understanding of how the progress of magnesium corrosion from the implant surface proceeds at a defined spatial and temporal scale.

Chapter 4

Corrosion Inside a Magnesium Pore

In the previous chapter, the degradation of a magnesium (Mg) sample was explored for orthopaedic applications, where the Mg was visualised to be surrounded by layers of its corrosion products, magnesium hydroxide $(Mg(OH)_2)$ and magnesium carbonate $(MgCO_3)$. For simplicity, the Mg sample was assumed to be a solid with no pores while the magnesium compounds were assumed to be porous to allow the reactants to diffuse through, but, in practice, a typical Mg sample used for research into medical implants is preferred to be porous. This is because a porous structure resembles the natural porosity of bone, thus making it more beneficial for absorption into the bone [86]. Hence, there is a growing number of interest in porous Mg structures for regenerative medicine where Mg foams are being fabricated [49].

In this chapter, the corrosion inside a Mg pore is explored using mathematical modelling, where the advection-diffusion model derived in the previous chapter is adjusted here to describe the decomposition of a single pore within a porous structure. During the degradation, Mg will corrode until eventually the pore is totally filled by the corrosion products. The model derived is simplified and non-dimensionalised in
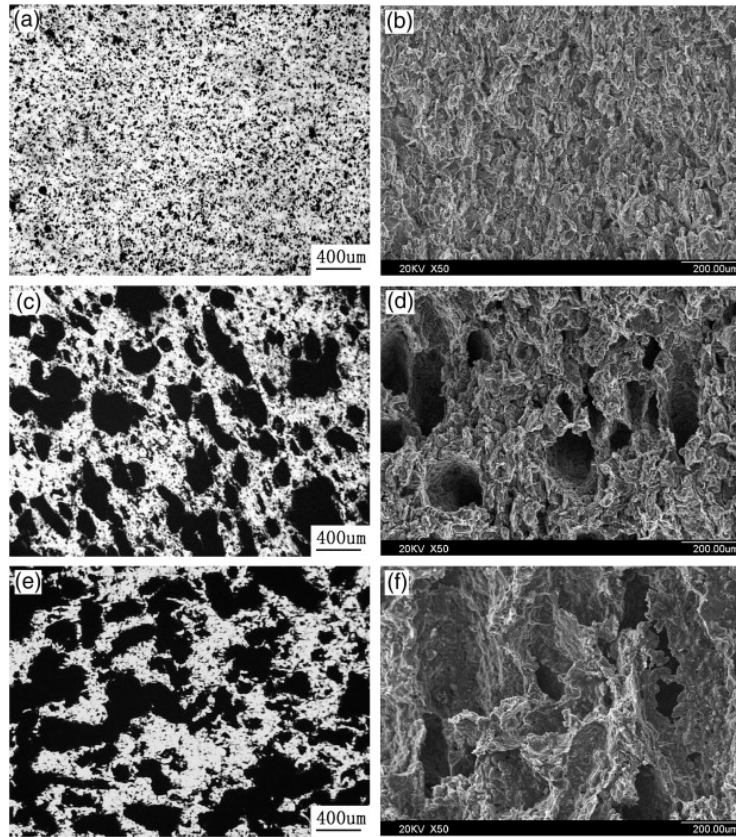
Figure 4.1: Optical and SEM (Scanning Electron Microscope) micrograph images of porous Mg structures with open interpenetrated macropores and small isolated micropores porosities of 7% for (a) and (b), 36% for (c) and (d), 55% (e) and (f), and pore sizes ranging from several µm to 200 - 400 µm; taken with permission from [4].

preparation for the numerical analysis similar to that of the previous chapter. Section 4.5 displays and discusses the results; and the key conclusions are summarized in the final section.

4.1   Background

Ultimately, a bone implant should be "bone-mimicking" not just in terms of mechanical properties, but also in terms of porosity [86]. The porosity of a Mg implant aids its integration with the natural bone tissue [6]. Hence, Mg pores are fabricated using various techniques to investigate how the size, volume and structure of pores impact the features of a corroding implant [4, 45, 87, 88]. See Figure 4.1 for Mg

samples with a range of pore sizes and volumes with two different types of pores, "open interpenetrated macropores" and "small isolated micropores" [4].

The addition of porosity in Mg returns a reduction in the range of mechanical properties [6]. It is mentioned in [6] that a porosity of 97.5% with pore diameter of 4.5mm was reported to have a low yield stress making it inappropriate for load-bearing applications. A study conducted by authors in [88] used a powder metallurgy method to fabricate pores in Mg, and found that a decreasing number of pores and pore size returned an increase in elastic modulus and yield strength [6, 49, 88]. Another study that fabricated pores by a powder metallurgy method, [4], also identified that an increase in pore size and volume yields a lower range of mechanical properties; the authors noted that the porosity has an effect on the overall Mg degradation. Typical pore sizes that have been studied range between 100 and $500\,\mu m$ with high porosity volumes [45]. Nevertheless the authors in [45] highlight that Mg foam fabrication has not been explored widely enough, so optimal porosity parameters are, as of yet, unknown.

4.2   Modelling the Problem

When a porous Mg sample is immersed into clinical solutions or in the body then the biochemical reactants enter the pores; in this case these are water and carbon dioxide. The main reactions are assumed to be the same as those in Chapter 3. The water from within the pore reacts with the Mg through the following reaction

$$Mg + 2\,H_2O \longrightarrow Mg(OH)_2 + H_2, \tag{4.1}$$
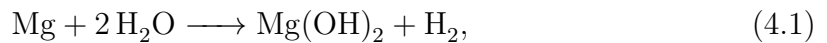
forming a layer of $Mg(OH)_2$ inside the pore with evolving bubbles of hydrogen. The hydroxide layer reacts with the carbon dioxide inside the pore through the following
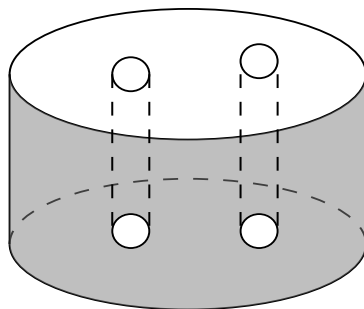
Figure 4.2: Diagram of an Mg block with two pore channels with circular cross section. The modelling focuses on reactions within a single pore.

reaction

$$Mg(OH)_2 + CO_2 \longrightarrow MgCO_3 + H_2O, \tag{4.2}$$
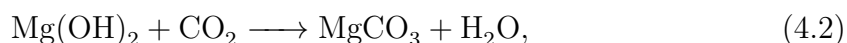
forming a stable layer of $MgCO_3$.

A cylindrical pore size within a Mg block is modelled in this chapter, as shown in Figure 4.2. The model describes the physiological interactions inside a single pore and perceives events from the start of the corrosion process of Mg within a pore, through the formation of the hydroxide and carbonate layers inside the pore, until the pore closes up. It is assumed that the Mg region surrounding the pore is infinite, so the metal cannot be exhausted during the corrosion process. It is further assumed that the outer layer of Mg around the pore has no other voids and corrodes in a way that maintains a smooth surface. Consequently, it is envisaged that inside the pore, a $Mg(OH)_2$ layer is produced on the Mg surface, and then the $MgCO_3$ layer is produced on the $Mg(OH)_2$ surface; see Figure 4.3 for the expected corrosion layers inside the pore. In order for the Mg to corrode further, water in the pore must be able to diffuse through the carbonate and hydroxide layers to react at the Mg surface, and CO_2 in the pore must be able to diffuse through the carbonate layer to reach the hydroxide compound interface. Like the model in Chapter 3, these assumptions result in a model that describes the transport and reaction processes of water and CO_2 as well as the location of the interfaces between Mg and its constituents, which are deposited
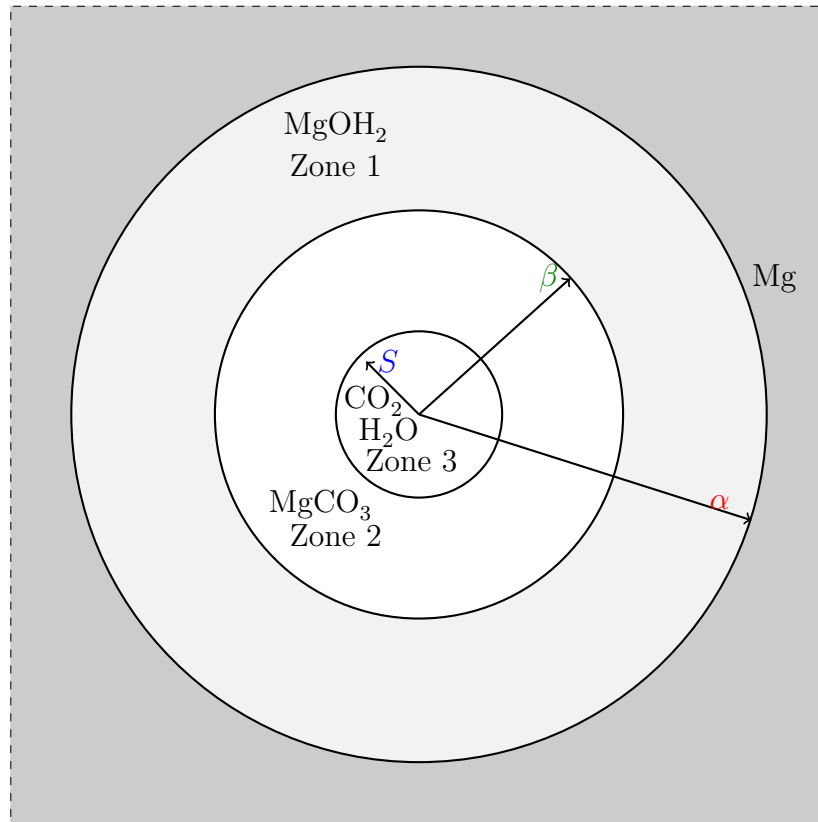
Figure 4.3: Set-up of the physiochemical decomposition inside a single magnesium pore used in the model for cylindrical geometry. The pure magnesium exists on the outer layer (Zone 0, $\alpha(t) < r$), the magnesium hydroxide forms a layer inside the magnesium pore (Zone 1, $\beta(t) < r < \alpha(t)$), which is followed by a further layer of magnesium carbonate inside the pore (Zone 2, $S(t) < r < \beta(t)$); and the pore, acting as a water and CO_2 source, exists in the centre (Zone 3, $0 \leq r < S(t)$).

on the Mg surface inside the pore as corrosion products. As in the previous model, in Chapter 3, the hydroxide and carbonate layers are treated as porous media, thereby the movement speed of the "solid" components, i.e. the $Mg(OH)_2$ and $MgCO_3$, is distinct to that of the fluid and gas components, i.e., water and CO_2. By assuming a radically symmetric cylindrical geometry, a closed system of equations is found based on mass conservation alone.

4.2.1 Model Variables

The model variables here are similar to those in Chapter 3. A radically symmetric cylindrical geometry is applied where changes occur only in the r direction, writing r as the spatial co-ordinate and t as the time variable, the moving boundaries between the layers are represented as follows

- $r = \alpha(t)$: the location of the magnesium to magnesium hydroxide interface.

- $r = \beta(t)$: the location of the magnesium hydroxide to magnesium carbonate interface.

- $r = S(t)$: the location of the pore interface.

The spaces between the interfaces are denoted by

- Zone 0: the Mg layer $\alpha(t) < r$.

- Zone 1: the $Mg(OH)_2$ layer $\beta(t) < r < \alpha(t)$.

- Zone 2: the $MgCO_3$ layer $S(t) < r < \beta(t)$.

- Zone 3: the pore $0 \leq r < S(t)$.

The mass concentrations of water and carbon dioxide in the Mg compound pores are denoted by

- $W_1(r, t)$: the concentration of water in the $Mg(OH)_2$ layer.

- $W_2(r, t)$: the concentration of water in the $MgCO_3$ layer.

- $C_2(r, t)$: the concentration of carbon dioxide in the $MgCO_3$ layer.

As the hydroxide deposits on the magnesium surface and likewise the carbonate on the hydroxide surface, the "solid" compounds move with velocities v_{s_i}; and the

movement of water and carbon dioxide in the fluid phases are denoted by velocities v_{f_i}, where $i = 1, 2$ corresponding to the zone.

The solid structures of Zones 1 and 2 are assumed to consist of a fixed volume fraction of the Mg compound and non-traversable space (ε_i) and traversable space $(1 - \varepsilon_i)$, where traversable space is interpreted as continuous channels of space and excludes fully enclosed gaps in the solid structure. The outer layer of Mg that is observed in the model is assumed to be completely non-traversable, thus $\varepsilon_0 = 1$.

The chemical reactions are assumed to take place only at the interfaces $\alpha(t)$ and $\beta(t)$, whereby the rate at which these boundaries move depends on the local rate of reaction. Inside the pore, the water and CO_2 concentration are assumed to be inexhaustible *in vitro* or in the physiological environment, so the magnesium and the hydroxide will continue being consumed until the pore is completely blocked, i.e. $S = 0$. Therefore, the model is only expected to be valid for a finite time, $0 < t < T_S$, whereby $t = T_S$ is the point in time when $S(t) = 0$ (i.e. $S(t) > 0$ for $t < T_S$). After $S(t) = 0$, the pore no longer exists and there are no further developments in the system; so the end result is the carbonate surrounded by a layer of the hydroxide enclosed within an outer layer of magnesium.

We note, for $t > T_S$, the water and CO_2 that are present in the hydroxide and carbonate layers at $t = T_S$ will continue to react until exhaustion. However, there are no stress free boundaries to allow for volume expansion from these reactions, meaning that stresses will build up in the pore; this is not considered in the current model as we limit attention to a $t < T_S$ time frame.

Table 4.1 summarizes the above and lists the parameters corresponding to each zone.

Zone (i)	Domain	Solid fraction	Solid constituent	Mass density	Molecular mass	Mol/Vol	Solid velocity
0	$\alpha < r$	$\varepsilon_0 = 1$	Mg	ρ_0	M_0	μ_0	0
1	$\beta < r < \alpha$	ε_1	$Mg(OH)_2$	ρ_1	M_1	μ_1	v_{s_1}
2	$S < r < \beta$	ε_2	$MgCO_3$	ρ_2	M_2	μ_2	v_{s_2}

Table 4.1: Notation used in the model where $\rho_i = M_i \mu_i$, $\omega_\alpha = \mu_0/\mu_1$ and $\omega_\beta = \mu_1/\mu_2$.

4.3 Mathematical Model

The derivation of the model is the same as that in the previous chapter in Section 3.2, except the set-up of the model is "inside out". The radial velocities of the magnesium compound phases are $v_{s_1}(r,t)$ and $v_{s_2}(r,t)$, hence the conservation of mass for cylindrical geometry implies

$$\frac{1}{r}\frac{\partial}{\partial r}\left(r\varepsilon_1 v_{s_1}\right) = 0 \qquad r \in (\beta, \alpha), \tag{4.3}$$

$$\frac{1}{r}\frac{\partial}{\partial r}\left(r\varepsilon_2 v_{s_2}\right) = 0 \qquad r \in (S, \beta), \tag{4.4}$$

where ε_1 and ε_2 are the constant solid fractions for Zone 1 and Zone 2, respectively. These can be divided out, but the fraction term will be retained in the model derivation for completeness. The fluid phase is assumed to consist of all non-solid materials and that it is non-compressible. Hence,

$$\frac{1}{r^d}\frac{\partial}{\partial r}\left(r^d(1-\varepsilon_1) v_{f_1}\right) = 0 \qquad r \in (\beta, \alpha), \tag{4.5}$$

$$\frac{1}{r^d}\frac{\partial}{\partial r}\left(r^d(1-\varepsilon_2) v_{f_2}\right) = 0 \qquad r \in (S, \beta). \tag{4.6}$$

where the fluid fractions, $(1-\varepsilon_1)$ and $(1-\varepsilon_2)$ are constants, and v_{f_1} and v_{f_2} are the fluid velocities of Zone 1 and Zone 2, respectively. It is noted that the flow here does not encompass that of the fluid/gas trapped in non-traversable pores in the solid

structure. The advection-diffusion fluxes for water and carbon dioxide are as follows

$$
\begin{aligned}
J_{W_1} &= v_{f_1} W_1 - D_W \nabla W_1 & r &\in (\beta, \alpha), \\
\left. \begin{aligned}
J_{W_2} &= v_{f_1} W_2 - D_W \nabla W_2 \\
J_{C_2} &= v_{f_1} C_2 - D_C \nabla C_2
\end{aligned} \right\} & r &\in (S, \beta),
\end{aligned}
\tag{4.7}
$$

where D_W is the diffusion coefficient of water and D_C is the diffusion coefficient of carbon dioxide. These yield the following transport equations

$$
\frac{\partial((1 - \varepsilon_1)W_1)}{\partial t} = -\frac{1}{r}\frac{\partial}{\partial r}(r(1 - \varepsilon_1)J_{W_1}) \qquad r \in (\beta, \alpha), \tag{4.8}
$$

$$
\left. \begin{aligned}
\frac{\partial((1 - \varepsilon_2)W_2)}{\partial t} &= -\frac{1}{r}\frac{\partial}{\partial r}(r(1 - \varepsilon_1)J_{W_2}) \\
\frac{\partial((1 - \varepsilon_2)C_2)}{\partial t} &= -\frac{1}{r}\frac{\partial}{\partial r}(r(1 - \varepsilon_1)J_{C_2})
\end{aligned} \right\} \qquad r \in (S, \beta). \tag{4.9}
$$

4.3.1 Initial, Boundary and Interface Conditions

Initially, it is assumed that there is a pore with an outer layer of magnesium, therefore

$$
t = 0: \qquad S(0) = \beta(0) = \alpha(0) = P_0, \tag{4.10}
$$

where $P_0 > 0$ is the initial radius of the pore. Water and carbon dioxide is sourced from inside the pore on $r = S$, which flow at speed equal to the local velocity, hence

$$
r = S(t): \qquad W_2 = W_0^*, \quad C_2 = C_0^*, \quad \dot{S} = v_{s_2}, \tag{4.11}
$$

where $\dot{S} = dS/dt$, and W_0^* and C_0^* are constant concentrations of water and carbon dioxide *in vitro* or in physiological environments that are inside the pore.

As seen in Chapter 3, the conditions on the interfaces are more complex and change at critical points of the corrosion process. Water, from inside the pore, reacts
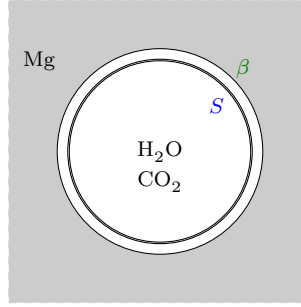
Figure 4.4: Physiochemical schematic at the start of the corrosion process when $k < \infty$ and $S(t) - \beta(t)$ is very small (at $0 < t \leq T_{\alpha=\beta}$), where the CO_2 inside the pore can penetrate the tiny layer of $MgCO_3$ and instantly react the $Mg(OH)_2$ without exhausting the CO_2, hence the hydroxide layer is absent i.e. $\alpha(t) = \beta(t)$.

with the surface of the magnesium sample at $r = \alpha(t)$. The rate of this reaction, R_α, will be dependent on the water concentration and flux there. As two water molecules are consumed, it is assumed by the law of mass action applied to (3.1) that $R_\alpha = kW_1^2$, where k is a rate constant. The same two cases considered in Chapter 3 will be examined in this model, these are as follows

- *Case 1* considers the limit $k \to \infty$, where the reaction is so rapid that water is immediately exhausted on the $r = \alpha(t)$ interface, hence $W_1 = 0$.

- *Case 2* considers $k < \infty$, whereby $W_1 > 0$ on $r = \alpha(t)$. In small time, when $1 - \beta(t)/S(t) \ll 1$, the small distance for the carbon dioxide to diffuse means that $Mg(OH)_2$ immediately becomes exhausted on production and Mg converts to $MgCO_3$, in effect, immediately; consequently $\alpha(t) = \beta(t)$ during this transient. See Figure 4.4 for a visualisation of this. In time, the thickness of Zone 2, $S(t) - \beta(t)$, becomes sufficiently large for the reaction to exhaust the carbon dioxide on $r = \beta(t)$, allowing the $Mg(OH)_2$ layer to grow.

All the conditions on $r = \alpha(t)$ and $r = \beta(t)$ are the same as that in Section 3.2.1 in Chapter 3, except for the interface condition on $r = \alpha(t)$ when $k < \infty$, where the

water flux is

$$(1 - \varepsilon_1)(-W_1\dot{\alpha} + J_{W_1}) = 2R_\alpha = 2kW_1^2;$$

note the sign change here, because growth is in a different direction relative to the outward normal. For *Case 1*, the conditions are on

$$
\begin{aligned}
r = \alpha(t): \quad & v_{s_1} = -(\omega_\alpha - 1)\dot{\alpha}, \ v_{f_1} = \dot{\alpha}, \\
& (1 - \varepsilon_1)(-\dot{\alpha}W_1 + J_{W_1}) = 2\frac{M_W}{M_0}\rho_0\dot{\alpha}, \\
& W_1 = 0 \text{ for } k \to \infty \quad \text{or} \quad \frac{M_W}{M_0}\rho_0\dot{\alpha} = kW_1^2 \text{ for } k < \infty,
\end{aligned}
\tag{4.12}
$$

and

$$
\begin{aligned}
r = \beta(t): \quad & C_2 = 0, \ W_2 = W_1, \ v_{s_2} = v_{s_1} - (\omega_\beta - 1)(\dot{\beta} - v_{s_1}), \\
& (1 - \varepsilon_1)(v_{f_1} - \dot{\beta}) = (1 - \varepsilon_2)(v_{f_2} - \dot{\beta}), \\
& (1 - \varepsilon_2)(-\dot{\beta}W_2 + J_{W_2}) - (1 - \varepsilon_1)(-\dot{\beta}W_1 + J_{W_1}) = -\frac{M_W}{M_1}\rho_1(\dot{\beta} - v_{s_1}), \\
& (1 - \varepsilon_2)(-\dot{\beta}C_2 + J_{C_2}) = \frac{M_C}{M_1}\rho_1(\dot{\beta} - v_{s_1}),
\end{aligned}
\tag{4.13}
$$

for $S(t) > 0$. For *Case 2*, when $t \leq T_{\alpha=\beta}$, then the hydroxide layer is absent. Hence, the boundary conditions are

$$
\begin{aligned}
r = \alpha(t) = \beta(t): \quad & v_{s_2} = -(\omega_\alpha\omega_\beta - 1)\dot{\beta}, \ v_{f_2} = \dot{\beta}, \\
& (1 - \varepsilon_2)(-\dot{\beta}W_2 + J_{W_2}) = \frac{M_W}{M_1}\rho_1\dot{\beta}, \\
& \frac{M_W}{M_0}\rho_0\dot{\beta} = kW_1^2, \quad (1 - \varepsilon_2)J_{C_2} = \frac{M_C}{M_1}\rho_1\dot{\beta};
\end{aligned}
\tag{4.14}
$$

and once $t > T_{\alpha=\beta}$ conditions (4.12) and (4.13) are imposed. See Section 3.2.1 for a derivation of the conditions.

The derived system describes the alteration of Mg to $MgCO_3$ inside the pore. It assumes that $MgCO_3$ will have no exit from the system, and the final stage is when the pore is blocked, which is at $t = T_S$ when $S(t) = 0$. The different stages modelled

Phase		time	b.c.s	v_{s_i} and v_{f_i}
1.1	$k \to \infty$	$0 \leq t \leq T_S$	(4.12), (4.13)	(4.15)
2.1	$k < \infty$	$0 \leq t \leq T_{\alpha = \beta}$	(4.14)	(4.16)
2.2		$T_{\alpha = \beta} < t \leq T_S$	(4.12), (4.13)	(4.15)

Table 4.2: Relevant boundary conditions for each of the Mg corrosion phases for the two cases $k \to \infty$ and $k < \infty$, where time scales $T_{\alpha=\beta}$ and T_S represent the smallest points in time when Phase 2.1 ends and $S = 0$, respectively.

during the corrosion of Mg from inside the pore are labelled for the two cases on k. These are, Phase 1.1 (for $k \to \infty$ and $0 \leq t \leq T_S$), Phase 2.1 (for $k < \infty$ and $0 \leq t \leq T_{\alpha=\beta}$) and Phase 2.2 (for $k < \infty$ and $T_{\alpha=\beta} < t \leq T_S$).

Table 4.2 summarises the boundary conditions used for the different phases in *Case 1* and *Case 2*.

4.3.2 Exact Solutions

Equations (4.3)-(4.6) are integrated for each of the scenarios in Table 4.2. For *Case 1*, applying equations (4.12) and (4.13) gives

$$v_{s_1} = -\frac{(\omega_\alpha - 1)\,\dot{\alpha}\,\alpha}{r}, \qquad v_{s_2} = -\frac{\omega_\beta\,(\omega_\alpha - 1)\,\dot{\alpha}\,\alpha + (\omega_\beta - 1)\,\dot{\beta}\,\beta}{r},$$
$$v_{f_1} = \frac{\dot{\alpha}\,\alpha}{r}, \qquad v_{f_2} = \frac{(1 - \varepsilon_1)\,\dot{\alpha}\,\alpha - (\varepsilon_2 - \varepsilon_1)\,\dot{\beta}\,\beta}{(1 - \varepsilon_2)r}, \tag{4.15}$$

for $t \leq T_S$. For *Case 2*, applying (4.14) gives

$$v_{s_1} = -\frac{(\omega_\alpha - 1)\,\dot{\beta}\,\beta}{r}, \qquad v_{s_2} = -\frac{(\omega_\alpha\,\omega_\beta - 1)\dot{\beta}\beta}{r},$$
$$v_{f_1} = \frac{\dot{\beta}\,\beta}{r}, \qquad v_{f_2} = \frac{\dot{\beta}\,\beta}{r}, \tag{4.16}$$

for $t \leq T_{\alpha=\beta}$, and the velocities for $T_{\alpha=\beta} < t \leq T_S$ are the same as that in equation (4.15). Using the formulation in (4.15) for v_{s_2}, we obtain

$$S\dot{S} = -\omega_\beta(\omega_\alpha - 1)\alpha\dot{\alpha} + (\omega_\beta - 1)\beta\dot{\beta},$$

which on integration, using (4.10), yields

$$S = P_0 \big[-(\omega_\beta - 1)\,(\beta/P_0)^2 - \omega_\beta(\omega_\alpha - 1)\,(\alpha/P_0)^2 + \omega_\alpha\,\omega_\beta \big]^{1/2}, \tag{4.17}$$

which is valid for Phase 1.1 and Phase 2.2, and substituting $\alpha = \beta$ into (4.17) gives S for Phase 2.1. In the final stage of the corrosion process, the following is obtained on substitution of $S = 0$, for $\omega_\alpha \neq 1$,

$$(\omega_\beta - 1)\beta_\infty^2 + \omega_\beta(\omega_\alpha - 1)\alpha_\infty^2 = \omega_\alpha\omega_\beta P_0^2, \tag{4.18}$$

where α_∞ and β_∞ are the final sizes of α and β at pore closure. It must be emphasised that ω_α and/or ω_β, which represent the molar densities of the two reactions, must be more than 1 for $S \to 0$, otherwise equation (4.18) can never be satisfied. In other words, one of both of the chemical reactions need to create solid phase volume to enable the pore to close. Note that the corroded thickness of Mg is $\alpha_\infty - P_0$ and equation (4.18) indicates that $\alpha_\infty \propto P_0 \Leftrightarrow \beta_\infty \propto P_0$.

An upper bound for α_∞ can be identified by assuming that there is no carbonate layer and so the pore is filled with the hydroxide at closure. For this, using the formulation in (4.15) for v_{s_1}, we have

$$\beta\dot{\beta} = -(\omega_\alpha - 1)\alpha\dot{\alpha},$$

which on integration, using (4.10), gives

$$\beta_\infty^2 = -(\omega_\alpha - 1)\alpha_\infty^2 + P_0^2\omega_\alpha, \tag{4.19}$$

at T_S. Substituting (4.19) into (4.18) yields the following upper bound

$$\alpha_\infty = \sqrt{\frac{\omega_\alpha}{\omega_\alpha - 1}} P_0. \tag{4.20}$$

There are no further exact solutions to be obtained and variables α, β, W_1, W_2 and C_2 need to be resolved numerically from (4.8), (4.9) and (4.10)-(4.14).

The data for the model parameters is represented in Table 3.3 (in the previous chapter Section 3.2.2). There are three parameters $\varepsilon_1, \varepsilon_2$ and k for which information appears to be limited; they will be investigated further on their effects to the degradation behaviour of magnesium from inside a pore. The parameter for the initial size of the pore, P_0, will also be explored.

4.3.3   Non-dimensionalisation

The variables are rescaled in a similar way to that in Section 3.2.3. A suitable timescale is chosen for which carbon dioxide diffuses across a reference distance P_0^* (choosing $P_0^* = 250\,\mu\mathrm{m}$). The water and carbon dioxide variables are rescaled with ambient mass concentrations W_0^* and C_0^*, therefore

$$t = \frac{P_0^{*2}}{D_c}\hat{t}, \quad r = P_0^*\hat{r}, \quad W_1 = W_0^*\hat{W}_1, \quad W_2 = W_0^*\hat{W}_2, \quad C_2 = C_0^*\hat{C}_2, \quad \alpha = P_0^*\hat{\alpha},$$

$$\beta = P_0^*\hat{\beta}, \quad S = P_0^*\hat{S},$$

and $v_* = D_C\hat{v}_*/P_0^*$, where the quantities with hats are dimensionless. Using the data in Table 3.3 the scaling implies that $\hat{t} = 1$ represents about 0.54 minutes. Let

$$\hat{P}_0 = \frac{P_0}{P_0^*}, \quad \hat{D}_W = \frac{D_W}{D_C}, \quad \gamma_0 = \frac{M_W\rho_0}{M_0W_0^*}, \quad \gamma_1 = \frac{M_W\rho_1}{M_1W_0^*}, \quad \gamma_2 = \frac{M_C\rho_1}{M_1C_0^*}, \quad \kappa = \frac{P_0^*W_0^*}{D_C}k,$$

$$\tag{4.21}$$

noting that ω_α and ω_β are already dimensionless, then, on dropping the hats for clarity, the following system is obtained

$$\frac{\partial W_1}{\partial t} + v_{f_1} \frac{\partial W_1}{\partial r} - \frac{D_W}{r} \frac{\partial}{\partial r} \left(r \frac{\partial W_1}{\partial r} \right) = 0, \qquad (4.22)$$

$$\frac{\partial W_2}{\partial t} + v_{f_2} \frac{\partial W_2}{\partial r} - \frac{D_W}{r} \frac{\partial}{\partial r} \left(r \frac{\partial W_2}{\partial r} \right) = 0, \qquad (4.23)$$

$$\frac{\partial C_2}{\partial t} + v_{f_2} \frac{\partial C_2}{\partial r} - \frac{1}{r} \frac{\partial}{\partial r} \left(r \frac{\partial C_2}{\partial r} \right) = 0, \qquad (4.24)$$

with velocities for each scenario, after non-dimensionalisation, the same as that shown in equations (4.15) and (4.16). Initial conditions are

$$\alpha(0) = \beta(0) = S(0) = P_0. \qquad (4.25)$$

For *Case 1*, $\kappa \to \infty$, the boundary conditions are as follows,

$$W_1(\alpha, t) = 0, \quad W_1(\beta, t) = W_2(\beta, t), \quad W_2(S, t) = 1, \quad C_2(\beta, t) = 0, \quad C_2(S, t) = 1, \qquad (4.26)$$

with interface conditions

$$\begin{aligned}
r = \alpha(t) : \quad & -(1 - \varepsilon_1) D_W \partial_r W_1 = 2 \gamma_0 \dot{\alpha}, \\
r = \beta(t) : \quad & D_W \left((1 - \varepsilon_1) \partial_r W_1 - (1 - \varepsilon_2) \partial_r W_2 \right) = -\gamma_1 \left(\dot{\beta} + \frac{(\omega_\alpha - 1) \alpha^d \dot{\alpha}}{\beta^d} \right), \\
& -(1 - \varepsilon_2) \partial_r C_2 = \gamma_2 \left(\dot{\beta} + \frac{(\omega_\alpha - 1) \alpha^d \dot{\alpha}}{\beta^d} \right),
\end{aligned} \qquad (4.27)$$

and analytical solution for S

$$S = P_0 \left(\omega_\alpha \omega_\beta - (\omega_\beta - 1)(\beta/P_0)^2 - \omega_\beta(\omega_\alpha - 1)(\alpha/P_0)^2 \right)^{1/2}. \qquad (4.28)$$

For *Case 2*, $\kappa < \infty$, the boundary conditions are as follows

$$W_2(S,t) = 1, \quad C_2(S,t) = 1, \tag{4.29}$$

and for $t \leq T_{\alpha=\beta}$ interface conditions are

$$r = \alpha(t) = \beta(t) : \quad \gamma_0\dot{\beta} = \kappa W_2^2, \quad -D_W(1-\varepsilon_2)\,\partial_r W_2 = \gamma_1\,\omega_\alpha\,\dot{\beta},$$
$$-(1-\varepsilon_2)\partial_r C_2 = \gamma_2\,\omega_\alpha\,\dot{\beta}, \tag{4.30}$$

and analytical solution

$$S = P_0\left[(\beta/P_0)^2 + \omega_\alpha\omega_\beta(1-(\beta/P_0)^2)\right]^{1/2}. \tag{4.31}$$

For $T_{\alpha=\beta} < t \leq T_S$, in addition to equations (4.29), we have

$$\gamma_0\dot{\alpha} = \kappa W_1^2, \quad W_1(\beta,t) = W_2(\beta,t), \quad C_2(\beta,t) = 0, \tag{4.32}$$

and interface conditions (4.27) and (4.28) are imposed.

Table 3.4 in Section 3.2.3 displays the values of the dimensionless parameters used in the model simulations.

4.4   Numerical Method and Asymptotics

The system of PDEs in (4.22)-(4.24) is solved numerically using the same method as in Chapter 3. Firstly, the spatial domains are mapped onto the unit interval $\rho \in [1,2]$ using the rescaling presented in Section 3.3.1, where $(r,t) \to (\rho,\tau)$. The singularities resulting from $\alpha = \beta = S$ at $t = 0$ at the start of Phase 1.1 and Phase 2.1 and $\alpha = \beta$ at $t = T_{\alpha=\beta}$ at the start of Phase 2.2 are dealt with in a similar way to that in Section 3.3.2. For *Case 1*, the simulation starts at $\tau = \tau_0 \ll 1$ so that a tiny

amount of corrosion has occurred and, due to $\omega_\alpha, \omega_\beta > 1$, $S(\tau_0) < P_0 < \alpha(\tau_0)$ with $1 - S(\tau_0)/P_0 \ll 1$ and $\alpha(\tau_0)/P_0 - 1 \ll 1$. The united radii $\alpha(\tau_0)$, $\beta(\tau_0)$ and $S(\tau_0)$ are approximated using small time asymptotic expansions

$$\alpha(\tau) \sim P_0 + a_1\, \tau^{1/2}, \quad \beta(\tau) \sim P_0 + b_1\, \tau^{1/2}, \quad S(\tau) \sim P_0 + s_1\, \tau^{1/2} \tag{4.33}$$

for $\tau \ll 1$, where $a_1 > 0$ and $s_1 < 0$ are expected. The expansions lead to equations (3.52) and (3.54) as $\tau \longrightarrow 0$, which are solved to provide initial conditions for $\alpha, \beta, S, W_1, W_2$ and C_2 at small time. A similar approach is used in *Case 2*, whereby $S(\tau_0) < P_0 < \beta(\tau_0) = \alpha(\tau_0)$. The following small time asymptotic approximations are applied to the equations for Phase 2.1

$$\begin{aligned}
\beta &\sim P_0 + b_1^{[1]}\tau + b_2^{[1]}\tau^2, \\
S &\sim P_0 + s_1^{[1]}\tau + s_2^{[1]}\tau^2, \\
W_2 &\sim 1 + W_{2_1}^{[1]}(\rho)\tau + W_{2_2}^{[1]}(\rho)\tau^2, \\
C_2 &\sim 1 + C_{2_1}^{[1]}(\rho)\tau + C_{2_2}^{[1]}(\rho)\tau^2,
\end{aligned} \tag{4.34}$$

where it was found that

$$\begin{aligned}
b_1^{[1]} &= \frac{\kappa}{\gamma_0}, \quad b_2^{[1]} = \frac{\kappa}{\gamma_0}\, W_{2_1}^{[1]}, \quad s_1^{[1]} = (1 - w_\alpha w_\beta)\, b_1, \\
s_2^{[1]} &= \frac{1}{P_0}(1 - w_\alpha w_\beta)\left(\frac{b_1^{[1]^2}\, w_\alpha w_\beta}{2} + P_0 b_2^{[1]}\right);
\end{aligned} \tag{4.35}$$

and the initial conditions of W_2 and C_2 in equation (3.57) are relevant.

After changing the variables and imposing the small time asymptotic analysis, the system of PDEs and the appropriate boundary conditions for each of the phases was solved using an adjustment of the code in the previous chapter, where the Method of Lines (MoL) was implemented in MATLAB. The stiff ODE solver, *ode15s*, was

applied for the time stepping process.

4.5   Results

In this section, the results from the numerical solution are discussed. As mentioned in Chapter 3, there are three parameters in the model listed in Table 3.3 for which data is not identified, $\varepsilon_1, \varepsilon_2$ and κ, (though $\varepsilon_1 = 0.6$ and $\varepsilon_2 = 0.4$ was chosen for most simulations to keep the values close to the mid-range). The degradation of magnesium is examined in the simulations, and in particular the pore closure time, T_S, and the final sizes, α_∞ and β_∞. Section 4.5.2 explores the effect of the initial size of the pore, which can be experimentally controlled through fabrication techniques, but for the rest of the simulations the pore radius is set at the reference value, $250\,\mu m$ (i.e. $P_0 = 1$).

4.5.1   Magnesium Degradation

For *Case 1*, $\kappa \to \infty$, the result for when $\varepsilon_1 = 0.6$ and $\varepsilon_2 = 0.4$ is shown in Figure 4.5, where the size of Mg and its compounds are displayed over time. The dashed lines in Figure 4.5 represent T_S. Evidently, it is seen that Mg corrodes until the pore is blocked, after this it remains at a constant size. Since the reaction rate is infinite in this case, the $Mg(OH)_2$ is being produced quicker than it is being consumed and so $\beta - S$ is very small throughout. After reaching T_S the hydroxide remains at a constant size. The size of the pore becomes smaller throughout the corrosion process as the centre of the pore is suffused with $MgCO_3$ and $Mg(OH)_2$. The pore closes quite rapidly at $t = O(1)$, which is due to $\kappa \to \infty$.

Figure 4.6 shows an example simulation for a finite reaction rate (*Case 2*) when $\kappa = 1.05 \times 10^{-3}$ (corresponding to $k = 0.07 cm^4/g \cdot s$ in Table 3.3) for Mg and its compounds over time. Here, the dashed lines represent $T_{\alpha=\beta}$ (left) and T_S (right). After $T_{\alpha=\beta}$, when β and α begin to separate, the hydroxide is produced but appears
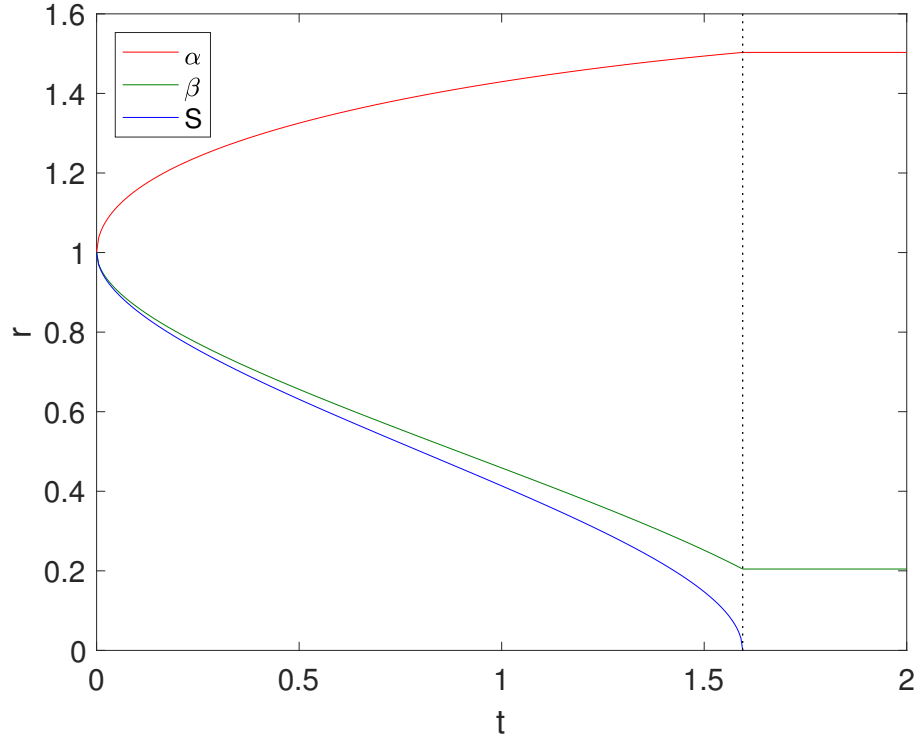
Figure 4.5: Plots of α, β and S against t using $\varepsilon_1 = 0.6$, $\varepsilon_2 = 0.4$, $\kappa \to \infty$, the parameters in Table 3.4 and $P_0 = 1$. The dashed line shows $t = T_S$.

to be consumed quickly by its reaction with CO_2. In contrast to Figure 4.5, the pore takes much longer to close at $t = O(10^2)$, because, here, the reaction rate is finitely small.

The water and CO_2 concentration distribution is displayed in Figure 4.7 at the start of Phase 2.1, end of Phase 2.1 $(t = T_{\alpha=\beta})$, Phase 2.2 at the point the full system is solved numerically and end of Phase 2.2 $(t = T_S)$; the times t are detailed in the caption where $\kappa \approx 1.05 \times 10^{-3}$, $\varepsilon_1 = 0.6$ and $\varepsilon_2 = 0.4$. In small time, the $Mg(OH)_2$ layer is absent so a tiny layer of $MgCO_3$ surrounds the Mg inside the pore, and, evidently, the concentrations of water and CO_2 are quite uniform $r \in (S, \beta)$. Moreover, the CO_2 is not exhausted at β in small time, but in time, the concentration declines to zero at the end of Phase 2.1. As time progresses into Phase 2.2, $\alpha - \beta$ and $\beta - S$ are still small and the profiles for water and CO_2 are approximately linear.
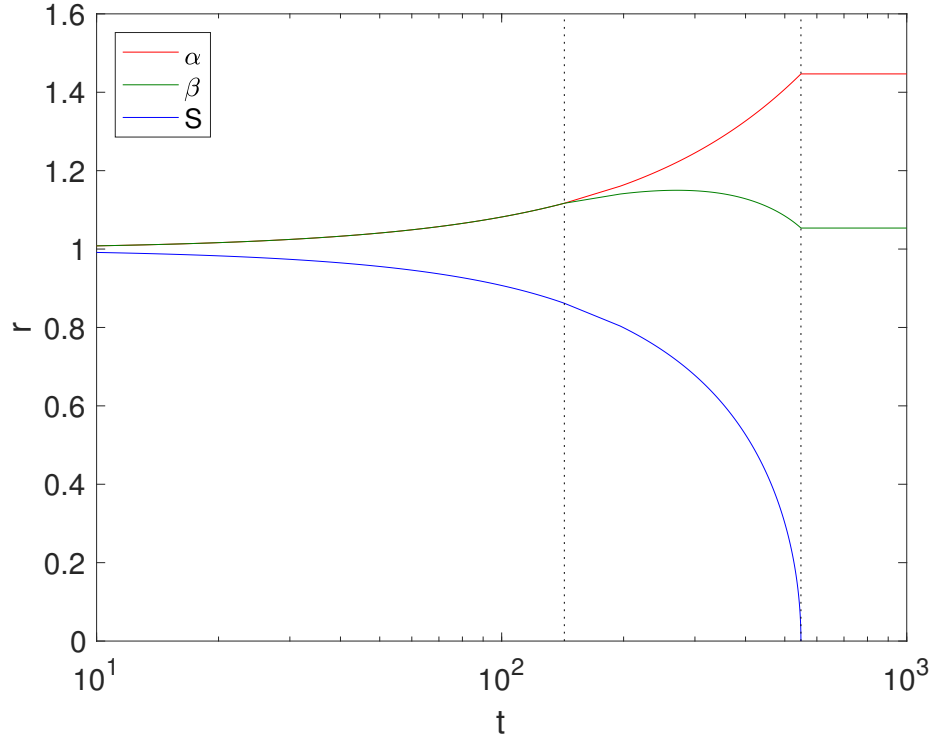
Figure 4.6: Plots of α, β and S against t using $\varepsilon_1 = 0.6$, $\varepsilon_2 = 0.4$, $\kappa = 1.05 \times 10^{-3}$, the parameters in Table 3.4 and $P_0 = 1$. The dashed lines show $t = T_{\alpha=\beta}$ (left) and T_S (right).

A slight upward kink in the water distribution is noted at $r = \beta$ on close inspection, which is due to the production of water when the hydroxide converts to the carbonate. By the end of Phase 2.2, the water and CO_2 distributions are non-linear.

4.5.2 Effect of Pore Size

The non-dimensionalisation in Section 3.2.3 is such that the initial radius of the pore is $P_0 = 1$, which has been used in the simulations up until now and corresponds to $250\,\mu m$. Explored in Figure 4.8 is the relationship between the initial pore radius, which ranges from $0.01 - 40$ (corresponding to $2.5\,\mu m$ - 1 cm), and the final sizes of α and β (right); and the relationship between the initial pore radius and T_S (left). Other parameters in the simulation are $\kappa \approx 0.03, \varepsilon_1 = 0.6$ and $\varepsilon_2 = 0.4$. Evidently,
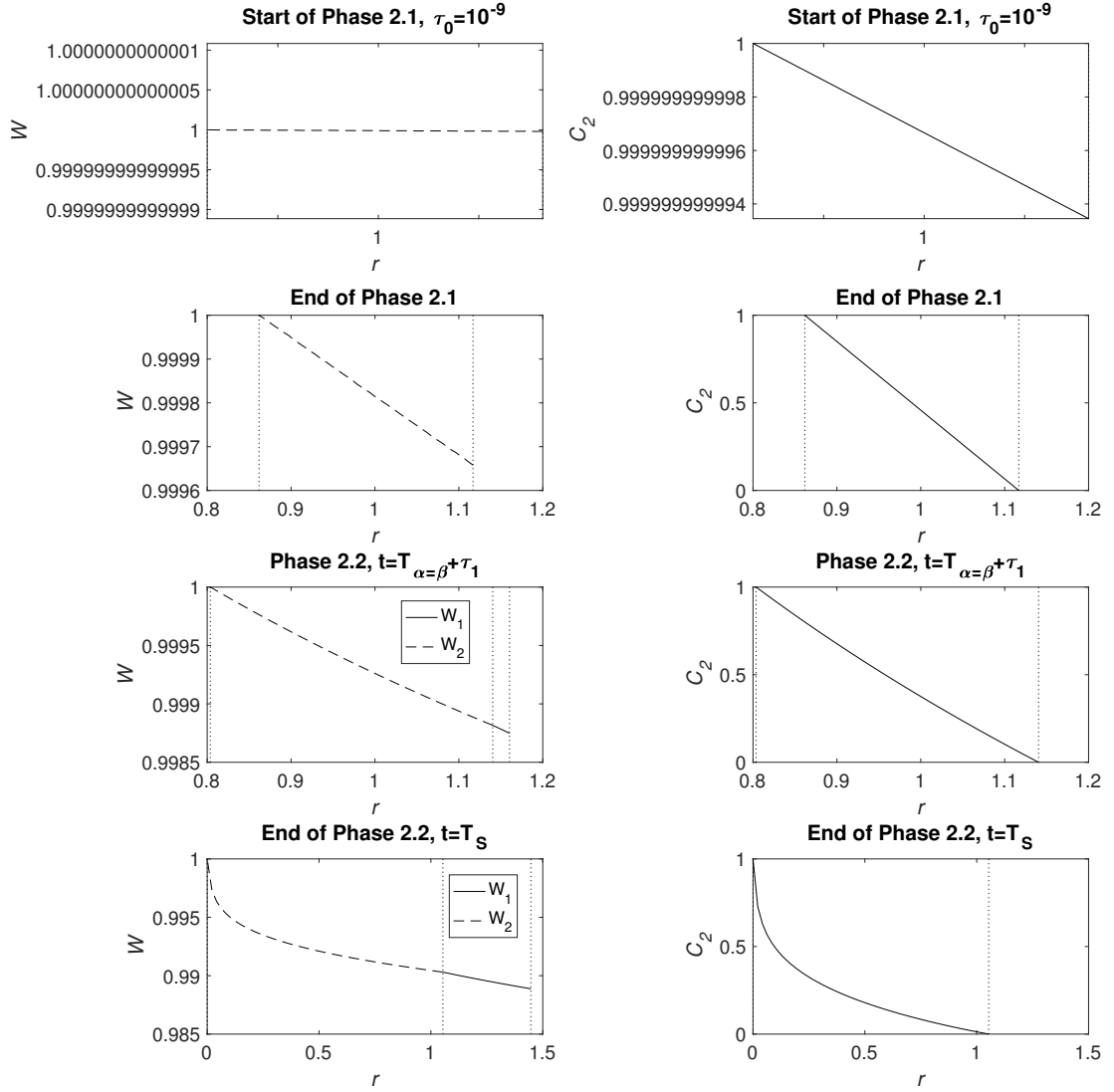
Figure 4.7: Plots of the concentrations W_1, W_2 (left) and C_2 (right) at, from top to bottom, the start of Phases 2.1 ($t = \tau_0 = 10^{-9}$), end of Phase 2.1 ($t = T_{\alpha=\beta} \approx 142.79$), Phase 2.2 ($t = T_{\alpha=\beta} + \tau_1$, with $\tau_1 = 53.3$, see Section 3.3.2), and the end of 2.2 ($t = T_S \approx 548.1$). In the left-hand panel, the solid lines represent W_1 and the dashed lines W_2. The vertical dotted lines indicate from right to left, $r = \beta$, $r = S$ (right-hand panel and top 2 plots on left-hand panel) and $r = \alpha$, $r = \beta$, $r = S$ (bottom 3 plots on left-hand panel). The parameters are $\varepsilon_1 = 0.6$, $\varepsilon_2 = 0.4$, $\kappa \approx 1.05 \times 10^{-3}$, $P_0 = 1$ and the rest listed in Table 3.4.
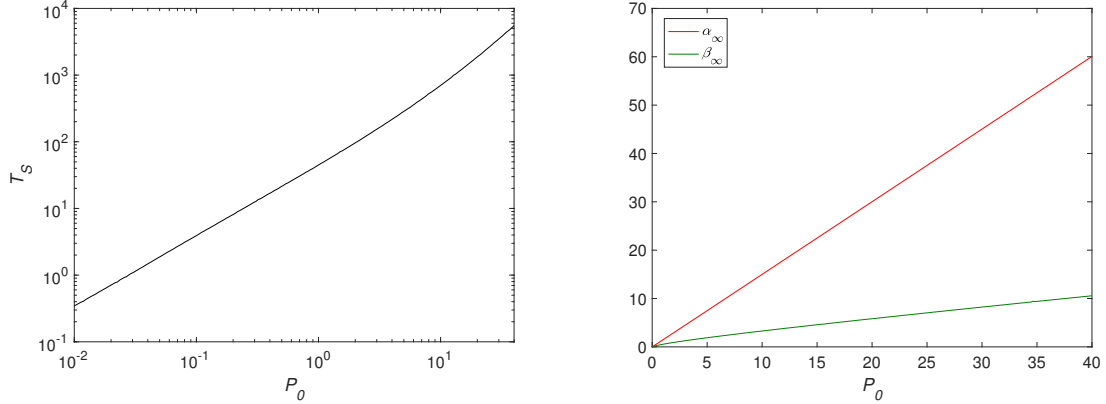
Figure 4.8: Plot of T_S against P_0 (top), and α_∞ and β_∞ against P_0 (bottom) when $\kappa \approx 0.015$, $\varepsilon_1 = 0.6$, $\varepsilon_2 = 0.4$. The remaining parameters are listed in Table 3.4.

as the initial pore size is increased then the pore takes longer to close up and more Mg has corroded at T_S. It is noted that the left plot does not give a power law relationship, but for the right of Figure 4.8 a linear relationship is detected for α_∞ and β_∞; from the analytical solution in equation (4.18), this can be expected.

4.5.3 Effect of Porosity of the $Mg(OH)_2$ and $MgCO_3$ Layers

In Figure 4.9, α_∞ and β_∞ are plotted against changes in ε_1 and ε_2 for $\kappa = 0.03, 3$, $\varepsilon_1 = 0.6$ (bottom) and $\varepsilon_2 = 0.4$ (top). It is seen that adjustments in the solid fractions have a small affect on α_∞ and β_∞. An increase in the hydroxide solid fraction (top) inhibits water reaching $r = \alpha$, which slows the reaction at $r = \alpha$ without effecting the reaction at $r = \beta$, and so the proportion of $Mg(OH)_2$ converting to $MgCO_3$ increases leading to closure with a larger fraction of $MgCO_3$, and slightly less Mg corrosion i.e. α_∞ decreases. An increase in the carbonate solid fraction (bottom) slows the reaction at $r = \beta$, so more $Mg(OH)_2$ remains in the system, and there is a greater fraction of $Mg(OH)_2$ at hole closure, so α_∞ increases.

Figure 4.10 shows the effect of the solid fractions, ε_1 and ε_2, on the time scale T_S for $\kappa = 0.03, 0.3, 3$ and $\kappa \to \infty$, $\varepsilon_1 = 0.6$ (bottom) and $\varepsilon_2 = 0.4$ (top). It appears that T_S increases with ε_1 in the top plot, and rises sharply as $\varepsilon_1 \to 1$, which is expected,
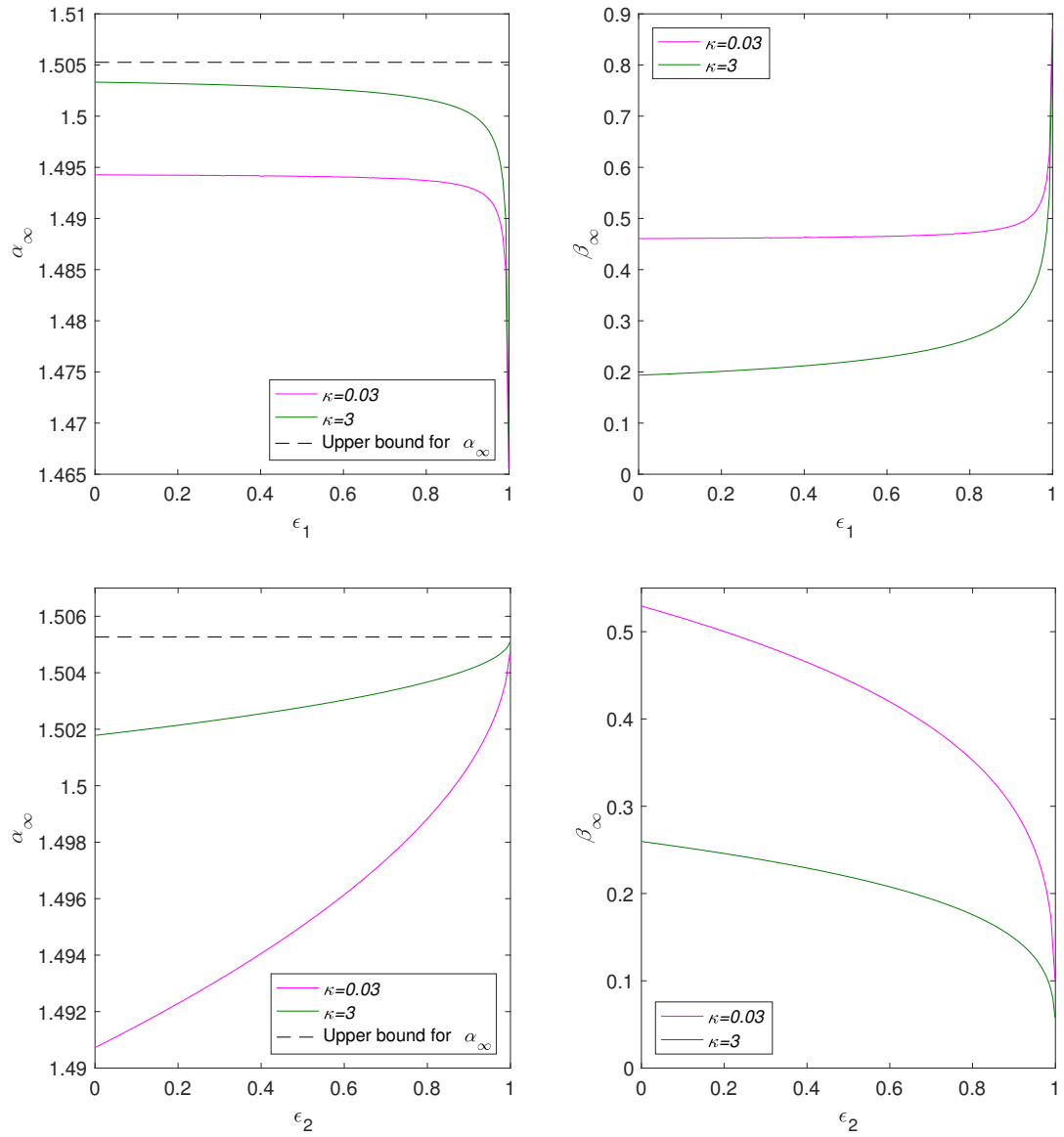
Figure 4.9: Plots of α_∞ and β_∞ against ε_1 (top) and ε_2 (bottom) for $\kappa = 0.03, 3$, $\varepsilon_1 = 0.6$ (bottom) and $\varepsilon_2 = 0.4$ (top). The remaining parameters are listed in Table 3.4 and $P_0 = 1$. The black dashed line represents the upper bound for α_∞, which is 1.5053 using equation (4.20).

because a larger solid fraction in the hydroxide region means that there is less space for the water to diffuse and react with the Mg. As ε_2 increases in the bottom plot of Figure 4.10, then only a subtle increase in T_S is noted, which rises sharply as $\varepsilon_2 \to 1$. This is because a bigger solid fraction reduces the space for water and CO_2

to flow through and react at the boundaries, thereby increasing the pore closure time. Changes in ε_1 appear to have more of an effect on T_S than changes in ε_2.

The "diamond" symbols in Figure 4.10 are the points at which an error was received in the numerical code when $\kappa \to \infty$, $\varepsilon_1 > 0.98$ or $\varepsilon_2 > 0.95$. The error for $\varepsilon_2 > 0.95$ was due to the initial conditions for Phase 1.1 in equations (3.54), which required the subtraction of two error functions with large arguments resulting with a zero on the denominator. Though not implemented, this can partially be resolved using asymptotic series of the error function.

4.5.4 Effect of Rate of Reaction at Magnesium Interface

Contours of $\log(T_S)$ are displayed in Figure 4.11 for a range of values for κ and ε_1 whilst keeping ε_2 constant at 0.4 (top plot), and a range of values for κ and ε_2 whilst keeping ε_1 constant at 0.6 (bottom plot). Different corrosion rates across various magnesium alloys are represented by the variations in κ. The longevity of the pore increases as κ and the void fraction $1 - \varepsilon_1$ decreases. In the plot, when $\kappa = O(10^{-3})$ and $1 - \varepsilon_1 = O(10^{-4})$, the pore takes the longest time to close up at $T_S = 10^{2.7}$, which is approximately 4.5 hours. This would be very rapid in comparison to the time scale of the Mg implant (observed in Chapter 3).

Displayed in Figure 4.12 is the effect on T_S (top) and α_∞ (bottom) as κ varies for $\kappa < 0$ and $\kappa \to \infty$ when $\varepsilon_1 = 0.6$ and $\varepsilon_2 = 0.4$. Evidently, it is seen that the pore closure time decreases as the reaction rate is higher eventually tending to the *Case 1* solution as $\kappa \to \infty$. As expected, a lower reaction rate, κ, indicates that less Mg has corroded at pore closure, and as κ is increased then this leads to the *Case 1* solution for α_∞.
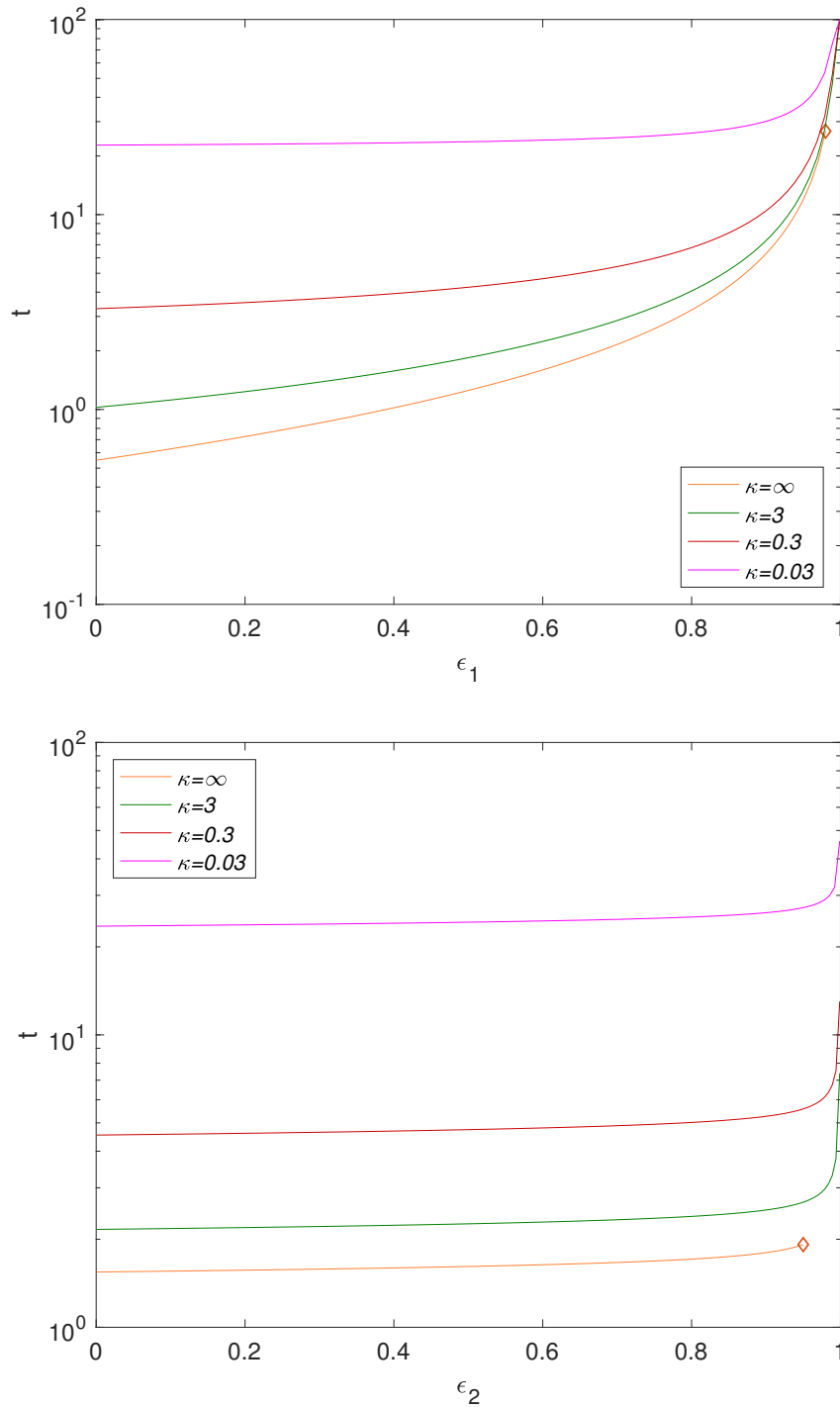
Figure 4.10: Plots of T_S against ε_1 (top) and ε_2 (bottom) for $\kappa = 0.03, 0.3, 3$ and $\kappa \to \infty$, $\varepsilon_1 = 0.6$ (bottom) and $\varepsilon_2 = 0.4$ (top). The remaining parameters are listed in Table 3.4 and $P_0 = 1$. Due to the numerical limitation, computations were only made to the "diamond" symbols when $\kappa \to \infty$ and $\varepsilon_1 > 0.98$ or $\varepsilon_2 > 0.95$.
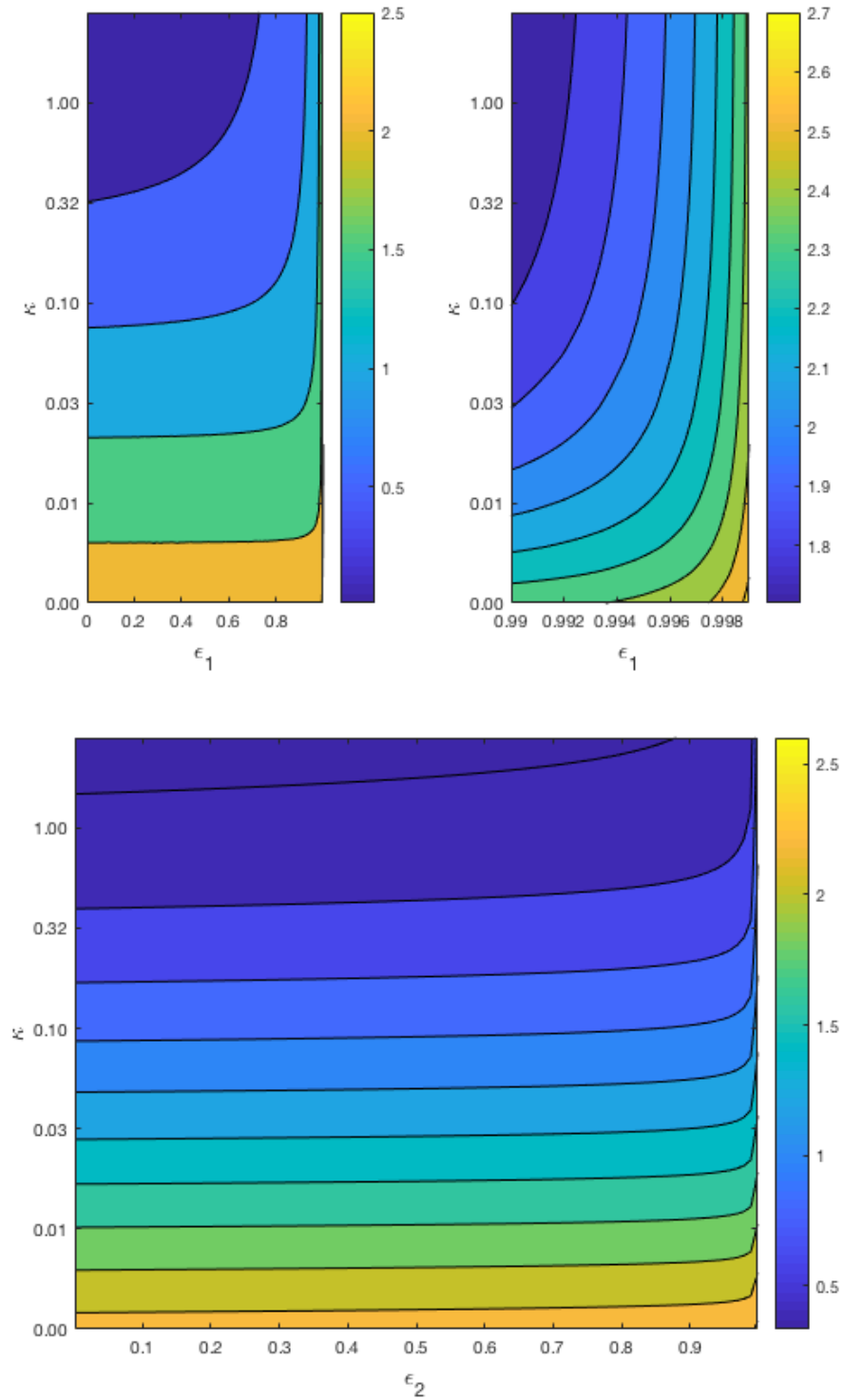
Figure 4.11: Contour plot of $\log(T_S)$ for κ against ε_1 with $\varepsilon_2 = 0.4$ (top) and κ against ε_2 with $\varepsilon_1 = 0.6$ (bottom). The remaining parameters are listed in Table 3.4 and $P_0 = 1$.
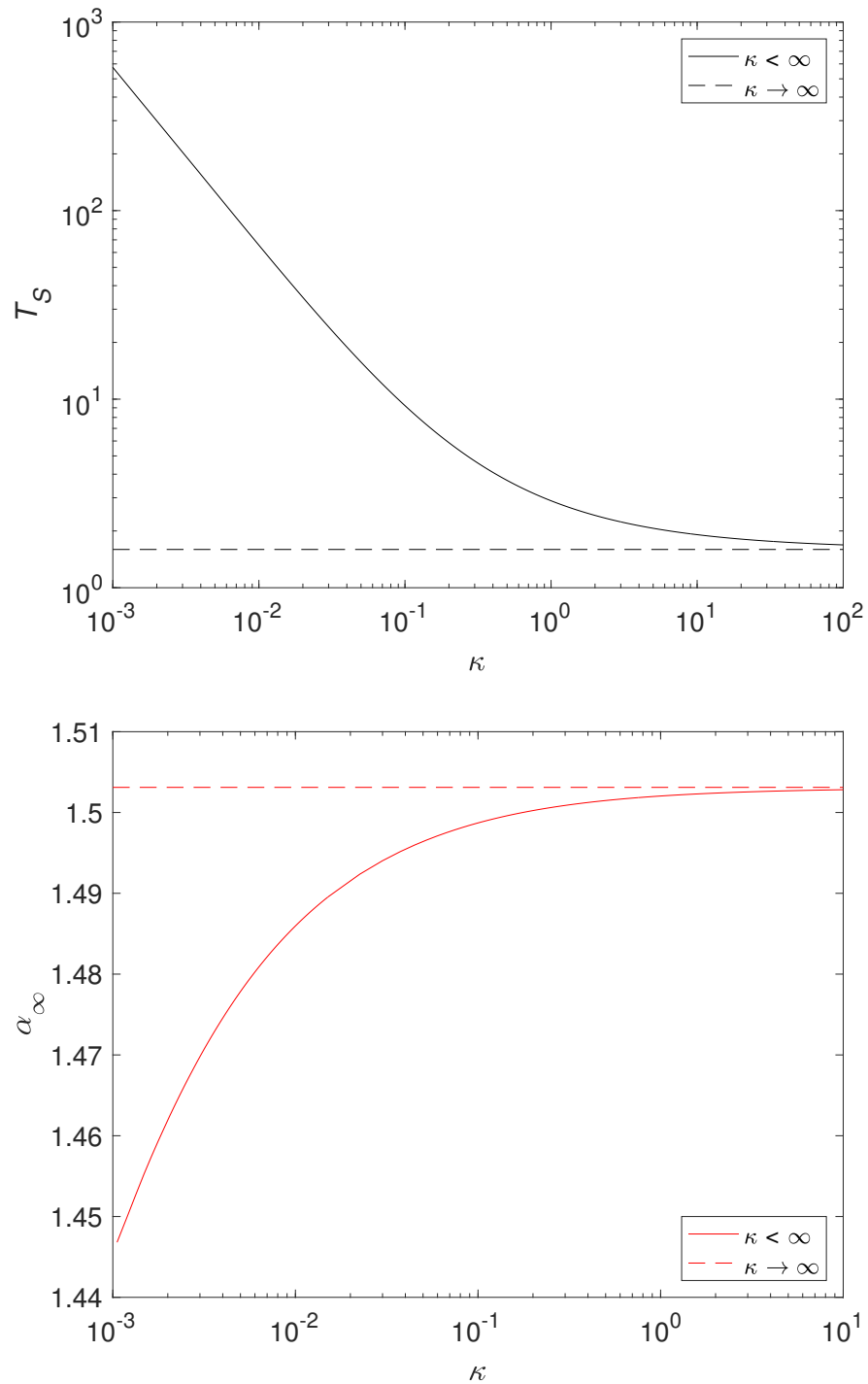
Figure 4.12: Plot of T_S (top) and α_∞ (bottom) against $\kappa < 0$ (solid line) and $\kappa \to \infty$ (dashed line), where $\varepsilon_1 = 0.6$ and $\varepsilon_2 = 0.4$. The remaining parameters are listed in Table 3.4 and $P_0 = 1$. Note that the upper bound for α_∞ is 1.5053 using equation (4.20).

4.6   Conclusion

In practice, a magnesium implant will be porous, because the holes will presumably effect its corrosive properties by aiding its integration into the bone [6, 45]. Hence, the model derived in the previous chapter was adapted here to explore the corrosion inside a single Mg pore. The advection and diffusion of water and carbon dioxide from inside a pore was considered, which formed corrosion products, $Mg(OH)_2$ and $MgCO_3$, as distinct layers deposited on the Mg surface. It was assumed that the outside layer of Mg is inexhaustible.

The model was derived for cylindrical geometry, and, in a similar way to Chapter 3, it was analysed numerically, but small time asymptotic solutions were needed to deal with singularities at initial and certain time points. There are three parameters in the model that are not readily available from the literature, k, ε_1 and ε_2. The results of Section 4.5.3 and 4.5.4 show that these can be tuned to predict a wide range of results in terms of a timescale for the pore closure, $t = T_S$, and the final sizes of α and β, α_∞ and β_∞. At T_S the pore is filled with $MgCO_3$ that is surrounded by $Mg(OH)_2$, which in turn is surrounded by the Mg. The numerical results indicate that changes in k and ε_1 affect T_S, while ε_2 has only a little effect, which is insignificant. Furthermore, it was found that a rise in the $Mg(OH)_2$ solid fraction led to less Mg corroded at T_S, whereas a rise in the $MgCO_3$ solid fraction led to more Mg corroded at $t = T_S$, and a smaller k was found to yield less Mg corrosion at pore closure.

To delay the pore closure time, the reaction rate, k, of a Mg or Mg alloy implant can be lowered. The analysis indicated that pores close within a few hours, which is very rapid in comparison to the life time of an implant. This further suggests that a Mg block, fashioned with pores, will quickly evolve to a heterogeneous structure of Mg, $Mg(OH)_2$ and $MgCO_3$ with potentially some trapped air and hydrogen pockets.

A further parameter that can be tuned in the model is the radius of a Mg pore

P_0, which is, in practice, fully controllable via pore fabrication techniques. In Section 4.5.2, it was found that the thickness of corroded Mg at $t = T_S$ is linearly dependent on the pore size.

The corrosion inside a Mg pore was described well by the model to predict the pore closure time and the final thickness of corroded Mg. The porous media assumption in the model makes it unique for metal corrosion models, while the consideration of corrosion inside a Mg pore extends its novelty. There is capacity to enhance the current model for orthopaedic applications; this is discussed in detail in Section 6.1. However, the work in this chapter provides a groundwork for the exploration of Mg pore corrosion.

Chapter 5

Magnesium in the Blood

Magnesium (Mg) is a biodegradable implant material, which carries the ability to be fully dissolved over time. As the implant degrades, a tissue is formed around the bone releasing magnesium ions into the blood. Magnesium ions are the fourth most abundant cations in the human body, which holds around $21 - 30$g of magnesium [8, 11, 12, 28]. The element is normally sourced from the diet, is stored in bone, muscle, other soft tissues and blood, and is excreted in the urine [5]. A concentration of magnesium lower than 0.65 mmol/l in the serum is classed as a deficiency known as a condition called hypomagnesamia, while a concentration in excess of 1.05 mmol/l is known as a condition called hypermagnesemia [5, 11]. It must be considered that a degrading Mg implant can result in an excess amount of the element in the serum.

In the previous chapters, the degradation of Mg implants was modelled, and since hypermagnesemia can potentially be the outcome of such degradation, this chapter models the effects of Mg in the blood during implantation. In agreement with [20], observing Mg in the serum is a significant aspect of bone implantation to ensure severe symptoms of hypermagnesemia can be prevented. A physiologically based pharmacokinetic (PBPK) model is derived here to study and analyse the effects of plasma Mg with and without the presence of an implant. The model is also applied

to the case when excess Mg is not eliminated from the blood in the usual manner via urinary excretion.

5.1   Background

The human body obtains magnesium from its diet e.g. from consuming water, leafy green vegetables and nuts. Magnesium, like other nutrients, is then broken down in the digestive system, and some of this is absorbed in the intestine while the rest is excreted in the faeces. The absorbed proportion is transferred into the blood compartment where it is filtered in the kidneys; about 95% is normally reabsorbed by the kidneys while the rest is excreted in the urine. The kidneys are able to excrete more or less Mg to help preserve healthy levels in the blood. Bone is the key Mg depository in the body, and there is a continuous exchange between bone and blood [89]. The bone can compensate in the course of an Mg deficiency in the blood, but since Mg is essential for bone strength, repeated compensation can lead to osteoporosis [5, 42]. On the other hand, too much Mg absorption from the bone has damaging effects to the bone [42]. To summarize, a stable level of magnesium in the body is maintained by three major organs, intestine, kidneys and bone [89]. See Figure 5.1 for an overview of Mg metabolism in the human body.

The kidneys are naturally efficient at discarding excess Mg from the blood [8, 90], therefore hypermagnesemia rarely occurs. It is usually only prevalent in patients with renal disease. It can occur in patients that consume a high amount of Mg salts or Mg containing drugs like laxatives and also supplements, but the condition is scarce in the presence of a normal kidney function [90]. Some extreme examples of hypermagnesemia are mentioned in [8, 90], where patients have nearly drowned in the Dead Sea; the Dead Sea contains the worlds most saltiest water with an incredibly high concentration of Mg compared to other oceans and rivers. Furthermore, a fatality
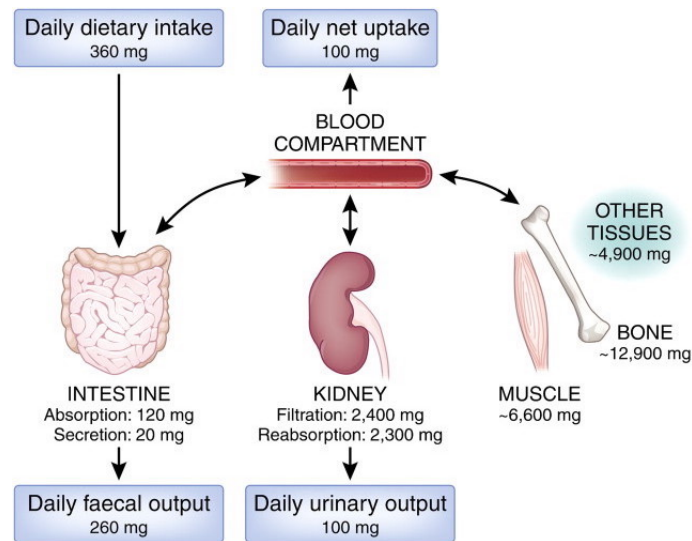
Figure 5.1: Magnesium balance within the human body, taken from [5]

was reported in [91], where hypermagnesemia was caused by laxative use; the authors highlight that, although it is rare, severe hypermagnesmia "frequently" leads to death.

Hypermagnesmia is clinically defined to be when plasma Mg concentrations are above 1.05 mmol/l, however symptoms, which include weakness and difficulty breathing, are only noticeable when levels are above 2 mmol/l [8]. Rising concentrations affect the neuromuscular and cardiovascular systems causing the loss of deep tendon refluxes with electrocardiogram scans generating uncharacteristic results at concentrations more than 3 mmol/l. As concentrations rise even more respiratory depression is experienced eventually leading to cardiac arrest at more than 7 mmol/l [5, 8, 90]. Hence, hypermagnesmia can have severe affects if left uncontrolled. The condition can be treated if it is mild by withdrawing any Mg therapy and if symptoms are more severe then taking calcium salts can be beneficial, but if hypermagnesemia is due to renal disease then dialysis can be performed to clear Mg from the blood [8, 90].

5.2 Modelling the Problem

When an Mg orthopaedic implant is placed in the body, it bonds with the bone to enable healing and as it degrades Mg ions are released into the blood yielding higher plasma Mg levels. Here, Mg metabolism is analysed in order to develop a PBPK model for situations with and without an implant, where the model aims to monitor the effects of an implant on serum concentrations.

The magnesium content in the human body is pinpointed in the bone, muscle, soft tissues, plasma and the red blood cells (RBCs), where the blood compartment is formed of plasma and RBCs [5, 8]. Hence the variables in the mathematical model to follow are denoted

- $s(t)$, Mg mass in the plasma,

- $r(t)$, Mg mass in the RBCs,

- $N(t)$, Mg mass in the bone,

- $T(t)$, Mg mass in the tissue, i.e. muscle and soft tissue,

- $I(t)$, Mg mass in the tissue in the vicinity of the implant,

where $s(t) + r(t) + N(t) + T(t) + I(t) =$ Total Mg in the human body. The definition for mass states that, $i = V_i \times C_i$ where V is volume, C is concentration and $i = s, r, N, T, I$; this notation is used to derive the model.

Around 99% of the total magnesium in the human body is stored in the bone and tissue [5], and from there the element is exchanged to and from the blood compartment. The exchange rates are assumed to be constants k_1, k_{-1}, μ_1 and μ_{-1}. The essential source of Mg in the blood is from the diet, which, for simplicity, is assumed to be sourced at a constant rate ϕ_D. Moreover, it is assumed that the release rate of

magnesium from the implant is σ, which is a constant. The kidneys are responsible for excreting excess Mg in the urine, with rate constant γ.

The concentration of Mg in the serum can be assorted into three groups, ionised, protein bound and complexed with anions [5, 8]. Of the three assortments, the ionised concentration of Mg in the serum, which represents approximately 65%, is exposed and thereby exchangeable from the blood. Hence, the exposed and unexposed content in the serum is mixed with a ratio and interaction rate represented by ξ_1 and λ_1, respectively. The majority of the concentration of Mg in the RBCs is complexed, only a small amount is ionised [92, 93], and so the Mg ions are assumed to be unmixed. The transport of ionised Mg between the different RBCs encounters mixing with the serum. Hence, the exposed content in the RBCs and serum is mixed with ratio and interaction rate represented by ξ_2 and λ_2, respectively.

The bone is a rigid organ in the human body, which consists of a blood vessel to enable the flow of blood, but since bone is solid the movement of Mg ions is very tight; thus there is a region around the blood vessel and the outer edges of the bone that is exposed to blood flow while the rest is unexposed. Therefore Mg ion content in the bone is assumed to be unmixed. Let the exchangeable proportion be represented by ϕ. Similar to bone, tissue consist of blood vessels that enable flow, but Mg ions have slightly more movement here than in bone. The exposed and unexposed content in the tissue is mixed with ratio and interaction rate represented by ξ_3 and λ_3, respectively.

To distinguish between the exposed and unexposed content of Mg, let $\boldsymbol{C_i} = \begin{pmatrix} C_i^e \\ C_i^u \end{pmatrix}$ where C_i^e represents the exposed concentration and C_i^u the unexposed concentration. Figure 5.2 displays a pathway diagram representing Mg networks to and from the serum, RBCs, bone, tissue and implant site in a well-mixed system. It is assumed that the exchange of Mg between serum and implant is related to that between serum and tissue.
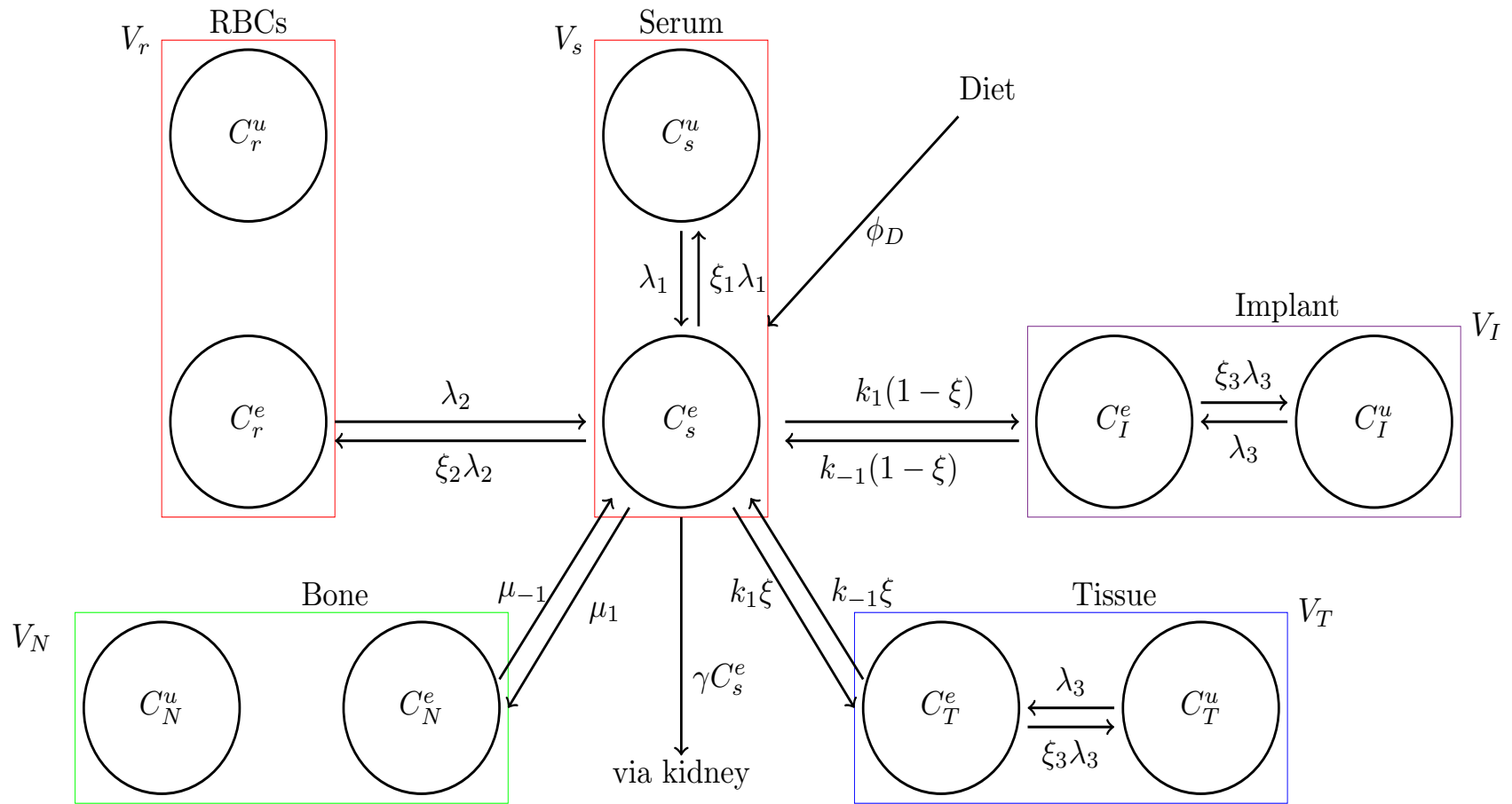
Figure 5.2: Magnesium exchanged to and from the exposed and unexposed concentrations in the serum C_s, RBCs C_r, bone C_N, tissue C_T and implant C_I in a well-mixed tissue compartment system where $\xi = \dfrac{V_T}{V_I + V_T}$.

Tissue	Weight (kg wet wt)	Concentration (mmol/kg wet wt)	Content (mmol)	% of total body magnesium
Serum	3.0	0.85	2.6	0.3
Red blood cells	2.0	2.5	5.0	0.5
Soft tissue	22.7	8.5	193.0	19.3
Muscle	30.0	9.0	270.0	27.0
Bone	12.3	43.2	530.1	52.9
TOTAL	70.0		1000.7	100

Table 5.1: Distribution of magnesium in the average adult human being [7].

5.3   Data

Studies on magnesium physiology and hypermagnesemia have been investigated to determine approximate values for the parameters in the model. Healthy levels of plasma Mg are recognised to be in the range 0.65 - 1.05 mmol/l, more than this refers to hypermagnesemia. Concentrations above 3 mmol/l can be problematic, and above 7 mmol/l can lead to cardiac arrest [5]. For the numerical analysis to follow, 3 mmol/l is considered to be high Mg levels that require immediate attention.

Data for the amount of Mg in the human body is taken from [5, 7, 8], see Table 5.1. An average 70 kg adult human body is found to consist of 1000.7 mmol magnesium, 530.1 mmol of this is in the bone, 193 mmol is present in the soft tissue, 270 mmol is in the muscle, 2.6 mmol is in the serum and 5 mmol is in the RBCs. The wet weight of each is displayed in Table 5.1, from which the volumes and initial concentrations in the model are determined in Table 5.3. For the tissue concentration, the muscle and soft tissue from Table 5.1 are combined.

An average dietary intake of 15 mmol (or 360 mg) per day is taken from [5] and [89]. As mentioned before, some of this dietary intake is absorbed by the intestine; further to this about 0.8 mmol (or 20 mg) is secreted from the blood to the intestine. After intestinal absorption and blood secretion, 4 mmol (or 100 mg) of magnesium per day is reported to be transferred to the blood [89, 90], therefore $\phi_D = 4$ mmol/day.

Location	Exposed Mg (%)
Serum	65
RBCs	8
Bone	33.3
Tissue	25

Table 5.2: Percentage of exchangeable Mg in serum, RBCs, bone and tissue sourced from [5, 8].

The mass exchange rates of magnesium between blood and tissue, k_1, and between blood and bone, μ_1, appear not to be reported in the literature. Reference values for these parameters are attained from [94], where the paper provides a plethora of reference values for PBPK model parameters. The values they provide are not compound or element specific, but have been used in other PBPK modelling studies, such as [95] for zinc oxide and [96] for manganese. The blood flow rates are identified as fractions of cardiac output, which is well known to be 5 l/min for an average 70 kg human being. Here 4.2% of the cardiac output is reported to flow to the bone, while the rest flows to the tissues [94]; this gives data for k_1 and μ_1. For the k_{-1} and μ_{-1} values, the homoeostatic state predicted by the model in Section 5.4 is used, from which it can be declared $\dfrac{k_{-1}}{k_1} \sim \dfrac{\bar{C}_s^e}{\bar{C}_T^e}$ and $\dfrac{\mu_{-1}}{\mu_1} \sim \dfrac{\bar{C}_s^e}{\bar{C}_N^e}$. The bars represent homoeostatic components. See Table 5.3 for the parameter values.

The kidneys are responsible for excreting excess magnesium in the urine. It is known that they have the potential to increase and decrease excretion depending on plasma levels [5]. Studies report that normally 4 mmol of magnesium is expected to appear in the urine per day [5, 8, 89, 90], hence under healthy conditions $\gamma \bar{C}_s^e = 4$ mmol/day $\Rightarrow \gamma = 7.3$ l/day.

Parameter	Description	Value	Units	Source
V_s	Volume of serum	3	L	[5, 8]
V_r	Volume of RBCs	2	L	[5, 8]
V_N	Volume of bone	12.3	L	[5, 8]
V_T	Volume of tissues	52.7	L	[5, 8]
V_I	Volume of implant	0.00419	L	-
$\bar{C}_s^e$	Homoeostatic exposed concentration in serum	0.55	mmol/l	R
$\bar{C}_r^e$	Homoeostatic exposed concentration in RBCs	0.2	mmol/l	R
$\bar{C}_N^e$	Homoeostatic exposed concentration in bone	14.4	mmol/l	R
$\bar{C}_T^e$	Homoeostatic exposed concentration in tissue	2.2	mmol/l	R
$\bar{C}_s^u$	Homoeostatic unexposed concentration in serum	0.30	mmol/l	R
$\bar{C}_r^u$	Homoeostatic unexposed concentration in RBCs	2.3	mmol/l	R
$\bar{C}_N^u$	Homoeostatic unexposed concentration in bone	28.8	mmol/l	R
$\bar{C}_T^u$	Homoeostatic unexposed concentration in tissue	6.6	mmol/l	R
ϕ_D	Mg dietary intake rate after intestine absorption	4	mmol/day	[5, 8]
σ	Mg implant release rate	F	mmol/day	-
γ	Excretion rate constant of Mg in the urine	7.3	l/day	[5, 8]
μ_1	Exchange rate constant from blood to bone	302.4	l/day	[94]
μ_{-1}	Exchange rate constant from bone to blood	1.3	l/day	H
k_1	Exchange rate constant from blood to tissue	6897.6	l/day	[94]
k_{-1}	Exchange rate constant from tissue to blood	1.2	l/day	H
ξ_1	Equilibration ratio of exposed and unexposed in serum	0.54	-	R
ξ_2	Equilibration ratio of exposed in serum and exposed in RBCs	0.36	-	R
ξ_3	Equilibration ratio of exposed and unexposed in tissue	3	-	R
ϕ	Equilibration of exchangeable Mg in bone	3	-	R
λ_1	Rate of equilibration between exposed and unexposed in serum	A	l/day	-
λ_2	Rate of equilibration between exposed in serum and exposed in RBCs	A	l/day	-
λ_3	Rate of equilibration between exposed and unexposed in tissue	A	l/day	-

Table 5.3: Values for the model parameters for healthy individuals, where F is a free parameter, R is derived using Table 5.1 and Table 5.2, H is derived from homoeostasis, A is unknown but is large in comparison to dimensionally equivalent parameters.

Ionised Mg ions in the serum are exposed, while the protein bound and complexed are unexposed. The ratio between the exposed and unexposed is 0.65 : 0.35 [5, 8], which means $\xi_1 = 0.54$. The ionised Mg in RBCs is identified to be 0.2 mmol/l [93], and comparing this to the ionised concentration in the serum $\xi_2 = 0.36$. Approximately a third of the Mg content in the bone is exchangeable, and a quarter in skeletal muscle and liver are exchangeable [5, 8]. The distribution of Mg in the skeletal muscle is provided in Table 5.1. The liver is part of the soft tissue. To find the concentration of liver alone, the wet weight of liver is 1.55 kg, and approximately 14 mg of Mg is present in every 100g of pig liver; pig liver is comparable to human liver [97, 98]. Therefore, the amount of Mg in the liver is 217 mg, which gives a liver concentration of 5.8 mmol/l. Since this concentration is close to that of soft tissue, which is 8.5 mmol/l in Table 5.1, then, for simplicity, it is assumed that a quarter of T is exchangeable, hence $\xi_3 = 3$. The rates of equilibration within phase, λ_1, λ_2 and λ_3, are assumed to be much more rapid than that for the other processes; this will be explored for the model simplification.

When an Mg implant is present, the model can be tuned for various values of V_I, which is the volume of the implant. In Chapter 3, when modelling the corrosion of Mg a sample size of 1 cm radius was employed, and for an Mg sphere this refers to a volume of 4.19 cm^3 or 4.19×10^{-3} l. Hence, for the analysis in this chapter, a reference value for V_I is set constant at 4.19×10^{-3} l.

The percentage of the exchangeable Mg in the serum, RBCs, bone and tissue are displayed in Table 5.2, and the model parameter values are displayed in Table 5.3.

5.4 Mathematical model

The following mass-balance PBPK equations are derived from Figure 5.2, for blood

$$
V_s \frac{dC_s^e}{dt} = \phi_D - \mu_1 C_s^e + \mu_{-1} C_N^e - k_1 C_s^e + k_{-1}(\xi C_T^e + (1-\xi)C_I^e) - \gamma C_s^e +
$$
$$
\lambda_1(C_s^u - \xi_1 C_s^e) + \lambda_2(C_r^e - \xi_2 C_s^e),
$$
$$
V_s \frac{dC_s^u}{dt} = -\lambda_1(C_s^u - \xi_1 C_s^e),
$$
$$
V_r \frac{dC_r^e}{dt} = -\lambda_2(C_r^e - \xi_2 C_s^e),
$$
$$
V_r \frac{dC_r^u}{dt} = 0,
$$

$$(5.1)$$

for bone

$$
\phi V_N \frac{dC_N^e}{dt} = \mu_1 C_s^e - \mu_{-1} C_N^e,
$$
$$
(1-\phi)V_N \frac{dC_N^u}{dt} = 0,
$$

$$(5.2)$$

for tissue

$$
V_T \frac{dC_T^e}{dt} = \xi(k_1 C_s^e - k_{-1} C_T^e) + \lambda_3(C_T^u - \xi_3 C_T^e),
$$
$$
V_T \frac{dC_T^u}{dt} = -\lambda_3(C_T^u - \xi_3 C_T^e),
$$

$$(5.3)$$

and for the implant zone

$$
V_I \frac{dC_I^e}{dt} = \sigma + (1-\xi)(k_1 C_s^e - k_{-1} C_I^e) + \lambda_3(C_I^u - \xi_3 C_I^e),
$$
$$
V_I \frac{dC_I^u}{dt} = -\lambda_3(C_I^u - \xi_3 C_I^e),
$$

$$(5.4)$$

where $\xi = \dfrac{V_T}{V_I + V_T}$; all constant parameters are explained in Table 5.3. Initial conditions represent the homoeostatic state, and these are

$$C_s^j(0) = \bar{C}_s^j, \quad C_r^j(0) = \bar{C}_r^j \quad C_N^j(0) = \bar{C}_N^j, \quad C_T^j(0) = \bar{C}_T^j, \quad C_I^j(0) = \bar{C}_T^j, \qquad (5.5)$$

where $j = e, u$. Equations (5.1) and (5.2) imply that C_r^u and C_N^u are constant, so $C_r^u = \bar{C}_r^u$ and $C_N^u = \bar{C}_N^u$.

To analyse this model, the system is first non-dimensionalised, and then the model is reduced based on rapid equilibration between some phase variables.

5.4.1 Non-dimensionalisation and Reduction

There are a number of timescale in the system, e.g. timescale for equilibration within a phase (assumed fast at $O(\text{secs})$), between phases (slower at $O(\text{mins})$), time at excretion (slower at $O(\text{hours/days})$) and implant occupation ($O(\text{months})$). Here, time is rescaled with respect to the second fastest timescale using

$$t = \widehat{t}\frac{V_s}{k_1};$$

and concentrations are rescaled using the following

$$C_s^j = \bar{C}_s^e\widehat{C}_s^j, \qquad C_r^j = \bar{C}_s^e\widehat{C}_r^j, \qquad C_N^j = \frac{\mu_1}{\mu_{-1}}\bar{C}_s^e\widehat{C}_N^j, \qquad C_T^j = \frac{k_1}{k_{-1}}\bar{C}_s^e\widehat{C}_T^j,$$

$$C_I^j = \frac{k_1}{k_{-1}}\bar{C}_s^e\widehat{C}_I^j,$$

where the hats represent dimensionless variables. Using the data in Table 5.3, the scaling implies that $\widehat{t} = 1$ represents 1.04 minutes. The following dimensionless

parameters are defined

$$S = \frac{\sigma V_s k_{-1}}{\bar{C}_s^e V_I k_1^2}, \qquad \mu = \frac{\mu_1}{k_1}, \qquad \Gamma = \frac{\gamma}{k_1}, \qquad \xi = \frac{V_T}{V_I + V_T}, \qquad \xi_B = \frac{V_s}{V_r} \qquad \xi_N = \frac{V_s \mu_{-1}}{V_N \mu_1},$$

$$\xi_T = \frac{V_s k_{-1}}{V_T k_1}, \qquad \frac{1}{\epsilon} = \frac{\lambda_1}{k_1}, \qquad \frac{\widehat{\lambda}_{3_0}}{\epsilon} = \frac{\lambda_2}{k_1}, \qquad \frac{\widehat{\lambda}_{3_1}}{\epsilon} = \frac{V_s \lambda_3}{V_T k_1}, \qquad \frac{\widehat{\lambda}_{3_2}}{\epsilon} = \frac{V_s \lambda_3}{V_I k_1},$$

where it is assumed that $\gamma = \frac{\phi_D}{\bar{C}_s^e}$; and after dropping the hats for clarity, the following system is attained,

$$\frac{dC_s^e}{dt} = \Gamma(1 - C_s^e) + \mu(C_N^e - C_s^e) + \xi(C_T^e - C_s^e) + (1 - \xi)(C_I^e - C_s^e) + \frac{1}{\epsilon}(C_s^u - \xi_1 C_s^e) +$$

$$\frac{\lambda_{3_0}}{\epsilon}(C_r^e - \xi_2 C_s^e),$$

$$\frac{dC_s^u}{dt} = -\frac{1}{\epsilon}(C_s^u - \xi_1 C_s^e), \tag{5.6}$$

$$\frac{dC_r^e}{dt} = -\frac{\xi_B \lambda_{3_0}}{\epsilon}(C_r^e - \xi_2 C_s^e)$$

$$\phi \frac{dC_N^e}{dt} = \mu \xi_N(C_s^e - C_N^e), \tag{5.7}$$

$$\frac{dC_T^e}{dt} = \xi \xi_T(C_s^e - C_T^e) + \frac{\lambda_{3_1}}{\epsilon}(C_T^u - \xi_3 C_T^e),$$

$$\frac{dC_T^u}{dt} = -\frac{\lambda_{3_1}}{\epsilon}(C_T^u - \xi_3 C_T^e), \tag{5.8}$$

$$\frac{dC_I^e}{dt} = S + \xi \xi_T(C_s^e - C_I^e) + \frac{\lambda_{3_2}}{\epsilon}(C_I^u - \xi_3 C_I^e),$$

$$\frac{dC_I^u}{dt} = -\frac{\lambda_{3_2}}{\epsilon}(C_I^u - \xi_3 C_I^e), \tag{5.9}$$

with initial conditions

$$C_s^e(0) = C_N^e(0) = C_T^e(0) = C_I^e(0) = 1, \quad C_r^e(0) = \frac{\bar{C}_r^e}{\bar{C}_s^e}, \tag{5.10}$$

$$C_s^u(0) = \frac{\bar{C}_s^u}{\bar{C}_s^e}, \quad C_T^u(0) = C_I^u(0) = \frac{k_{-1}\bar{C}_T^u}{k_1\bar{C}_s^e}. \tag{5.11}$$

Recall that C_r^u and C_N^u are constant.

It is assumed that the timescale for Mg exchange within each phase is much faster than that across phases, which means that $\epsilon \ll 1$. Therefore, the leading order balance in (5.6)-(5.9) gives

$$C_s^u \sim \xi_1 C_s^e, \qquad C_r^e \sim \xi_2 C_s^e, \qquad C_T^u \sim \xi_3 C_T^e, \qquad C_I^u \sim \xi_3 C_I^e, \tag{5.12}$$

hence

$$C_s^u + C_s^e + C_r^e \sim (1 + \xi_1 + \xi_2)C_s^e, \qquad C_T^u + C_T^e \sim (1 + \xi_3)C_T^e,$$

$$C_I^u + C_I^e \sim (1 + \xi_3)C_I^e$$

as $\epsilon \longrightarrow 0$. Applying the above to the equations in (5.6), (5.8) and (5.9) leads to the following reduced system

$$\frac{dC_s^e}{dt} = \frac{1}{1 + \xi_1 + \xi_2}\left[\Gamma(1 - C_s^e) + \mu(C_N^e - C_s^e) + \xi(C_T^e - C_s^e) + (1 - \xi)(C_I^e - C_s^e)\right], \tag{5.13}$$

$$\frac{dC_N^e}{dt} = \frac{1}{\phi}\left[\mu\xi_N(C_s^e - C_N^e)\right], \tag{5.14}$$

$$\frac{dC_T^e}{dt} = \frac{1}{1 + \xi_3}\left[\xi\xi_T(C_s^e - C_T^e)\right], \tag{5.15}$$

$$\frac{dC_I^e}{dt} = \frac{1}{1 + \xi_3}\left[S + \xi\xi_T(C_s^e - C_I^e)\right]. \tag{5.16}$$

From now on in this chapter C_i is used to refer to C_i^e.

5.5 Steady State Analysis

A steady-state analysis is conducted using the model in (5.13)-(5.16). The following steady state is identified when no implant is present and $\Gamma > 0$,

$$(C_s, C_N, C_T) = (1, 1, 1), \tag{5.17}$$

because the homoeostatic state was rescaled to 1. Evidently, when there is no Mg source from the diet ($\Gamma = 0$), then a zero steady state is attained in (5.17).

The presence of an implant, when $S > 0$, yields the following steady state for (C_s, C_N, C_T, C_I)

$$\left(\frac{(\Gamma\xi_T - S)\xi + S}{\Gamma\xi\xi_T}, \frac{(\Gamma\xi_T - S)\xi + S}{\Gamma\xi\xi_T}, \frac{(\Gamma\xi_T - S)\xi + S}{\Gamma\xi\xi_T}, \frac{(\xi\xi_T + S)\Gamma + (1 - \xi)S}{\Gamma\xi\xi_T} \right), \tag{5.18}$$

where $S = 0$ results in (5.17). As $\Gamma \to 0$ the steady state in (5.18) refers to infinite magnesium concentrations; this is to be expected because as less Mg is excreted in the urine, Γ becomes smaller, and hence, in the presence of an implant, the concentrations rise.

The Jacobian matrix for equations (5.13)-(5.16) is

$$\begin{pmatrix} -\Gamma - \mu - 1 & \mu & \xi \\ \xi_N\mu & -\xi_N\mu & 0 \\ \xi\xi_T & 0 & -\xi\xi_T \end{pmatrix}, \tag{5.19}$$

for (5.17), and

$$\begin{pmatrix} -\Gamma - \mu - 1 & \mu & \xi & 1 - \xi \\ \xi_N \mu & -\xi_N \mu & 0 & 0 \\ \xi \xi_T & 0 & -\xi \xi_T & 0 \\ \xi \xi_T & 0 & 0 & -\xi \xi_T \end{pmatrix}, \tag{5.20}$$

for (5.18). The following characteristic polynomial is attained

$$\begin{aligned} g(x) \quad &= x^3 + (\xi \xi_T + (\xi_N + 1)\mu + \Gamma + 1)x^2 + (((\xi_N + 1)\mu - \xi + \Gamma + 1)\xi \xi_T + \\ &\quad \mu \xi_N (\Gamma + 1))x - \mu \xi \xi_T \xi_N (\xi - \Gamma - 1), \end{aligned} \tag{5.21}$$

for (5.19), where the coefficients of x are all positive because $(1 - \xi) > 0$. Hence with no sign change Descartes rule of signs implies there are no positive real roots. Now writing $g(-x)$ results in 3 sign changes between the coefficients of x from one term to the next, so there are 1 or 3 negative real roots. The Gershgorin circle theorem states that for an $n \times n$ matrix A, each eigenvalue λ_1, lies within a disc of radius R_i, defined as $R_i = \sum_{j=1; i \neq j}^{n} |a_{ij}|$, centred at a_{ii} in the complex plane. Such a disc is called a Gershgorin disc [99]. Applying this to the Jacobian matrix in (5.19) reveals that there are 3 eigenvalues with a negative real part. Therefore, the steady state, when no implant is present and $\Gamma > 0$, is stable.

The characteristic polynomial for (5.20) is

$$\begin{aligned} h(x) \quad &= x^4 + (2\xi_T \xi + \mu \xi_N + \Gamma + \mu + 1)x^3 + (\xi_T^2 \xi^2 + 2\mu \xi \xi_T \xi_N + 2\Gamma \xi_T \xi + \Gamma \mu \xi_N + \\ &\quad 2\mu \xi_T \xi + \xi_T \xi + \mu \xi_N)x^2 + (\mu \xi_T^2 \xi^2 \xi_N + \Gamma \xi_T^2 \xi^2 + 2\Gamma \mu \xi_T \xi \xi_N + \mu \xi_N^2 \xi^2 + \mu \xi_T \xi \xi_N)x + \\ &\quad \Gamma \mu \xi_T^2 \xi^2 \xi_N, \end{aligned} \tag{5.22}$$

Parameter	Value
S	-
μ	0.0438
Γ	0.0011
ξ	0.99992
ξ_T	0.0142
ξ_N	0.0093
ξ_1	0.54
ξ_2	0.36
ξ_3	3
ϕ	3

Table 5.4: Dimensionless parameters in the model for healthy individuals, which are found using data in Table 5.3; the parameter S is controlled by the implant release rate.

where Descartes rule of signs implies that there are 0, 2 or 4 negative real roots. Applying the Gershgorin theorem to (5.20) reveals that all eigenvalues have negative real parts or 1 negative real part and 3 eigenvalues at 0. As the constant coefficient in (5.22) is non-zero there cannot be any 0 roots, therefore there are 4 eigenvalues with a negative real part. So the steady state in (5.18) is stable, and represents a homoeostasis state adapted to the implant.

5.6   Numerical Simulations

The system in (5.13)-(5.16) is solved in MATLAB using *ode15s*. In this section, simulations are generated for the model using the dimensionless parameters in Table 5.4, where parameters S and Γ are varied. Unless otherwise stated, Γ represents the healthy urine excretion rate in Table 5.4.

Up-to $t = 0$, there is no implant, and the Mg ion concentrations are set at homoeostatic state, $(C_i = 1, i = s, N, T)$. At $t = 0$, the implant is installed releasing Mg into the system (i.e. $S > 0$) at a rate controlled through the parameter S. The plot in Figure 5.3 is generated using Table 5.4 when $S = 2.4 \times 10^{-3}$ (corresponding to $\sigma = 0.05$ mmol/day), where the concentrations are displayed over time. It is seen
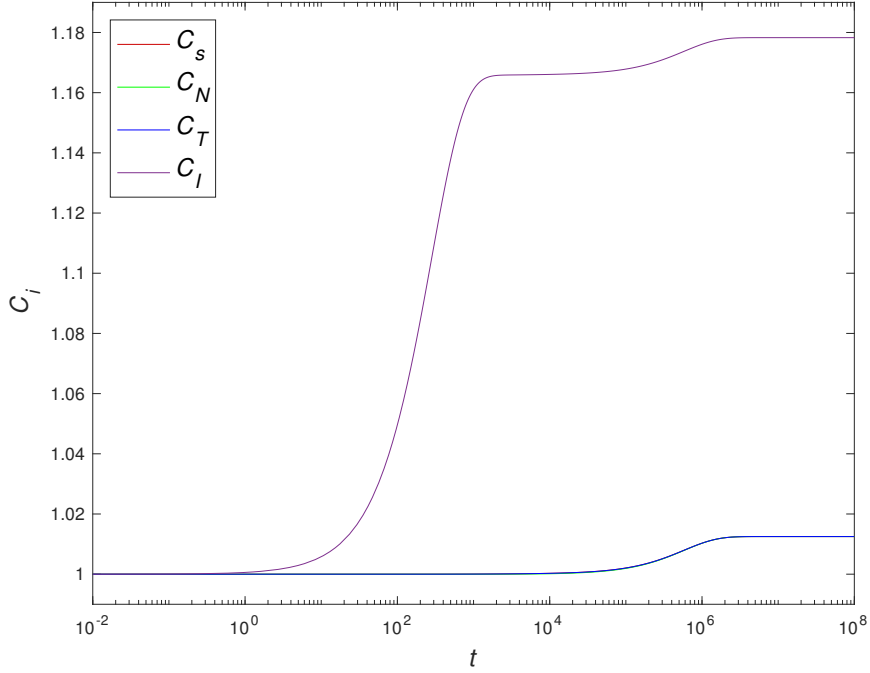
Figure 5.3: Plot of the dimensionless concentrations over time using the parameter values in Table 5.4 and $S = 2.4 \times 10^{-3}$. The variables C_s, C_N, C_T all overlap each other.

that the concentrations start at healthy levels and a rise in C_I is followed by a rise in C_s, C_N, C_T; the concentrations C_s, C_N, C_T overlap each other reflecting that the Mg in the serum, bone, and tissue equilibrate rapidly. While the tissue is acting as a reservoir of the Mg there is no rise in C_I, but then this eventually results in a further rise in C_I. The timescales for these and intermediate events are analysed. The C_I value can be approximated using the following argument, for $1 - \xi \ll 1$.

Initially, when $C_s, C_N, C_T \sim 1$, using equations (5.13)-(5.16) it follows that

$$\frac{dC_I}{dt} \sim \frac{1}{1 + \xi_3}\big[S + \xi\xi_T(1 - C_I)\big], \tag{5.23}$$

at that time. Using the initial condition in (5.11), equation (5.23) is solved to give

$$C_I \sim 1 + (\frac{S}{\xi\xi_T})\Big[1 - \exp(-\frac{\xi\xi_T}{1 + \xi_3}t)\Big],$$

so

$$C_I \sim C_I^* \sim 1 + \frac{S}{\xi\xi_T}, \tag{5.24}$$

as the timescale $t \longrightarrow \infty$ for the phase. Using the values in Table 5.4, this gives $C_I^* = 1.169$, which is in close agreement with Figure 5.3.

Equation (5.24) causes a rise in C_s from which equation (5.13) gives

$$\frac{dC_s}{dt} \sim \frac{1}{1 + \xi_1 + \xi_2}(1 - \xi)(C_I^s - C_s),$$

and this is solved using the initial condition in (5.11) to give the following

$$C_s \sim 1 + \frac{S}{\xi\xi_T}\Big[1 - e^{-\frac{(1 - \xi)t}{(1 + \xi_1 + \xi_2)}}\Big], \tag{5.25}$$

where it is known that $(1 - \xi) \ll 1$. So Mg serum concentrations are expected to move from its homoeostatic level when $t = O(1/(1 - \xi))$. Using the values in Table 5.4, this predicts $t \approx 1.25 \times 10^4$, which is in good agreement with Figure 5.3.

In the dimensionless model, hypermagnesemia is diagnosed when $C_s = 1.24$, (which corresponds to 1.05 mmol/l), hence for the case in Figure 5.3 this is not apparent. When increasing the parameter S, hypermagnesemia is more likely to occur.

In Chapter 3, the degradation time for a 1 cm radius sphere was identified for a range of parameter values, from which a full degradation time of 100 days can be
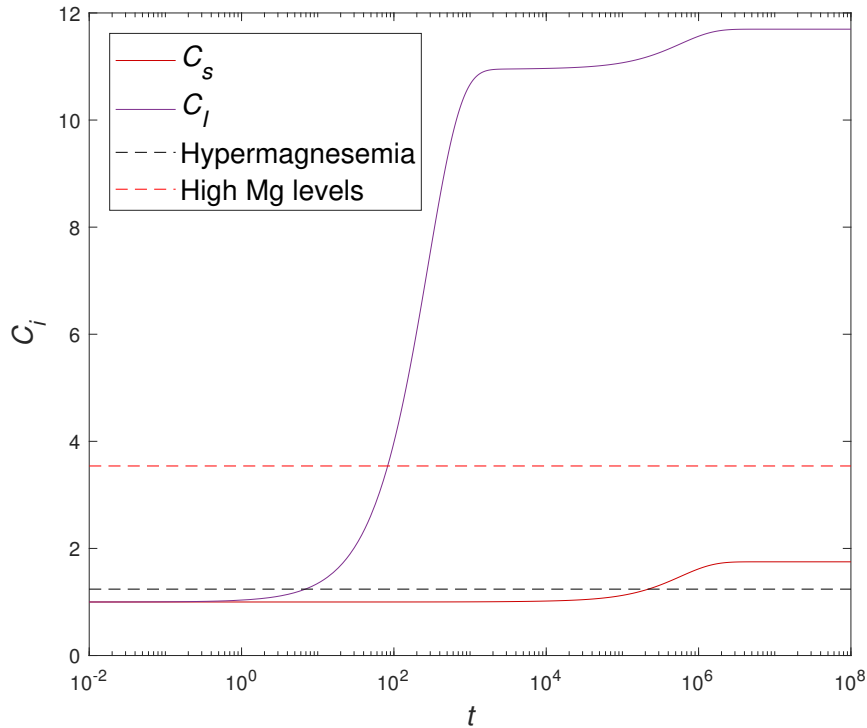
Figure 5.4: Plot of the dimensionless concentrations over time using the parameter values in Table 5.4 and $S = 0.14$. Hypermagnesemia occurs when C_s is above 1.24 (black dashed line), and reaches higher levels where symptoms can be more severe when C_s is above 3.54 (red dashed line), at which point immediate action should be taken.

taken. Using the density and molecular mass of Mg, a 1 cm radius of a sphere is equivalent to 290 mmol. Therefore, σ can be estimated to be 3.00 mmol/day, which equates to $S = 0.14$. Figure 5.4 displays the concentration of the blood and the implant over time when $S = 0.14$ where hypermagnesemia, represented by the black dashed line, is diagnosed. The blood concentration is below the high levels of Mg represented by the red dashed line at $C_s = 3.54$, (which corresponds to 3 mmol/l). So if a spherical Mg implant of 1 cm radius degrades in 100 days, hypermagnesemia will be diagnosed and any Mg in the diet should be maintained or reduced for the 100 days until the implant degrades.

A well functioning kidney is usually sufficient at keeping hypermagnesemia at bay,

because, as stated before, the kidneys have the ability to excrete any excess Mg in the urine. For this reason, hypermagnesemia is usually only perceived in patients with a compromised renal function. For the simulations up to now, the urinary excretion parameter, Γ, was kept constant at a healthy level. With kidney failure taken into consideration, values for Γ are varied to investigate the steady state for the blood concentration with various values for the implant release rate S; this is shown in Figure 5.5 for a range of values of Γ when $S \approx 0.02, 0.05, 0.1, 0.2, 0.3$ (corresponding to $\sigma = 0.45, 1.1, 2.2, 4.4, 6.5$ mmol/day). The black dashed line in Figure 5.5 represents hypermagnesemia, and the red dashed line represents higher levels of Mg. The dotted line represents urine excretion at a healthy level. It is seen that at a healthy Γ, the green curve, which represents a high implant release rate, is just below the red dashed line. The plot displays that a low Γ rapidly increases Mg concentrations in the blood to infinite levels, the patient would presumably not survive at such high levels for long periods. Hypermagnesemia appears to be quite severe when Γ is less than half of the healthy excretion rate, especially as the implant release rate is higher. The result suggests that kidney function must be monitored before Mg implantation, so that an appropriate implant release rate can be determined.

5.7   Conclusion

A PBPK based model has been developed and analysed in this chapter to model magnesium metabolism with and without an implant. The key goal of the model is to investigate Mg in the serum so that the possibility of hypermagnesemia can be illustrated during Mg implantation. Research highlights that the three organs governing Mg homoeostasis in the body are intestine, bone and kidney. From the diet, some Mg is absorbed in the intestine and transferred to the blood compartment, where it can then be transferred to bone and tissue; any excess Mg is filtered in the
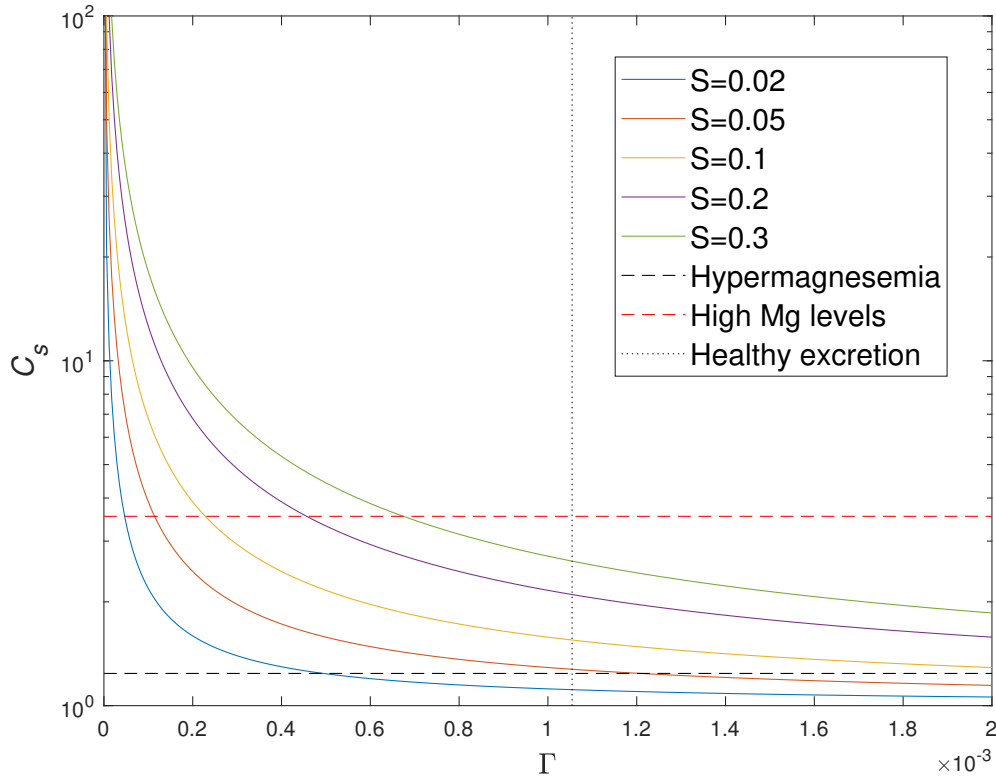
Figure 5.5: Plot of dimensionless plasma Mg concentration against Γ using the parameter values in Table 5.4 and various implant release rates of $S \approx 0.02, 0.05, 0.1, 0.2, 0.3$. Hypermagnesemia occurs when C_s is above 1.24 (black dashed line) and reaches a more higher level that needs immediate attention when C_s is above 3.54 (red dashed line).

kidney and excreted in the urine. The model was derived by consideration of the dynamics of Mg distribution within and between major compartments, blood, tissue, bone and implant, based on Mg metabolism.

When no implant is present, the diet and urine excretion rates are significant parameters for maintaining normal plasma Mg; these are assumed to be constant in the model. The steady state analysis in the model indicated that the concentrations of blood, bone and tissue remain at a stable steady state without the presence of an implant.

When an implant is present, the concentration of Mg in the implant region tends

to a higher steady state than that of blood, bone and tissue. The model simulations indicate that the blood, bone and tissue equilibrate rapidly and that the tissue, due to its much greater volume, acts as a reservoir. Evidently, as the implant release rate is increased in the simulations, the risk of hypermagnesemia appears to be increased (see Figure 5.3 and 5.4).

For a renal disease case, an Mg implant is more likely to cause hypermagnesemia, because the kidneys are unable to excrete excess Mg at a fast enough rate. Therefore, the model was explored for various values of the excretion rate to detect blood serum levels for different implant release rates (see Figure 5.5). The result shows a rapid rise in blood concentrations for a smaller excretion rate. In practice, an extremely low excretion rate may result in fatalities, thus underlining the importance of monitoring kidney function before Mg implantation in vulnerable patients.

Hypermagnesemia can potentially occur after Mg ions are released into the serum during Mg implantation [20]. As a fresh look into Mg implantation, here, the effects on the serum concentrations were explored using mathematical modelling. The model derived is a simple but capable tool for detecting plasma Mg to ensure that hypermagnesemia or higher levels of Mg can be avoided during implantation, and is also applicable for patients that are screening for renal function. In Section 6.1, some potential work for future reference is discussed in order to further enhance the model.

Chapter 6

Discussion

Magnesium (Mg) based orthopaedic implants are hailed for their mechanical and physical properties that can enhance bone healing, but their rapid corrosion in aqueous environments has become an obstacle for their use. As a result, there is considerable research into controlling magnesium corrosion, for example through alloying and coating, and the physiological effects of magnesium corrosion have also been widely studied. However, the use of mathematical modelling in this area is very scarce. In this thesis, the degradation of magnesium was studied via the development of four new mathematical models.

As explained in Section 1.2, Mg reacts with H_2O in the physiological environment to form magnesium hydroxide ($Mg(OH)_2$). In this work, it was acknowledged that the hydroxide can then react with CO_2 from the bicarbonate ions in the environment or *in vitro* to form magnesium hydrogen carbonate ($Mg(HCO_3)_2$), which decomposes to form a more stable product, magnesium carbonate ($MgCO_3$). The consideration of the reaction between $Mg(OH)_2$ and CO_2 is a novel feature for mathematical modelling of Mg. The first corrosion model, in Chapter 2, is an ODE model that uses the law of mass action to describe the chemical interactions mentioned above. An exponential decay of Mg is presented in the model; and after simulating the model for various

parameter values, an expected relationship between Mg and its corrosion products was perceived.

A PDE model for the corrosion of a Mg block was developed in Chapter 3, where the corrosion products, $Mg(OH)_2$ and $MgCO_3$, are envisioned to develop as porous layers around a Mg block. The advection and diffusion of water and carbon dioxide through porous media in the crystal structures was considered in the model. A closed system, in 1-D, was derived using mass conservation for Cartesian, cylindrical and spherical geometries. In terms of metal corrosion modelling, the consideration of a porous media flow in the crystal structures is a novel quality. In principle, the modelling approach is generic and can be used or adapted to model the corrosive process of any metals or alloys.

The model was derived for two cases on the reaction with Mg and water, an infinitely fast and a finitely fast reaction, where the hydroxide layer is absent at a small time phase. To solve the model numerically, small time asymptotic solutions were required. Two key timescales for the Mg corrosion process were examined, namely that of complete corrosion of the Mg block (T_α) and $Mg(OH)_2$ (T_β). There were parameters in the model for which data was undetermined; the rate of reaction between Mg and water, k, and the solid fractions of the hydroxide and carbonate layers, ε_1 and ε_2, respectively. Values for these parameters and the initial radius of an implant, S_0, were tuned into the numerical code to yield various results, where it was seen that a decrease in k and $(1 - \varepsilon_1)$ increased the longevity of an implant. In practice, k would be determined by the corrosive strength of an Mg or Mg based alloy. Furthermore, we compared the advective assumption in the current model to scenarios when there is no advective transport and when the advective transport is equal to the solid phase velocity. Hence, the results indicated that the current model gives a slightly faster Mg degradation time than the other advective transports.

Chapter 4 investigated the corrosion of Mg inside a single pore within a typical porous structure of Mg to account for the attribute that implant porosity allows better integration into the bone [6]. For this case, the PDE model was adapted to consider layers of corrosion products, $Mg(OH)_2$ and $MgCO_3$, inside the void. The model was developed for cylindrical geometry and was solved numerically in a similar way to that in Chapter 3. The factors of interest in the model were the timescale for pore closure (T_S), and the representation of corroded Mg at pore closure (α_∞). The simulations suggested that a decrease in k and $(1 - \varepsilon_1)$ increased the longevity of the pore, and a smaller k was found to yield less Mg corrosion at pore closure. Also, the initial radius of the pore, P_0, was changed in the model, which evidently showed that an increase in P_0 returned an increase in T_S and α_∞.

It can be concluded that a lower reaction rate, k, delays the degradation of a Mg implant and the closure time of the pores in the structure. The analysis shows that pores close within a few hours in Chapter 4, which is very rapid in comparison to the life time of an implant in Chapter 3 found to be within $O(10^2)$ days; this suggests that a porous structure of Mg will quickly evolve to a heterogeneous structure of Mg, $Mg(OH)_2$ and $MgCO_3$ with potentially some trapped air or hydrogen pockets. Though the PDE model in this work is formulated for a general 1-D geometry, it provides a good framework for Mg corrosion. There is plenty of scope for improvement, which is discussed in the next section of this chapter. Nevertheless, the modelling approach is unique for metal corrosion models and provides an advanced, novel model within Mg corrosion.

In contrast to the previous models, Chapter 5 presents a physiologically based pharmacokinetic (PBPK) model to observe the effect of a degrading Mg implant on the blood. An excess of Mg ions in the blood is known as a condition called hyper-magnesemia, which can cause serious implications to the human body particularly for

patients with renal disease. The model derived reflects the exchangeable contents of Mg ions to and from the blood, bone, tissue, and implant. Numerical results from the model portray the serum concentrations of Mg for different implant release rates. Due to the chosen timescale, the blood, bone and tissue appeared to equilibrate rapidly, and the tissue was acting as a reservoir for Mg. The urine excretion rate was assumed constant for the model derivation; we tuned in various values for this and the implant release rate to note the effects on serum Mg ion concentration. As expected a low urine excretion rate reflected higher levels of Mg, particularly with a high implant release rate, from which the patient would not survive. The model reflects the importance of monitoring the effects of Mg implantation in the blood, especially for patients with renal disease. Though the modelling can be improved on, it is capable in detecting plasma Mg to keep the effects of hypermagnesemia, after implantation, at bay, and is the first of its kind in approaching Mg implant fates within well-defined physiological systems.

6.1   Future Work

The PDE model is assumed to use radically symmetric geometries, and therefore would not be applicable for studies involving a typical Mg implant design. Extending the current modelling approach to consider 2-D or 3-D, non-simple geometries, poses non-trivial modelling challenges. The increase in the number of variables will require constitutive assumptions on the mechanical properties of the $Mg(OH)_2$ and $MgCO_3$ layers to close the system.

The current PDE model describes the corrosion of a smooth Mg surface in an aqueous media. The constituents of the media that an orthopaedic implant will be exposed to is more complex and may have significant affects on the corrosion behaviour. For example, a lower pH corrodes the protective layer of $Mg(OH)_2$ and

$MgCO_3$, so that the pure Mg is more exposed to the environment and thereby accelerating its corrosion [30, 34]. Furthermore, the tougher outer layer of $MgCO_3$ will itself be corroded and the resulting magnesium ions will eventually disperse and be excreted by the host. Modelling this corrosion process for future work leads to a modified boundary condition on $r = S$. This can be pursued further when appropriate information on the resorption and removal of $MgCO_3$ is available.

The reaction between $Mg(OH)_2$ and bicarbonate ions was considered in this work, but other ions in plasma also react with $Mg(OH)_2$. For example, chloride ions react with $Mg(OH)_2$ to form $MgCl_2$ [16]; here, the model can be extended to consider two reactive species for $Mg(OH)_2$, and assume, for simplicity, the outer layer consists of an isotropic mixture of $MgCO_3$ and $MgCl_2$. However, this will depend on the make-up of the Mg implant, and the context of the fluid environment surrounding the implant.

Furthermore, there is scope for the parameters, k, ε_1 and ε_2, to be estimated based on appropriate *in vitro* data. For example, data from time-course measurements of the proportion of constituents of small, spherical magnesium or magnesium alloy beads, immersed in appropriate media. The use of small beads should ensure the experiment to be completed in a practicable and cheap time frame, whilst them being spherical enables direct application of the model to calibrate the parameters with the data. The interpretation of k can be extended to the corrosion rate of different qualities of magnesium metal and its alloy. The presence of impurity, the grain size of micro-structures, depending on the preparation methods used, and the environmental factors can have dramatic effects on the corrosion rate thereby changing k [100, 101]. A further experiment involves the use of computed tomography (CT) images, which enables spatial details of the macroscale crystal structure that can be used to obtain direct measurements of ε_1 and ε_2. The model, with these tuned or determined parameters, provides a starting point to predict the corrosion properties

of much larger magnesium pellets in any 2-D or 3-D extension outlined above.

The work in Chapter 4 can be extended to investigate pore connectivity and the corrosion of several pores within a porous structure to determine the size of magnesium corrosion around all the pores of the implant. Further to this, the pores will have an affect on the degradation time of magnesium, and hence the work can be merged with that in Chapter 3 to give a more accurate timing of the complete degradation.

For the PBPK model, it was assumed that the urine excretion rate was a constant parameter γ. However, the kidneys serve the potential to excrete more or less magnesium to help preserve healthy levels in the blood [5]. To take this into account in the model for future work, there can be an equation for γ, which would be dependent on serum concentrations of Mg, but it must be acknowledged that there is an upper and lower bound for γ. Also, the exchange rate parameters in the model, taken from [94], were reference values, because compound or element specific values appeared to be missing from the literature. However, there is scope to determine these values experimentally, where the model can be used to tune in various values for the parameters to fit the data.

To end this thesis, we can declare that the work provides a good framework for magnesium corrosion. With the consideration of future work, the models in Chapter 3 and 4 have the potential to enhance magnesium corrosion for orthopaedic implants, where they can be used to predict timescales in a spatial manner, while the model in a Chapter 5 provides an additional tool to measure the patient's safety during implantation.

Appendix A

Appendix

A.1 Derivation of Interface Conditions

The chemical reactions occur only at the interfaces, α, β and S, and we describe this by using a reaction rate multiplied by a Dirac delta function centred at these interfaces. The Dirac delta function is infinite at the origin, say x_0, and zero everywhere else on the real line x and states that

$$\int_{-\infty}^{\infty} f(x)\delta(x - x_0) \quad dx \quad = \quad f(x_0),$$

which is used for the following derivation of interfaces. The total mass of water in the whole Mg corrosion system is represented by

$$\int_0^S (1 - \varepsilon)W r^d dr$$

where ε and W are the solid fraction and water concentration in the whole structure, and $d = 0, 1, 2$ for Cartesian, cylindrical and spherical geometry, respectively. The

rate of change of this mass is

$$\frac{\partial}{\partial t} \int_0^S (1-\varepsilon)Wr^d dr = (1-\varepsilon_2)\frac{\partial}{\partial t} \int_\beta^S W_2 r^d dr + (1-\varepsilon_1)\frac{\partial}{\partial t} \int_\alpha^\beta W_1 r^d dr; \qquad \text{(A.1)}$$

and by mass balance at the interfaces, LHS of (A.1) also gives

$$= \int_0^S (1-\varepsilon_2)R_S\delta(r-S)r^d dr + \int_0^S (1-\varepsilon_2)R_\beta\delta(r-\beta)r^d dr + \int_0^S (1-\varepsilon_1)R_\alpha\delta(r-\alpha)r^d dr$$

$$= \left[(1-\varepsilon_2)R_S S^d + (1-\varepsilon_2)R_\beta\beta^d + (1-\varepsilon_1)R_\alpha\alpha^d\right], \qquad \text{(A.2)}$$

where R_α, R_β and R_S are the rates of the reactions at the corresponding boundaries. Differentiating the RHS of equation (A.1), under the integral sign, yields

$$(1-\varepsilon_2)\left[\dot{S}S^2 W_2|_{r=S} - \dot{\beta}\beta^2 W_2|_{r=\beta} + \int_\beta^S r^d \frac{\partial W_2}{\partial t}dr\right] + (1-\varepsilon_1)\left[\dot{\beta}\beta^2 W_1|_{r=\beta} - \dot{\alpha}\alpha^2 W_1|_{r=\alpha}\right.$$

$$\left. + \int_\alpha^\beta r^d \frac{\partial W_1}{\partial t}dr\right], \qquad \text{(A.3)}$$

and using the flux terms defined in equation (3.7) gives

$$(1-\varepsilon_2)\left[\dot{S}S^d W_0^* - S^d J_{W_2}|_{r=S} - \dot{\beta}\beta^d W_2|_{r=\beta} + \beta^d J_{W_2}|_{r=\beta}\right] + (1-\varepsilon_1)\left[\dot{\beta}\beta^d W_1|_{r=\beta} - \right.$$

$$\left. \beta^d J_{W_1}|_{r=\beta} - \dot{\alpha}\alpha^d W_1|_{r=\alpha} + \alpha^d J_{W_1}|_{r=\alpha}\right], \qquad \text{(A.4)}$$

where $W_2|_{r=S} = W_0^*$. Matching equation (A.4) to (A.2) gives

$$R_\alpha = -\dot{\alpha}W_1|_{r=\alpha} + J_{W_1}|_{r=\alpha},$$

$$(1-\varepsilon_2)R_\beta = -\dot{\beta}\Big((1-\varepsilon_2)W_2|_{r=\beta} - (1-\varepsilon_1)W_1|_{r=\beta}\Big) + (1-\varepsilon_2)J_{W_2}|_{r=\beta}$$

$$- (1-\varepsilon_1)J_{W_1}|_{r=\beta};$$

formally, R_S cannot be prescribed as its values are set due to the water concentration being equal to that on the outer boundary.

The total mass of CO_2 in the whole structure is

$$\int_\beta^S (1 - \varepsilon_2) C_2 r^d dr.$$

As with water, the rate of change of this mass is

$$\frac{\partial}{\partial t} \int_\beta^S (1 - \varepsilon_2) C_2 r^d dr = (1 - \varepsilon_2) \left[\overline{R}_S S^d + \overline{R}_\beta \beta^d \right] \tag{A.5}$$

where $\overline{R}_S$ and $\overline{R}_\beta$ are the reaction rates at the corresponding boundary. The LHS of equation (A.5) is differentiated under the integral sign to give

$$(1 - \varepsilon_2) \left[\dot{S} S^2 C_2|_{r=S} - \dot{\beta} \beta^2 C_2|_{r=\beta} + \int_\beta^S r^d \frac{\partial C_2}{\partial t} dr \right], \tag{A.6}$$

and then the flux in equation (3.7) is applied yielding

$$(1 - \varepsilon_2) \left[\dot{S} S^d C_0^* - S^d J_{C_2}|_{r=S} - \dot{\beta} \beta^d C_2|_{r=\beta} + \beta^d J_{C_2}|_{r=\beta} \right], \tag{A.7}$$

where $C_2|_{r=S} = C_0^*$. Matching this to the RHS of (A.5) gives

$$\overline{R}_\beta = \dot{\beta} C_2|_{r=\beta} + J_{C_2}|_{r=\beta};$$

note, as before, $\overline{R}_S$ cannot be prescribed because its values are set by the CO_2 concentration being equal to that on the outer boundary.

A.2 Numerical Scheme of PDE Model

The PDE system of section 3.3.1 is solved in MATLAB using the Method of Lines (MoL), where the spatial derivatives are discretized and the time derivative remains as it is, thus an ODE solver can be applied to solve the new system. The numerical scheme is presented here. Let n_i be the number of space points for Zone 1 and Zone 2 with $i = 1, 2$. A uniform grid is used so that the interval size is

$$\Delta\rho_i = \frac{1}{n_i - 1}.$$

Variables $W_1(\rho, \tau), W_2(\rho, \tau), C_2(\rho, \tau), \alpha(\tau), \beta(\tau)$ and $S(\tau)$ are set up as

$$\boldsymbol{u} = \begin{pmatrix} \boldsymbol{W_1} \\ \boldsymbol{W_2} \\ \boldsymbol{C_2} \\ \alpha \\ \beta \\ S \end{pmatrix},$$

and are coded as

$$W_1(\rho, \tau) : u(1, ..., n_1), \quad W_2(\rho, \tau) : u(n_1 + 1, ..., n_1 + n_2),$$

$$C_2(\rho, \tau) : u(n_1 + n_2 + 1, ..., n_1 + 2n_2),$$

$$\alpha(\tau) : u(n_1 + 2n_2 + 1), \quad \beta(\tau) : u(n_1 + 2n_2 + 2), \quad S(\tau) : u(n_1 + 2n_2 + 3).$$

The initial conditions in the problem reflect the assumption that the two chemical reactions occur instantaneously; solutions in small time were analysed in Section 3.3.2 using perturbation theory. Once the initial conditions are set up in the code,

the mathematical model is configured using finite difference approximations for the spatial derivatives. Equations (3.36)-(3.38) are discretized using a central difference approximation for the second order derivatives whilst for the first order derivative term in space either central differences or an upwind method was used (the latter working best in most cases). The upwind method states that for

$$\frac{du}{dt} + a\frac{du}{dx},$$

then if $a > 0$ the spatial derivative is represented by the backward Euler formula and if $a < 0$ the spatial derivative is represented by the forward Euler. In the upwind case, this gives the following ODEs

$$\frac{dW_1}{d\tau} = \quad -\frac{1}{(\beta - \alpha)}\left[G_1(\rho_1, \tau) + v_{f_1} - \frac{D_W}{(\beta - \alpha)}d_\alpha(\rho_1, \tau)\right]\frac{W_1^{n+j} - W_1^{n+j-1}}{\Delta\rho_1}$$
$$+ \frac{D_W}{(\beta - \alpha)^2}\frac{W_1^{n+1} - 2W_1^n + W_1^{n-1}}{\Delta\rho_1^2}, \tag{A.8}$$

$$\frac{dW_2}{d\tau} = \quad -\frac{1}{(S - \beta)}\left[G_2(\rho_2, \tau) + v_{f_2} - \frac{D_W}{(S - \beta)}d_\beta(\rho_2, \tau)\right]\frac{W_2^{n+j} - W_2^{n+j-1}}{\Delta\rho_2}$$
$$+ \frac{D_W}{(S - \beta)^2}\frac{W_2^{n+1} - 2W_2^n + W_2^{n-1}}{\Delta\rho_2^2}, \tag{A.9}$$

$$\frac{dC_2}{d\tau} = \quad -\frac{1}{(S - \beta)}\left[G_2(\rho_2, \tau) + v_{f_2} - \frac{1}{(S - \beta)}d_\beta(\rho_2, \tau)\right]\frac{C_2^{n+j} - C_2^{n+j-1}}{\Delta\rho_2}$$
$$+ \frac{1}{(S - \beta)^2}\frac{C_2^{n+1} - 2C_2^n + C_2^{n-1}}{\Delta\rho_2^2}, \tag{A.10}$$

where $G_1, G_2, v_{f_i}, d_\alpha, d_\beta$ are defined in Section 3.3.1, d is the geometry, and j is 1 or 0 depending on the upwind scheme.

On the interfaces and boundaries, equations (A.8) and (A.9) consist of two fictitious values, $W_1^{n_1+1}$ and $W_2^{n_1-1}$. These are also called ghost points and need to be approximated and replaced so that they can be used in the numerical scheme. To do this, the flux boundary condition, which is the second equation in (3.43), (3.44) or

(3.45) depending on the phase, is used along with the condition that $W_1^{n_1} = W_2^{n_1}$ at β from which $\dfrac{\partial W_1^{n_1}}{\partial \tau} = \dfrac{\partial W_2^{n_1}}{\partial \tau}$ at β can be applied. For instance, for Phase 1.1, after discretizing the spatial derivatives we obtain

$$D_W \left[\frac{1-\varepsilon_1}{\beta - \alpha} \frac{W_1^{n_1+1} - W_1^{n_1-1}}{2\Delta\rho_1} - \frac{1-\varepsilon_2}{S-\beta} \frac{W_2^{n_1+1} - W_2^{n_1-1}}{2\Delta\rho_2} \right] = -\gamma_1 \left[\dot{\beta} + \frac{(w_\alpha - 1)\alpha^2 \dot{\alpha}}{\beta^2} \right]$$

$$(A.11)$$

and

$$-\frac{1}{(\beta - \alpha)} \left[G_1(\rho_1, \tau) + v_{f_1} - \frac{D_W}{(\beta - \alpha)} d_\alpha(\rho_1, \tau) \right] \frac{W_1^{n_1+j} - W_1^{n_1+j-1}}{\Delta\rho_1}$$
$$+ \frac{D_W}{(\beta - \alpha)^2} \frac{W_1^{n_1+1} - 2W_1^{n_1} + W_1^{n_1-1}}{\Delta\rho_1^2} = -\frac{1}{(S-\beta)} \left[G_2(\rho_2, \tau) + v_{f_2} - \right.$$
$$\left. \frac{D_W}{(S-\beta)} d_\beta(\rho_2, \tau) \right] \frac{W_2^{n_1+j} - W_2^{n_1+j-1}}{\Delta\rho_2} + \frac{D_W}{(S-\beta)^2} \frac{W_2^{n_1+1} - 2W_2^{n_1} + W_2^{n_1-1}}{\Delta\rho_2^2} \quad (A.12)$$

Now (A.11) and (A.12) can be rewritten as a pair of linear equations with two unknowns, $W_1^{n_1+1}$ and $W_2^{n_1-1}$, like

$$A_1 W_1^{n+1} + B_1 W_2^{n-1} = C_1,$$

$$A_2 W_1^{n+1} + B_2 W_2^{n-1} = C_2,$$

and these are solved in MATLAB to give approximations for the fictitious values which are then used in the numerical code. The same procedure is applied for each phase using the corresponding flux boundary condition.

The moving boundaries for each phase are discretized. The spatial derivatives for $\dot{\alpha}$ and $\dot{\beta}$ are descretized using a 3-point finite difference scheme to give

$$\dot{\alpha} = -(1-\varepsilon_1) \frac{D_W}{2\gamma_0(\beta - \alpha)} \frac{-3W_1^1 + 4W_1^2 - W_1^3}{2\Delta\rho_1},$$

for Phase 1.1 and 1.2, and

$$\dot{\beta} = -\frac{(1-\epsilon_2)}{\gamma_2\,(S-\beta)}\,\frac{-3C_2^{n_1+n_2+1}+4C_2^{n_1+n_2+2}-C_2^{n_1+n_2+3}}{2\Delta\rho_2} - \frac{(w_\alpha-1)\,\alpha^2\dot{\alpha}}{\beta^2}.$$

Recall that a spatial derivative is not used for $\dot{\alpha}$ in *Case 2*, (Phase 2.1, 2.2 and 2.3).

For *Case 2*, it is assumed that $W_1(1,\tau) \neq 0$, and as a result, equation (A.8) produces a fictitious value W_1^0. The ghost point is approximated using the boundary condition

$$-\,(1-\varepsilon_1)\frac{D_W}{\beta-\alpha}\frac{\partial W_1(1,\tau)}{\partial\rho} = -2\kappa\,[W_1^1(1,\tau)]^2,$$

where the spatial derivative is discretized using a backward difference formula. Hence

$$-\,(1-\varepsilon_1)\frac{D_W}{\beta-\alpha}\frac{W_1^1-W_1^0}{\Delta\rho} = -2\kappa\,[W_1^1(1,\tau)]^2,$$

$$\Rightarrow W_1^0 = W_1^1 - 2\,\Delta\rho\frac{\kappa\,[W_1^1]^2\,(\beta-\alpha)}{D_W\,(1-\varepsilon_1)},$$

and this is substituted into the code.

For Phase 2.1, when $C_2(1,\tau) \neq 0$ and $\alpha = \beta$, thus introducing a ghost point in equation (A.10), $C_2^{n_1+n_2}$. This is estimated using the third equation in (3.45), where the spatial derivative is replaced with a backward difference approximation. Hence

$$-\frac{(1-\varepsilon_2)}{S-\beta}\frac{C_2^{n_1+n_2+1}-C_2^{n_1+n_2}}{\Delta\rho} = \gamma_2 w_\alpha\,\dot{\beta}$$

$$\Rightarrow C_2^{n_1+n_2} = C_2^{n_1+n_2+1} + \Delta\rho\frac{\gamma_2\,w_\alpha\,\dot{\beta}\,(S-\beta)}{(1-\varepsilon_2)} \qquad (A.13)$$

and this is the approximation for the fictitious value $C_2^{n_1+n_2}$.

The system was then solved using *ode15s*.

A.3   Power Law Relation

A power law relationship is observed in Figure 3.9 in Section 3.4.3 where T_β was found to satisfy $T_\beta \propto S_0^2$. This was noted because the concentration of CO_2 is relatively small to that of water, so that $1 \ll \gamma_2$, and therefore the decay of the hydroxide is slow in comparison to that of pure Mg; so $\dot\beta \ll 1$ and hence $v_{f_2} \ll 1$. For $\beta = O(1)$ we expect $\partial_r C_2 = O(1)$ (as C_2 changes from 0 to 1 over an $O(1)$ distance), and as $1 \ll \gamma_2$ in Table 3.4 then for equation (3.25) to balance we need $\dot\beta = O(1/\gamma_2)$; so changes in β occur on an $O(\gamma_2)$ timescale. Writing $t = \gamma_2 \bar t$ and $v_{f_2} = \dfrac{\overline{v}_{f_2}}{\gamma_2}$, then as $\gamma_2 \to \infty$ in equation (3.25) we get for $r \in (\beta, S)$

$$\frac{1}{\gamma_2}\partial_{\bar t} C_2 + \frac{\overline{v}_{f_2}}{\gamma_2}\partial_r C_2 - \frac{1}{r^d}\partial_r(r^d \partial_r C_2) \sim 0, \tag{A.14}$$

subject to $C_2(\beta, \bar t) = 0$, $C_2(S, \bar t) = 1$ and $-(1 - \varepsilon_2)\partial_r C_2 = \dfrac{d\beta}{d\bar t}$ from (3.30), and we recall from (3.31) that, for $t > T_\alpha$,

$$S = S_0(\omega_\alpha \omega_\beta - (\omega_\beta - 1)(\beta/S_0)^{d+1})^{1/(d+1)}. \tag{A.15}$$

It is convenient to write

$$r = S_0 \bar r, \qquad \beta = S_0 \overline{\beta}, \qquad S = S_0 \overline{S}, \tag{A.16}$$

whereby integration of (A.14), as $\gamma_2 \to \infty$, yields

$$C_2 = \begin{cases} \dfrac{\overline r - \overline\beta}{\overline S - \overline\beta} & d = 0, \\[2mm] \ln\left(\overline r/\overline\beta\right)/\ln\left(\overline S/\overline\beta\right) & d = 1, \\[2mm] \dfrac{\overline S(\overline r - \overline\beta)}{(\overline S - \overline\beta)\overline r} & d = 2, \end{cases} \tag{A.17}$$

and, for each geometry, (A.15) implies

$$\frac{d\overline{\beta}}{d\overline{t}} = \begin{cases} -\dfrac{(1-\varepsilon_2)}{S_0^2\omega_\beta(\omega_\alpha - \overline{\beta})} & d = 0, \\[3ex] -\dfrac{2(1-\varepsilon_2)}{S_0^2\overline{\beta}[\ln((-\omega_\beta+1)\overline{\beta}^2 + \omega_\alpha\omega_\beta) - \ln(\overline{\beta}^2)]} & d = 1, \\[3ex] -\dfrac{(1-\varepsilon_2)((-\omega_\beta+1)\overline{\beta}^3 + \omega_\alpha\omega_\beta)^{1/3}}{S_0^2\overline{\beta}[((-\omega_\beta+1)\overline{\beta}^3 + \omega_\alpha\omega_\beta)^{1/3} - \overline{\beta}]} & d = 2. \end{cases} \qquad \text{(A.18)}$$

The equations in (A.18) are integrated w.r.t. $\overline{t}$ to give

$$\overline{t} - \frac{\omega_\beta S_0^2(2\omega_\alpha\overline{\beta} - \overline{\beta}^2 - \overline{\beta}_0(-2\omega_\alpha + \overline{\beta}_0))}{2(\varepsilon_2 - 1)} = 0,$$

$$\overline{t} + \frac{K_1 S_0^2 \ln(K_1) - K_2 S_0^2 \ln(K_2) - 2(\omega_\beta - 1)[-\ln(\overline{\beta})^{\overline{\beta}^2 S_0^2} + \ln(\overline{\beta}_0)^{\overline{\beta}_0^2 S_0^2}]}{4(\varepsilon_2 - 1)(\omega_\beta - 1)} = 0,$$

$$\overline{t} - \frac{S_0^2(\overline{\beta}^2 - \overline{\beta}_0^2)(\omega_\beta - 1) + [\omega_\alpha\omega_\beta S_0^3 - S_0^3\overline{\beta}^3\omega_\beta + S_0^3\overline{\beta}^3]^{2/3}}{2(\varepsilon_2 - 1)(\omega_\beta - 1)} +$$

$$\frac{[\omega_\alpha\omega_\beta S_0^3 - S_0^3\overline{\beta}_0^3\omega_\beta + S_0^3\overline{\beta}_0^3]^{2/3}}{2(\varepsilon_2 - 1)(\omega_\beta - 1)} = 0,$$

$$\text{(A.19)}$$

for Cartesian, cylindrical and spherical geometry, respectively; where

$$K_1 = (-\omega_\beta + 1)\overline{\beta}^2 + \omega_\alpha\omega_\beta, \qquad K_2 = (-\omega_\beta + 1)\overline{\beta}_0^2 + \omega_\alpha\omega_\beta.$$

Imposing $\overline{\beta}(0) = \overline{\beta}_0$, the equations in (A.19) can be solved to give the implicit solution

$$\overline{t} \sim -\frac{\omega_\beta S_0^2\overline{\beta}_0(-2\omega_\alpha + \overline{\beta}_0)}{2(1 - \varepsilon_2)},$$

$$\overline{t} \sim \frac{S_0^2\left[((\overline{\beta}_0^2 - \omega_\alpha)\omega_\beta - \overline{\beta}_0^2)\ln((-\omega_\beta + 1)\overline{\beta}_0^2 + \omega_\alpha\omega_\beta) + \ln(\omega_\alpha\omega_\beta)^{\omega_\alpha\omega_\beta} - \ln(\overline{\beta}_0)^{2\overline{\beta}_0^2(\omega_\beta - 1)}\right]}{4(1 - \varepsilon_2)(\omega_\beta - 1)},$$

$$\overline{t} \sim \frac{S_0^2\left[((-\omega_\beta - 1)\overline{\beta}_0^3 + \omega_\alpha\omega_\beta)^{2/3} - (\omega_\alpha\omega_\beta)^{2/3} + (\omega_\beta - 1)\overline{\beta}_0^2\right]}{2(1 - \varepsilon_2)(\omega_\beta - 1)},$$

for Cartesian, cylindrical and spherical geometry, respectively. We note that the above

discussion represents an outer solution in time in the limit $\gamma_2 \to \infty$. The constant $\overline{\beta_0}$ can, in theory, be determined from the inner solution for the timescale $t = O(1)$ (or $\bar{t} = O(1/\gamma_2)$); but this analysis has not been undertaken.

Bibliography

[1] Safia K Ahmed, John P Ward, and Yang Liu. Numerical modelling of effects of biphasic layers of corrosion products to the degradation of magnesium metal in vitro. *Materials*, 11(1):1, 2017.

[2] University of Washington. Online musculoskeletal radiology book, https://rad.washington.edu/about-us/academic-sections/musculoskeletal-radiology/teaching-materials/online-musculoskeletal-radiology-book/orthopedic-hardware/, [Accessed 28 Nov. 2017].

[3] Dewei Zhao, Frank Witte, Faqiang Lu, Jiali Wang, Junlei Li, and Ling Qin. Current status on clinical applications of magnesium-based orthopaedic implants: A review from clinical translational perspective. *Biomaterials*, 112:287–302, 2017.

[4] Huaye Zhuang, Yong Han, and Ailing Feng. Preparation, mechanical properties and in vitro biodegradation of porous magnesium scaffolds. *Materials Science and Engineering: C*, 28(8):1462–1466, 2008.

[5] Wilhelm Jahnen-Dechent and Markus Ketteler. Magnesium basics. *Clinical kidney journal*, 5(Suppl_1):i3–i14, 2012.

[6] Mark P Staiger, Alexis M Pietak, Jerawala Huadmai, and George Dias. Mag-

nesium and its alloys as orthopedic biomaterials: a review. *Biomaterials*, 27(9):1728–1734, 2006.

[7] Ronald J Elin. Magnesium metabolism in health and disease. *Disease-a-month*, 34(4):166–218, 1988.

[8] R Swaminathan. Magnesium metabolism and its disorders. *The Clinical Biochemist Reviews*, 24(2):47, 2003.

[9] Blake E Peterson, Aneel Jiwanlal, Gregory J Della Rocca, and Brett D Crist. Orthopedic trauma and aging: it isn't just about mortality. *Geriatric orthopaedic surgery & rehabilitation*, 6(1):33–36, 2015.

[10] Georg Reith, Vera Schmitz-Greven, Kai O Hensel, Marco M Schneider, Tibor Tinschmann, Bertil Bouillon, and Christian Probst. Metal implant removal: benefits and drawbacks–a patient survey. *BMC surgery*, 15(1):96, 2015.

[11] Nils-Erik L Saris, Eero Mervaala, Heikki Karppanen, Jahangir A Khawaja, and Andrzei Lewenstam. Magnesium: an update on physiological, clinical and analytical aspects. *Clinica chimica acta*, 294(1):1–26, 2000.

[12] Rongchang Zeng, Wolfgang Dietzel, Frank Witte, Norbert Hort, and Carsten Blawert. Progress and challenge for magnesium alloys as biomaterials. *Advanced Engineering Materials*, 10(8):B3–B14, 2008.

[13] AH Yusop, AA Bakir, NA Shaharom, MR Abdul Kadir, and H Hermawan. porous biodegradable metals for hard tissue scaffolds: a review. *International journal of biomaterials*, 2012.

[14] Yifeng Zhang, Jiankun Xu, Ye Chun Ruan, Mei Kuen Yu, Micheal O'Laughlin, Helen Wise, Di Chen, Li Tian, Dufang Shi, Jiali Wang, et al. Implant-derived

magnesium induces local neuronal production of cgrp to improve bone-fracture healing in rats. *Nature medicine*, 22(10):1160, 2016.

[15] LJ Liu and M Schlesinger. Corrosion of magnesium and its alloys. *Corrosion Science*, 51(8):1733–1737, 2009.

[16] Frank Witte, Norbert Hort, Carla Vogt, Smadar Cohen, Karl Ulrich Kainer, Regine Willumeit, and Frank Feyerabend. Degradable biomaterials based on magnesium corrosion. *Current opinion in solid state and materials science*, 12(5):63–72, 2008.

[17] Nan Zhao and Donghui Zhu. Collagen self-assembly on orthopedic magnesium biomaterials surface and subsequent bone cell attachment. *PloS one*, 9(10):e110420, 2014.

[18] Richard Harrison, Diana Maradze, Simon Lyons, Yufeng Zheng, and Yang Liu. Corrosion of magnesium and magnesium–calcium alloy in biologically-simulated environment. *Progress in Natural Science: Materials International*, 24(5):539–546, 2014.

[19] F. Clarelli, B. De Filippo, and R. Natalini. Mathematical model of copper corrosion. *Applied Mathematical Modelling*, 38(19-20):4804–4816, 2014.

[20] Jemimah Walker, Shaylin Shadanbaz, Timothy BF Woodfield, Mark P Staiger, and George J Dias. Magnesium biomaterials for orthopedic application: a review from a biological perspective. *Journal of Biomedical Materials Research Part B: Applied Biomaterials*, 102(6):1316–1331, 2014.

[21] Frank Witte. The history of biodegradable magnesium implants: a review. *Acta Biomaterialia*, 6(5):1680–1692, 2010.

[22] Sankalp Agarwal, James Curtin, Brendan Duffy, and Swarna Jaiswal. Biodegradable magnesium alloys for orthopaedic applications: a review on corrosion, biocompatibility and surface modifications. *Materials Science and Engineering: C*, 68:948–963, 2016.

[23] Nicholas Travis Kirkland. Magnesium biomaterials: past, present and future. *Corrosion Engineering, Science and Technology*, 47(5):322–328, 2012.

[24] YF Zheng, XN Gu, and F Witte. Biodegradable metals. *Materials Science and Engineering: R: Reports*, 77:1–34, 2014.

[25] Guang-Ling Song. *Corrosion prevention of magnesium alloys*. Elsevier, 2013.

[26] Douglas C Hansen. Metal corrosion in the human body: the ultimate biocorrosion scenario. *The Electrochemical Society Interface*, 17(2):31, 2008.

[27] Jingxin Yang, Gerry L Koons, Guang Cheng, Linhui Zhao, Antonios G Mikos, and Fuzhai Cui. A review on the exploitation of biodegradable magnesium-based composites for medical applications. *Biomedical Materials*, 13(2):022001, 2018.

[28] Guangling Song. Control of biodegradation of biocompatable magnesium alloys. *Corrosion Science*, 49(4):1696–1701, 2007.

[29] Hazibullah Waizy, Jan-Marten Seitz, Janin Reifenrath, Andreas Weizbauer, Friedrich-Wilhelm Bach, Andrea Meyer-Lindenberg, Berend Denkena, and Henning Windhagen. Biodegradable magnesium implants for orthopedic applications. *Journal of Materials Science*, 48(1):39–50, 2013.

[30] Emily K Brooks, Stephanie Der, and Mark T Ehrensberger. Corrosion and mechanical performance of az91 exposed to simulated inflammatory conditions. *Materials Science and Engineering: C*, 60:427–436, 2016.

[31] Francesca Cecchinato, Nezha Ahmad Agha, Adela Helvia Martinez-Sanchez, Berengere Julie Christine Luthringer, Frank Feyerabend, Ryo Jimbo, Regine Willumeit-Römer, and Ann Wennerberg. Influence of magnesium alloy degradation on undifferentiated human cells. *PloS one*, 10(11):e0142117, 2015.

[32] Ian Johnson and Huinan Liu. A study on factors affecting the degradation of magnesium and a magnesium-yttrium alloy for biomedical applications. *PLoS One*, 8(6):e65603, 2013.

[33] NT Kirkland, Nick Birbilis, and MP Staiger. Assessing the corrosion of biodegradable magnesium implants: a critical review of current methodologies and their limitations. *Acta biomaterialia*, 8(3):925–936, 2012.

[34] Guangling Song and Andrej Atrens. Understanding magnesium corrosion—a framework for improved alloy performance. *Advanced engineering materials*, 5(12):837–858, 2003.

[35] Regine Willumeit, Janine Fischer, Frank Feyerabend, Norbert Hort, Ulrich Bismayer, Stefanie Heidrich, and Boriana Mihailova. Chemical surface alteration of biodegradable magnesium exposed to corrosion media. *Acta biomaterialia*, 7(6):2704–2715, 2011.

[36] Erlin Zhang, Liping Xu, Guoning Yu, Feng Pan, and Ke Yang. In vivo evaluation of biodegradable magnesium alloy bone implant in the first 6 months implantation. *Journal of biomedical materials research Part A*, 90(3):882–893, 2009.

[37] Shashi S Pathak, Sharathkumar K Mendon, Michael D Blanton, and James W Rawlins. Magnesium-based sacrificial anode cathodic protection coatings (mg-rich primers) for aluminum alloys. *Metals*, 2(3):353–376, 2012.

[38] Akiko Yamamoto and Sachiko Hiromoto. Effect of inorganic salts, amino acids and proteins on the degradation of pure magnesium in vitro. *Materials Science and Engineering: C*, 29(5):1559–1568, 2009.

[39] Elmar Willbold, Andreas Weizbauer, Anneke Loos, Jan-Marten Seitz, Nina Angrisani, Henning Windhagen, and Janin Reifenrath. Magnesium alloys: A stony pathway from intensive research to clinical reality. different test methods and approval-related considerations. *Journal of Biomedical Materials Research Part A*, 105(1):329–347, 2017.

[40] Martin Jönsson, Dan Persson, and Dominique Thierry. Corrosion product formation during nacl induced atmospheric corrosion of magnesium alloy az91d. *Corrosion Science*, 49(3):1540–1558, 2007.

[41] Anastasia Rakow, Janosch Schoon, Anke Dienelt, Thilo John, Martin Textor, Georg Duda, Carsten Perka, Frank Schulze, and Andrea Ode. Influence of particulate and dissociated metal-on-metal hip endoprosthesis wear on mesenchymal stromal cells in vivo and in vitro. *Biomaterials*, 98:31–40, 2016.

[42] Sara Castiglioni, Alessandra Cazzaniga, Walter Albisetti, and Jeanette AM Maier. Magnesium and osteoporosis: current state of knowledge and future research directions. *Nutrients*, 5(8):3022–3033, 2013.

[43] Zeeshan Sheikh, Shariq Najeeb, Zohaib Khurshid, Vivek Verma, Haroon Rashid, and Michael Glogauer. Biodegradable materials for bone repair and tissue engineering applications. *Materials*, 8(9):5744–5794, 2015.

[44] Lili Tan, Xiaoming Yu, Peng Wan, and Ke Yang. Biodegradable materials for bone repairs: a review. *Journal of Materials Science & Technology*, 29(6):503–513, 2013.

[45] Javier Trinidad, Iñigo Marco, Gurutze Arruebarrena, Joachim Wendt, Dietmar Letzig, Eneko Sáenz de Argandoña, and Russell Goodall. Processing of magnesium porous structures by infiltration casting for biomedical applications. *Advanced Engineering Materials*, 16(2):241–247, 2014.

[46] Frank Witte, V Kaese, H Haferkamp, E Switzer, A Meyer-Lindenberg, CJ Wirth, and H Windhagen. In vivo corrosion of four magnesium alloys and the associated bone response. *Biomaterials*, 26(17):3557–3563, 2005.

[47] Amy Chaya, Sayuri Yoshizawa, Kostas Verdelis, Nicole Myers, Bernard J Costello, Da-Tren Chou, Siladitya Pal, Spandan Maiti, Prashant N Kumta, and Charles Sfeir. In vivo study of magnesium plate and screw degradation and bone fracture healing. *Acta biomaterialia*, 18:262–269, 2015.

[48] Chen Liu, Zheng Ren, Yongdong Xu, Song Pang, Xinbing Zhao, and Ying Zhao. Biodegradable magnesium alloys developed as bone repair materials: A review. *Scanning*, 2018, 2018.

[49] Nan Li and Yufeng Zheng. Novel magnesium alloys developed for biomedical application: a review. *Journal of Materials Science & Technology*, 29(6):489–502, 2013.

[50] Florencia Alvarez, Puerto RM Lozano, Blanca Pérez-Maceda, Claudia A Grillo, and Lorenzo de Mele M Fernández. Time-lapse evaluation of interactions between biodegradable mg particles and cells. *Microscopy and microanalysis: the official journal of Microscopy Society of America, Microbeam Analysis Society, Microscopical Society of Canada*, 22(1):1–12, 2016.

[51] Henning Windhagen, Kerstin Radtke, Andreas Weizbauer, Julia Diekmann, Yvonne Noll, Ulrike Kreimeyer, Robert Schavan, Christina Stukenborg-

Colsman, and Hazibullah Waizy. Biodegradable magnesium-based screw clinically equivalent to titanium screw in hallux valgus surgery: short term results of the first prospective, randomized, controlled clinical pilot study. *Biomedical engineering online*, 12(1):62, 2013.

[52] Roland Biber, Johannes Pauser, Matthias Brem, and Hermann Josef Bail. Bioabsorbable metal screws in traumatology: A promising innovation. *Trauma Case Reports*, 8:11–15, 2017.

[53] Dewei Zhao, Shibo Huang, Faqiang Lu, Benjie Wang, Lei Yang, Ling Qin, Ke Yang, Yangde Li, Weirong Li, Wei Wang, et al. Vascularized bone grafting fixed by biodegradable magnesium screw for treating osteonecrosis of the femoral head. *Biomaterials*, 81:84–92, 2016.

[54] Jee-Wook Lee, Hyung-Seop Han, Kyeong-Jin Han, Jimin Park, Hojeong Jeon, Myoung-Ryul Ok, Hyun-Kwang Seok, Jae-Pyoung Ahn, Kyung Eun Lee, Dong-Ho Lee, et al. Long-term clinical study and multiscale analysis of in vivo biodegradation mechanism of mg alloy. *Proceedings of the National Academy of Sciences*, 113(3):716–721, 2016.

[55] BJ Luthringer, Frank Feyerabend, and Regine Willumeit-Römer. Magnesium-based implants: a mini-review. *Magnes Res*, 27(4):142–54, 2014.

[56] Claire Chainais-Hillairet and Ingrid Lacroix-Violet. On the existence of solutions for a drift-diffusion system arising in corrosion modelling. *Discrete and Continuous Dynamical Systems-Series B*, 20(1):15–pages, 2015.

[57] Richard S Larson. A physical and mathematical model for the atmospheric sulfidation of copper by hydrogen sulfide. *Journal of the Electrochemical Society*, 149(2):B40–B46, 2002.

[58] Adrian Muntean and Michael Böhm. A moving-boundary problem for concrete carbonation: global existence and uniqueness of weak solutions. *Journal of mathematical analysis and applications*, 350(1):234–251, 2009.

[59] Raffaele Landolfo, Lucrezia Cascini, and Francesco Portioli. Modeling of metal structure corrosion damage: a state of the art report. *Sustainability*, 2(7):2163–2175, 2010.

[60] Wen Sun, Guichang Liu, Lida Wang, Tingting Wu, and Yang Liu. An arbitrary lagrangian–eulerian model for studying the influences of corrosion product deposition on bimetallic corrosion. *Journal of Solid State Electrochemistry*, 17(3):829–840, 2013.

[61] RE Melchers. Mathematical modelling of the diffusion controlled phase in marine immersion corrosion of mild steel. *CORROSION SCIENCE*, 45(5):923–940, MAY 2003.

[62] Yury V Zaika and Natalia I Rodchenkova. Modelling of zirconium alloy hydrogenation. *Journal of Physics: Conference Series*, 769(1):012028, 2016.

[63] Srdjan Nešić. Key issues related to modelling of internal corrosion of oil and gas pipelines–a review. *Corrosion science*, 49(12):4308–4338, 2007.

[64] Steven I Barry and James Caunce. Exact and numerical solutions to a stefan problem with two moving boundaries. *Applied Mathematical Modelling*, 32(1):83–98, 2008.

[65] Scott W McCue, Bisheng Wu, and James M Hill. Classical two-phase stefan problem for spheres. In *Proceedings of the Royal Society of London A: Mathematical, Physical and Engineering Sciences*, volume 464, pages 2055–2076. The Royal Society, 2008.

[66] Alan B.. Tayler. *Mathemmatical Models in Applied Mechanics*. Clarendon press, Oxford, 1986.

[67] F. Clarelli, A. Fasano, and R. Natalini. Mathematics and monument conservation: free boundary models of marble sulfation. *SIAM Journal on Applied Mathematics*, 69(1):149–168, 2008.

[68] M Dahms, D Höche, N Ahmad Agha, F Feyerabend, and R Willumeit-Römer. A simple model for long-time degradation of magnesium under physiological conditions. *Materials and Corrosion*, 2017.

[69] R Montoya, C Iglesias, ML Escudero, and MC García-Alonso. Modeling in vivo corrosion of az31 as temporary biodegradable implants. experimental validation in rats. *Materials Science and Engineering: C*, 41:127–133, 2014.

[70] P Bajger, JMA Ashbourn, Varun Manhas, Yann Guyot, Karel Lietaert, and Liesbet Geris. Mathematical modelling of the degradation behaviour of biodegradable metals. *Biomechanics and modeling in mechanobiology*, 16(1):227–238, 2017.

[71] Xiaomei Zhuang and Chuang Lu. Pbpk modeling and simulation in drug research and development. *Acta Pharmaceutica Sinica B*, 6(5):430–440, 2016.

[72] HM Jones and K Rowland-Yeo. Basic concepts in physiologically based pharmacokinetic modeling in drug discovery and development. *CPT: pharmacometrics & systems pharmacology*, 2(8):1–12, 2013.

[73] Thomas J Snowden, Piet H van der Graaf, and Marcus J Tindall. Model reduction in mathematical pharmacology. *Journal of pharmacokinetics and pharmacodynamics*, pages 1–19, 2018.

[74] A Dokoumetzidis and L Aarons. Proper lumping in systems biology models. *IET systems biology*, 3(1):40–51, 2009.

[75] Aristides Dokoumetzidis and Leon Aarons. A method for robust model order reduction in pharmacokinetics. *Journal of pharmacokinetics and pharmacodynamics*, 36(6):613, 2009.

[76] Thierry Wendling, Nikolaos Tsamandouras, Swati Dumitras, Etienne Pigeolet, Kayode Ogungbenro, and Leon Aarons. Reduction of a whole-body physiologically based pharmacokinetic model to stabilise the bayesian analysis of clinical data. *The AAPS journal*, 18(1):196–209, 2016.

[77] Dennis Reddyhoff, John Ward, Dominic Williams, Sophie Regan, and Steven Webb. Timescale analysis of a mathematical model of acetaminophen metabolism and toxicity. *Journal of theoretical biology*, 386:132–146, 2015.

[78] Richard N Upton and Guy L Ludbrook. Pharmacokinetic-pharmacodynamic modelling of the cardiovascular effects of drugs–method development and application to magnesium in sheep. *BMC pharmacology*, 5(1):5, 2005.

[79] Jianfeng Lu, Marc Pfister, Paolo Ferrari, Gang Chen, and Lewis Sheiner. Pharmacokinetic-pharmacodynamic modelling of magnesium plasma concentration and blood pressure in preeclamptic women. *Clinical pharmacokinetics*, 41(13):1105–1113, 2002.

[80] Nicholas F Britton. *Essential mathematical biology*. Springer Science & Business Media, 2012.

[81] Scott H Faro, Feroze B Mohamed, Meng Law, and John T Ulmer. *Functional neuroradiology: principles and clinical applications*. Springer Science & Business Media, 2011.

[82] E. L. Cussler. *Diffusion: Mass Transfer in Fluid Systems (2nd ed.)*. New York: Cambridge University Press, 1997.

[83] David R. Lide. *CRC Handbook of Chemistry and Physics, 84th Edition.* CRC Press. Boca Raton, Florida, 2003.

[84] Dicken Weatherby and Scott Ferguson. *Blood chemistry and CBC analysis*, volume 4. Weatherby & Associates, LLC, 2004.

[85] A. Campo and U. Lacoa. Adaptation of the method of lines (mol) to the matlab code for the analysis of the stefan problem. *WSEAS Transactions on Heat & Mass Transfer*, 9:19–26, 2014.

[86] Y Li, J Zhou, P Pavanram, MA Leeflang, LI Fockaert, B Pouran, N Tümer, K-U Schröder, JMC Mol, H Weinans, et al. Additively manufactured biodegradable porous magnesium. *Acta biomaterialia*, 2017.

[87] Ingrid Morgenthal, Olaf Andersen, Cris Kostmann, Günter Stephani, Thomas Studnitzky, Frank Witte, and Bernd Kieback. Highly porous magnesium alloy structures and their properties regarding degradable implant application. *Advanced Engineering Materials*, 16(3):309–318, 2014.

[88] CE Wen, Y Yamada, K Shimojima, Y Chino, H Hosokawa, and M Mabuchi. Compressibility of porous magnesium foam: dependency on porosity and pore size. *Materials Letters*, 58(3-4):357–360, 2004.

[89] Jeroen HF De Baaij, Joost GJ Hoenderop, and René JM Bindels. Regulation of magnesium balance: lessons learned from human genetic disease. *Clinical kidney journal*, 5(Suppl_1):i15–i24, 2012.

[90] Joel Michels Topf and Patrick T Murray. Hypomagnesemia and hypermagnesemia. *Reviews in endocrine & metabolic disorders*, 4(2):195–206, 2003.

[91] Syed Rizwan Bokhari, Ravi Siriki, Federico J Teran, and Vecihi Batuman. Fatal hypermagnesemia due to laxative use: Case report and review of the literature. *The American Journal of the Medical Sciences*, 2017.

[92] Raj K Gupta, Jeffrey L Benovic, and Zelda B Rose. The determination of the free magnesium level in the human red blood cell by 31p nmr. *Journal of Biological Chemistry*, 253(17):6172–6176, 1978.

[93] H Millart, V Durlach, and J Durlach. Red blood cell magnesium concentrations: analytical problems and significance. *Magnesium research*, 8(1):65–76, 1995.

[94] Ronald P Brown, Michael D Delp, Stan L Lindstedt, Lorenz R Rhomberg, and Robert P Beliles. Physiological parameter values for physiologically based pharmacokinetic models. *Toxicology and industrial health*, 13(4):407–484, 1997.

[95] Wei-Yu Chen, Yi-Hsien Cheng, Nan-Hung Hsieh, Bo-Chun Wu, Wei-Chun Chou, Chia-Chi Ho, Jen-Kun Chen, Chung-Min Liao, and Pinpin Lin. Physiologically based pharmacokinetic modeling of zinc oxide nanoparticles and zinc nitrate in mice. *International journal of nanomedicine*, 10:6277, 2015.

[96] Jeffry D Schroeter, Andy Nong, Miyoung Yoon, Michael D Taylor, David C Dorman, Melvin E Andersen, and Harvey J Clewell III. Analysis of manganese tracer kinetics and target tissue dosimetry in monkeys and humans with multi-route physiologically based pharmacokinetic models. *Toxicological sciences*, 120(2):481–498, 2010.

[97] Karolina Stasiak, Aleksandra Roślewska, Magdalena Stanek, Dorota Cygan-Szczegielniak, and Bogdan Janicki. The content of selected minerals determined in the liver, kidney and meat of pigs. *Journal of Elementology*, 22(4), 2017.

[98] MT Vilei, A Granato, C Ferraresso, D Neri, P Carraro, G Gerunda, and M Muraca. Comparison of pig, human and rat hepatocytes as a source of liver specific metabolic functions in culture systems-implications for use in bioartificial liver devices. *The International journal of artificial organs*, 24(6):392–396, 2001.

[99] Richard S. Varga. *Geršgorin and His Circles,*. Berlin: Springer-Verlag, 2004.

[100] Yichi Liu, Debao Liu, Chen You, and Minfang Chen. Effects of grain size on the corrosion resistance of pure magnesium by cooling rate-controlled solidification. *Frontiers of Materials Science*, 9(3):247–253, Sep 2015.

[101] Joëlle Hofstetter, Elisabeth Martinelli, Annelie M Weinberg, Minh Becker, Bernhard Mingler, Peter J Uggowitzer, and Jörg F Löffler. Assessing the degradation performance of ultrahigh-purity magnesium in vitro and in vivo. *Corrosion Science*, 91:29–36, 2015.

[102] James Albert Sethian. *Level set methods and fast marching methods: evolving interfaces in computational geometry, fluid mechanics, computer vision, and materials science*, volume 3. Cambridge university press, 1999.

[103] Scott W McCue, Mike Hsieh, Timothy J Moroney, and Mark I Nelson. Asymptotic and numerical results for a model of solvent-dependent drug diffusion through polymeric spheres. *SIAM Journal on Applied Mathematics*, 71(6):2287–2311, 2011.

[104] GD Byrne and S Thompson. Error control matters. *Departments of Applied*, 405, 2007.

[105] James D Murray. *Mathematical biology. II Spatial models and biomedical applications {Interdisciplinary Applied Mathematics V. 18}*. Springer-Verlag New York Incorporated New York, 2001.

[106] Mike Hsieh, Scott W McCue, Timothy J Moroney, and Mark I Nelson. Drug diffusion from polymeric delivery devices: a problem with two moving boundaries. *ANZIAM Journal*, 52:549–566, 2011.

[107] Meisam Salahshoor and Yuebin Guo. Biodegradable orthopedic magnesium-calcium (mgca) alloys, processing, and corrosion performance. *Materials*, 5(1):135–155, 2012.